THE EXPERIMENTAL AND THEORETICAL INVESTIGATION OF THE HYDROGEN SULFIDE SPLITTING CYCLE FOR HYDROGEN PRODUCTION

A Thesis Submitted to the College of

Graduate Studies and Research

In Partial Fulfilment of the Requirements

For the Degree of Doctor of Philosophy

In the Department of Chemical and Biological Engineering

University of Saskatchewan

Saskatoon

By

Armin Moniri

PERMISSION TO USE

In presenting this thesis in partial fulfilment of the requirements for a postgraduate degree from the University of Saskatchewan, I agree that the libraries of this University may make it freely available for inspection. I further agree that permission for copying of this thesis in any manner, in whole or in part, for scholarly purposes may be granted by the professor or professors who supervised my thesis work or, in their absence, by the Head of the Department or the Dean of the College in which my thesis work was done. It is understood that any copying or publication or use of this thesis or parts thereof for financial gain shall not be allowed without my written permission. It is also understood that due recognition shall be given to me and to the University of Saskatchewan in any scholarly use that may be made of any material in my thesis.

Requests for permission to copy or to make other use of material in this thesis in whole or part should be addressed to:

Head of the Department of Chemical and Biological Engineering

University of Saskatchewan

1C01 Engineering Building, 57 Campus Drive

Saskatoon, Saskatchewan, S7N 5A9

ABSTRACT

In Dr. Hui Wang's research group at the University of Saskatchewan, an H_2S splitting cycle was earlier developed as a novel method to convert H_2S, a significant waste product in the oil and gas industry, to hydrogen, which is desired in the same industry for hydrotreating processes. In this research, it was realized that hydrogen could also be produced from variety of sulfur-containing feedstock as long as it could be converted into SO_2 to feed the Bunsen reaction followed by hydroiodic acid decomposition to form hydrogen. Therefore, an exergy analysis was performed on various chemical reaction routes, or open-loop cycles, to make use of sulfur-containing compounds, which exist in different industry sectors as byproducts or waste products, for hydrogen production. The exergy analysis tells which route makes hydrogen production from sulfur-containing feedstock more energy-efficient.

This research experimentally focused on the Bunsen reaction, the centre reaction in H_2S splitting cycle, the open-loop cycles, as well as the sulfur-iodine (S-I) water-splitting cycle. An iodine-toluene solution was used to render the Bunsen reaction to occur at ambient temperature so as to avoid the side reactions and I_2 vapour deposition which usually occur at higher temperatures. For the multiphase reaction system when organic solution is used, however, the improvement of cross-phase mass transfer becomes crucial. Glass-made, Low Flow Corning® Advanced-Flow™ Reactor (LF-AFR) was chosen for this study due to its excellent resistance to acid-caused corrosion and capability to improve the mixing efficiency of multiphase fluids. With this reactor, the overall mass transfer coefficients were calculated for binary systems (SO_2-water and SO_2-toluene). The effects of operating conditions such as gas and liquid flow rates, the water to toluene ratio, and the temperature in the ambient range (22-70 ^oC) on the absorption rates of SO_2 and the I_2 reaction rate were studied at the University of Saskatchewan. It was understood that the mass transfer

coefficients are highly dependent on the gas and liquid flow rates in the LF-AFR. Gas phase composition also played a big role where the K_La values tended to be smaller for the systems with the highest gas phase resistance. The mass transfer study implied that the gas absorption in liquid was completed in the contacting fluidic module where the gas-liquid mixture was initially mixed. Later, all experiments at higher flow rates of fluids were conducted in the next commercially available size of Corning® Advanced-Flow™ Reactor products (G1-AFR) at the Corning Reactor Technology Center. The results revealed the seamless scaling-up capability of Corning reactors from the LF-AFR to the G1-AFR when the flow rates were increased twenty times.

Based on the experimental results for the Bunsen reaction in this thesis and the results for other sections studied earlier by this group, a hydrogen production plant with the H_2S splitting cycle technology was designed in a typical size of the hydrogen plant of a heavy oil upgrader followed by an economic analysis.

ACKNOWLEDGMENTS

First of all, I would like to thank my supervisor, Professor Hui Wang, for his support, knowledge, non-stop engagement and punctuality, which significantly improved my work. His professional attitude was a key factor in overcoming the predicaments encountered during the research. It would not be possible to finish this PhD thesis without his supervision from the beginning to the end of the project. I also appreciate his mentorship in providing the opportunity to grow my research skills by encouraging me to enroll in the MITACS international internship at the Corning Reactor Technology Center in China.

I would like to thank the members of my advisory committee, Dr. Ajay Dalai, Dr. Richard Evitts, Dr. Jafar Soltan and Dr. Stephan Foley for their valuable feedback on my progress during the last four years. Their comments and suggestions helped me to improve the quality of this thesis.

I am also grateful to the technical staff of the Chemical & Biological Engineering Departments at the University of Saskatchewan, especially RLee Prokopishyn, Richard Blondin, Dragan Cekic, and Heli Eunike for assistance with the purchasing of laboratory supplies and equipment, developing analytical methods and troubleshooting the instruments.

Many thanks to Corning China Regional Headquarters and Corning Reactor Technology Center (China) staff, especially Dr. Yi Jiang, Dr. Bing Ma and Dr. Eric Wu for their invaluable guidance and time spent helping me work with them, and also to Professor Yue Zhang and Professor Shenghu Yan and their supportive students from Changzhou University for allowing me to use their gas and liquid analyzers. Special thanks to Dr. Hong-Xiang Ou of Changzhou University and her lovely family for making great moments for me while I was in China.

The University of Saskatchewan, NSERC, and MITACS should also be acknowledged for providing funding for this research project.

I also would like to recognize the following CHE 422 students (H_2S Solutions group), Chris Morien, Brett Smith, Chris Clarkson and Jordan Lewis, for their great contributions in designing the hydrogen production plant.

Many thanks to Dr. Ibrahim Dincer, Professor of the Department of Automotive, Mechanical and Manufacturing Engineering at the University of Ontario Institute of Technology, for his beneficial guidance and information in exergy analysis.

Last but not least, I would like to express my gratitude to my wonderful friends Ebrahim Rezaei, Mohsen Shakouri, Ji Li and Mehdi Tajallipour who have been generous with their help and support during my study at the University of Saskatchewan.

DEDICATION

This thesis is dedicated to my lovely wife, Mojgan Rezaei, who has always stood by me and dealt with all of my absence from many family occasions with a smile. She is the one who made sacrifices during each step of this long journey with her tremendous love, unlimited support, great encouragement and understanding.

TABLE OF CONTENTS

LIST OF TABLES

LIST OF FIGURES

NOMENCLATURE

a	Interfacial area per unit volume of the reactor, m^2/m^3
C_A	Concentration at any point in the reactor, mol/m^3
C_A'	Equilibrium concentration of A at the interface of gas and liquid, mol/m^3
C_t	Total concentration in the liquid phase, mol/m^3
C_{Ai}^*	Equilibrium concentration of A (i=1 inlet, i=2 outlet of the reactor), mol/m^3
D_A	Diffusivity of A in the gas phase, m^2/s
D	Distribution coefficient
$\overline{ex}^{ch}$	Molar chemical exergy, kJ/kmol
$\overline{ex}^{phys}$	Molar physical exergy, kJ/kmol
$\overline{ex}$	Total exergy, kJ/kmol
$\overline{ex}_{destruction}$	Destroyed exergy, kJ/kmol
Δex_{system}	Exergy difference, kJ/kmol
F_G	Molar flow rate of inert in the gas phase, mol/s
F_L	Molar flow rate of inert in the liquid phase, mol/s
g	Standard gravity, $9.81\ m/s^2$
$\Delta_f g^o_{j,298.15}$	Molar Gibbs free energy of formation, kJ/kmol
H	Total enthalpy, kJ
H_A	Henry's coefficient, $Pa.m^3/mol$
$\bar{h}$	Molar enthalpy, kJ/kmol
$\bar{h}_o$	Molar enthalpy at reference state, kJ/kmol
$\bar{h}_f^o$	Molar enthalpy of formation, kJ/kmol

k_G	Mass transfer coefficient in the gas phase, mol/m^2.Pa.s
k_L	Mass transfer coefficient in the liquid phase, m^3/(m^2.s)
$K_G.a$	Overall mass transfer coefficient in the gas phase, mol/m^3.Pa.s
$K_L.a$	Overall mass transfer coefficient in the liquid phase, 1/sec
K_{eq}	Equilibrium constant
N_A	Rate of straight mass transfer at any point in the reactor, mol/m^2.s
n	Number of moles, kmol
P_A	Partial pressure of A in the bulk of gas, Pa
P_A'	Partial pressure of A at the interface of gas and liquid, Pa
P_t	Total pressure in the gas phase, Pa
Q	Heat, kJ
Q_G	Volumetric gas flow rate, mL/min
Q_L	Volumetric liquid flow rate, mL/min
$\overline{S}$	Molar entropy, kJ/kmol·K
$\overline{S}_o$	Molar entropy at reference state, kJ/kmol·K
$\overline{S}_f^o$	Molar entropy of formation, kJ/kmol·K
T	Temperature, K
T_o	Reference-environment temperature, K
T_F	Final temperature of each step, K
V	Velocity, m/s
V_r	Reactor volume, m^3
y_{SO_2}	mole fraction of SO_2 in the gas phase

z	Elevation, m
z	Film thickness, m
Z	Coordinates, m

Greek Letters

η_{ex}	Exergy efficiency
τ	Residence time, s

Subscripts

f	Formation
F	Final state
o	Reference state
P	Products
R	Reactants

Superscripts

$\dot{}$ (over dot)	Quantity per unit time
$\bar{}$ (over bar)	Quantity per unit mole
^{o}	Standard reference states

Abbreviations

GA	General Atomics
G1-AFR	G1 Standard Evaluation Advanced-Flow Reactor
LF-AFR	Low Flow Advanced-Flow Reactor
SMR	Steam Methane Reforming
S-I	Sulfur-Iodine
TCD	Thermal Conductivity Detector
UV-Vis	Ultraviolet-Visible Spectrophotometer

CHAPTER ONE

INTRODUCTION

1.1. Research background and motivation

There is an increasing demand for energy consumption worldwide. Most of the energy supply has been provided by fossil fuels so far. The long-term effects of such a huge dependency on fossil fuels are detrimental to the environment in the forms of air pollution and global warming. The uncertainty of oil prices, due to the ongoing crisis in the Middle East, is also a noticeable concern from an economics point of view. Therefore, the development of hydrogen production technologies has been a global focus in order to overcome the current fears and to improve energy and economic security [1].

The annual rate of hydrogen production is about 38 million tonnes worldwide, a market valued at about $60 billion. Most of this hydrogen (90%) is used for heavy oil upgrading, desulfurization and upgrading of conventional petroleum, and for production of ammonia. There is also a projected demand for H_2 as a transportation fuel and portable power source. The current rate of hydrogen production in Canada is 3.4 million tonnes/year. It is estimated that this demand will likely be 5.9–6.9 million tonnes/year by 2020 [2]. To produce hydrogen, several methods have been employed from either fossil feedstocks such as natural gas and coke or renewable resources such as biomass and water powered by renewable energy sources (e.g. sunlight, wind, wave or hydro-power). These processes include the use of chemical, biological, electrolytic, photolytic and thermochemical technologies. Depending on the feedstock availability, market applications and demand, government policies, cost, and the stage of development, each technology may offer many advantages or disadvantages [3].

Commercially, the first industrial process for hydrogen production dates back to the 1920s when electrolysis was used for the production of pure hydrogen. However, in the 1960s fossil fuel was first utilized as feedstock and has been used as the most important source of hydrogen production until the present [3]. About 60% of hydrogen is produced by steam methane reforming (SMR) of natural gas, which is responsible for the emission of about 30 million tonnes of CO_2 per year [2]. For this reason, many attempts have focused on the processes that use renewable energy sources. The thermochemical water-splitting cycle was considered as one of the best candidates for this purpose and was studied for a long time between 1970 and 1980. A large number of unique cycles were proposed and various experiments have been performed to optimize the operating conditions of the reactions within the cycles. Among these cycles, the sulfur-iodine (S-I) water-splitting cycle absorbed a lot of attention especially after massive research and investment by General Atomic (GA) Company. The following reactions are included [4]:

$$2H_2O + I_2 + SO_2 \rightarrow H_2SO_4 + 2HI \ (120\ ^oC) \quad (1\text{-}1)$$

$$2HI \rightarrow I_2 + H_2 \ (300\text{-}450\ ^oC) \quad (1\text{-}2)$$

$$H_2SO_4 \rightarrow H_2O + SO_2 + 0.5O_2 \ (830\text{-}900\ ^oC) \quad (1\text{-}3)$$

And, the overall reaction is:

$$H_2O \rightarrow H_2 + 0.5O_2 \quad (1\text{-}4)$$

The GA Company's extensive research cost $8 million to investigate the different projects of this cycle. It revealed the conditions under which the products of the Bunsen reaction, as the

most critical step of this cycle, form two phases: sulfuric acid (upper phase), mainly a mixture of H_2SO_4 and water, and hydroiodic acid (lower phase), including HI, I_2 and water [5] where a large amount of iodine and water is required to avoid side reactions and to separate two acid products into two immiscible liquid phases according to the following stoichiometry [6-8]:

$$\begin{aligned} &SO_2 + 16H_2O + 9I_2 \rightarrow \\ &(2HI + 10H_2O + 8I_2)_{\text{HIx phase}} + (H_2SO_4 + 4H_2O)_{\text{Sulfuricacid phase}} \end{aligned} \quad (1\text{-}5)$$

In spite of the physical separation of the HI and H_2SO_4 phases in this method, some challenges are inevitable. Using excess water results in increasing capital and operating costs, and lowering the energy efficiency of the entire chemical loop because of the high heat duty for the concentration of both acids prior to decomposition [7]. In addition, a Bunsen reaction must be carried out at elevated temperatures (70-120 ^oC), leading to iodine vapour deposition in the set-up and tube blockage. At these temperatures, the severe corrosion of Bunsen reaction products is also a concern [9]. Therefore, experimental and theoretical research activities have been carried out during the last decade to minimize these challenges in the Bunsen reaction [10-13] as well as other technical difficulties related to reactions (1-2) and (1-3). For instance, in the HI decomposition section of S-I water-splitting cycle, the existence of the azeotropic point in the mixture of HIx phase makes the separation difficult before decomposition. Low equilibrium conversion of HI (ca 20% at 400 ^oC) is also an obstacle. When it comes to sulfuric acid decomposition of S-I water-splitting cycle, a high temperature is needed to decompose H_2SO_4 thermally in the first stage. In addition, the need for active and stable catalysts in the second stage adds more complexity to this cycle, especially at the commercialization stage.

Wang [14] proposed an H_2S splitting cycle based on the inspiration of the S-I water-splitting cycle. Accordingly, H_2SO_4, SO_2, H_2O, I_2 and HI are cycled within this process to produce one mole of H_2 and one mole of S from one mole of H_2S. Similarly, this cycle consists of the three chemical reactions:

$$H_2S + H_2SO_4 \rightarrow S + SO_2 + 2\,H_2O \ (120\text{-}150\ ^oC) \quad (1\text{-}6)$$

$$2H_2O + I_2 + SO_2 \rightarrow H_2SO_4 + 2HI \ (25\ ^oC) \quad (1\text{-}1)$$

$$2HI \rightarrow H_2 + I_2 \ (25\ ^oC) \quad (1\text{-}2)$$

The overall reaction is:

$$H_2S \rightarrow H_2 + S \quad (1\text{-}7)$$

The final goal of developing the H_2S splitting cycle is not limited only to hydrogen production. Heavy bitumen from the Canadian oil sands contains many impurities that need to be removed before the refining stage [2]. Steam methane reforming (SMR) is the main process that uses methane to produce the hydrogen used in hydrotreating. Hydrotreating is currently used in the oil industry to remove sulfur with hydrogen, forming hydrogen sulfide gas. A major concern for this process is the amount of sulfur left in the oil, which will poison the catalyst during refining [15]. Conventionally, H_2S is treated to produce elemental sulfur and water by the Claus process [16]. The hydrogen sulfide splitting cycle could benefit the petroleum industry by treating hydrogen sulfide gas and converting it to hydrogen, a more valuable product compared to elemental sulfur. This cycle has the potential to replace the Claus and SMR processes while

reducing the industrial demand for methane. Thermodynamic analysis revealed that the H_2S splitting cycle is more energy-efficient compared to the S-I water-splitting cycle since the endothermic sulfuric acid decomposition reaction of the S-I water-splitting cycle was replaced by the exothermic H_2S oxidation [14]. The Bunsen reaction is the most critical step in the H_2S splitting cycle as well as in the sulfur-iodine (S-I) water-splitting cycle for hydrogen production. A low-temperature process for the H_2S splitting cycle is proposed, where toluene is used to dissolve iodine and the Bunsen reaction could be carried out continuously at room temperature [17]. This low-temperature process avoids iodine vapour deposition and the side reactions, and it also eases the corrosion challenge. The subsequent electrolysis of the Bunsen reaction products relieves the worry about two acid separations as well. However, the use of an I_2-toluene solution leads to a gas-liquid-liquid multiphase reaction system where the improvement of cross-phase mass transfer becomes the key to the increase of process efficiency.

Corning® Advanced-Flow™ Reactors were used in this study because they are able to improve the gas-liquid mass transfer coefficients compared with other gas-liquid contactors, such as bubble columns and spray columns [18]. They are also made of glass or ceramic materials, which are highly corrosion-resistance to aqueous acid solutions. It is claimed that the modulus design of these reactors allows seamless scale-up from the lowest flow rate (10 mL/min) to highest flow (5000 mL/min) [19]. In addition, these reactors are believed to improve heat transfer for exothermic reactions, preventing either thermal degradation or explosive evolution [19-21]. In this dissertation, the H_2S splitting cycle was extensively studied in the Corning® Advanced-Flow™ Reactors by focusing on the Bunsen reaction to investigate mass transfer behaviours of the SO_2-water, SO_2-toluene binary systems. During this work, it was also realized that hydrogen could be produced from different sulfur-containing feedstocks as long as they can be converted into SO_2 to

feed the Bunsen reaction. Therefore, based on the H_2S splitting cycle and by performing an exergy analysis, various chemical reaction routes were proposed to make use of sulfur-containing compounds, which exist in different industry sectors as byproducts or waste products, to produce hydrogen. Finally, a hydrogen production plant was designed based on the hydrogen sulfide splitting cycle which was followed by an economic analysis of the designed plant.

1.2. The structure of this thesis

Following this chapter, Chapter 2 is a review of the literature regarding the widely studied S-I thermochemical water-splitting cycle as the basis of the advent of the H_2S splitting cycle. Chapter 3 specifically presents the research allocated to the H_2S splitting cycle in Dr. Hui Wang's research group. The chapter describes the contribution of this thesis toward the development of the process to identify the mechanism of the Bunsen reaction in the multiphase reaction system and the reaction rate-controlling step. The knowledge gaps and objectives are introduced after this. Experimental details, measurement techniques and analysis methods, mass balance and reproducibility of data are described in Chapter 4. Chapter 5 sets forth an exergy analysis, performed on different possible routes for SO_2 production to feed the Bunsen reaction, by presenting the chemistry of the routes and discussing their possible applications. Chapter 6 studies the liquid-side overall mass transfer coefficients for the SO_2-water and SO_2-toluene binary systems using Corning® Advanced-Flow™ Reactors. This was followed by measuring the SO_2 absorption rates for any combinations of SO_2-water-toluene mixture. Chapter 7 illustrates the investigation of the Bunsen reaction in the presence of toluene as the solvent for iodine, where the effects of operating conditions on the SO_2 absorption and I_2 reaction rates were studied in Corning® Advanced-Flow™ Reactors. Chapter 8 presents a hydrogen production plant design based on the H_2S splitting cycle with the cooperation of an undergraduate student group (H_2S solution) followed

by an economic analysis of the designed plant. Finally, in Chapter 9, overall conclusions are presented and recommendations are given for future work.

It is noteworthy to mention that some parts of this work have been either published or ready for submission as follows:

1. **Moniri A**, Wang H. Mass transfer study of the Bunsen reaction in the H_2S splitting cycle using Corning® Advanced-Flow™ Reactors. Manuscript ready to be submitted to the *International Journal of Hydrogen Energy*.

2. **Moniri A**, Wang H. Study of the Bunsen reaction in the H_2S splitting cycle using Corning® Advanced-Flow™ Reactors. Manuscript ready to be submitted to the *International Journal of Hydrogen Energy.*

3. **Moniri A**, Wang H, Morien C, Lewis J, Smith B, Clarkson C. A Plant Design for Hydrogen Production through the H_2S-H_2O splitting cycle using Corning® Advanced-Flow™ Reactors. Manuscript ready to be submitted to the *Journal of Chemical Engineering Technology*.

4. Li J, **Moniri A**, Wang H. Apparent kinetics of a gas–liquid–liquid system of Bunsen reaction with iodine-toluene solution for hydrogen production through H_2S splitting cycle. *International Journal of Hydrogen Energy*. 2015;40:2912-20.

5. Wang H, Le Person A, Zhao X, Li J, Nuncio P, Yang L, **Moniri A**, Chuang K. A low-temperature hydrogen production process based on H_2S splitting cycle for sustainable oil sands bitumen upgrading. *Fuel Processing Technology*. 2013;108:55-62.

6. **Moniri A**, Mertins P, Wang H. Exergy analysis of hydrogen production from different sulfur-containing compounds based on H_2S splitting cycle. *International Journal of Hydrogen Energy*, 2012;37:15003-10.

As author of this thesis, I was the major contributor to the first, second and third manuscripts and also the sixth published paper, thus my name leads those lists of authors. I also made significant contributions to the fourth paper. I did the literature review, experimental set-up preparation, design and development of the analysis methods, conducting of experiments, interpreting of results, and writing and revision of the manuscripts. Dr Hui Wang was in charge of

the supervision of the thesis, providing feedback on the manuscripts, and handling the submission process of the papers.

CHAPTER TWO

LITERATURE REVIEW

This chapter reviews the development history of the thermochemical water-splitting cycles for hydrogen production leading to the introduction of the widely studied sulfur-iodine (S-I) thermochemical water-splitting cycle. In the context of the S-I water-splitting cycle, the main sub-reactions are reviewed by describing the common production methods to identify advantages, disadvantages and common challenges encountered by utilizing the conventional reaction schemes. The main focus of this chapter is on the literature pertaining to the key step of the S-I water-splitting cycle (the Bunsen reaction) that either investigates improving the commonly studied stoichiometry by phase separation or proposes alternative methods with the aim of avoiding technical difficulties.

2.1. Thermochemical water-splitting cycles

As mentioned earlier, fossil fuel has been the major feedstock of hydrogen production for many years, but this fact has not stopped many researchers from pursuing alternative processes that use renewable energy sources [3].

By definition, the theoretical work in any electrochemical process is the change in the Gibbs energy. The entropy change is also defined as the negative of the temperature derivative of the Gibbs energy change. Due to the small value of entropy change at the standard condition, the direct decomposition of water by electrolysis seems to be almost impossible [5]. One-step, direct thermal decomposition of water is one of the most straightforward methods for splitting water to hydrogen but requires a temperature greater than 2500 ^{o}C to obtain reasonable quantities. However, from the commercial point of view this option is not economically viable [22].

By introducing a multi-reaction process, the Gibbs energy change can be reduced significantly, which may have the same results as modifying the equilibrium of the water decomposition reaction. In theory, the work requirement could possibly be reduced to zero at reasonable operating temperatures by decreasing the amount of heat required [5]. A water thermochemical cycle includes a series of thermally driven reactions in which water is decomposed to oxygen and hydrogen at relatively moderate temperatures. The chemicals used to decompose water are circulated, ideally consumed and regenerated continuously within the system. The major concern associated with a thermochemical cycle is to maximize the hydrogen production yield while decreasing the amount of excess agents used in the process. Solar or nuclear energy has been used as the primary source of heat input for these types of cycles to reduce dependence on fossils energy sources and to obtain the highest possible energy consumption efficiency [22].

Extensive research was started between the 1970s and 1980s to find the most efficient chemical processes for hydrogen production worldwide by which the water decomposition reaction could be feasible [5]. The initial major program was directed by the Joint Research Centre (JRC) of the European Community, which began in the late 1960s and ended in 1983 at Ispra, Italy. The program investigated a direct hydrogen production route from water, using nuclear heat, to identify and develop the most appropriate thermochemical cycles. Water electrolysis was used as the reference technology and the primary energy source was also selected to be high temperature heat from a portable nuclear reactor so that water could be split into the required amount of hydrogen. According to the thermodynamic calculations and kinetics data, many process flow sheets and equipment designs were prepared for the thermochemical water-splitting cycles to meet the criteria. These included appropriate thermal efficiency, high availability and low cost of chemicals involved, easy separation and handling of materials, and high conversion of the

chemical reactions. Negatives to avoid included a high process temperature, side reactions, toxicity of the elements involved, corrosion, and heat and mass transfer challenges [5].

In the first place, mercury, manganese and vanadium-based cycles were studied. Later, another nine cycles were proposed based on the iron-chlorine families. Lastly, sulfur-iodine cycles were introduced. For instance, Marchetti and De Beni [23] proposed a cycle named Mark 1 at Ispra, which was based on mercury as the cycling agent, but the presence of mercury by itself was the biggest obstacle for commercializing this process. The iron-chlorine family of cycles named Mark 15 was also presented by Knoche et al. [24] where thermal decomposition of $FeCl_3$ and hydrolysis of $FeCl_2$ were identified as the most problematic issues of this cycle. Besides, the economics were not appealing even though the iron-chlorine cycles were chemically feasible [5]. Despite many attempts to overcome difficulties, no practical solution was found for most cycles described here and eventually the majority of them were abandoned.

Sulfur-iodine as the last cycle of the sulfur family, presented as Mark 16, absorbed great attention as it offered a higher thermal efficiency compared to the other proposed cycles. Later, the intensive research on this cycle resulted in the laboratory demonstration loops internationally [22]. Recently, the versatility of the S-I water-splitting cycle has allowed researchers to switch from lab-scale production toward bench and pilot plant test facilities, although no industrial plant has been constructed so far. Some of the international lab-scale facilities include Japan Atomic Energy Agency's (JAEA) glass apparatus (30 L/h) in 2004 [25], the integrated test facility by the cooperation of General Atomics (GA), Sandia National Laboratory (SNL), and Commissariat a` l'Energie Atomique (CEA) (200 L/h) in 2008 [26], and also Korea Atomic Energy Research Institute (KAERI) (3 L/h), Institute of Nuclear and New Energy Technology, Tsinghua University

(INET) (10 L/h) and Italian National Agency for New Technology, Energy and Environment (ENEA) (10 L/h), in 2010 [27-29].

2.2. Sulfur-Iodine thermochemical water-splitting cycle

The S-I water-splitting cycle, which was initially developed by General Atomics (GA) Company in the US [4], includes the following reactions:

$$2H_2O + I_2 + SO_2 \rightarrow H_2SO_4 + 2HI \ (120\ ^oC) \quad (2\text{-}1)$$

$$2HI \rightarrow I_2 + H_2 \ (300\text{-}450\ ^oC) \quad (2\text{-}2)$$

$$H_2SO_4 \rightarrow H_2O + SO_2 + 0.5O_2 \ (830\text{-}900\ ^oC) \quad (2\text{-}3)$$

The Bunsen reaction (2-1) must be carried out at elevated temperatures so that I_2 could be sufficiently dissolved in water. With proper amount of excessive water and iodine, two immiscible acid phases are produced, which should be separated, purified and concentrated in order to be decomposed in the reactions (2-2) and (2-3). The decomposition of HI results in the production of hydrogen while sulfuric acid decomposition provides SO_2 for the Bunsen reaction, which result in the splitting of 1 mole of water into 0.5 mole of oxygen and 1 mole of hydrogen [22]. In practice, some chemicals need to be used in excess and this results in a significant upgrading in the downstream before decomposition reactions occur. Therefore, in the following subsections, each reaction of the S-I water-splitting cycle are separately reviewed to identify the main technical problems that impede the development of this cycle on an industrial scale.

2.2.1. The Bunsen reaction

Reaction (2-1), known as the Bunsen reaction in the S-I water-splitting cycle, is a moderately exothermic reaction, which is believed to be the most crucial part of this cycle because it links two other sections: the sulfuric acid and hydroiodic decomposition reactions. General Atomics (GA) Company extensively investigated this reaction in order to optimize the conditions under which two produced acids have the highest degree of separation. GA Company concluded that both acids are not separated by any thermal means without reversing the equilibria unless excess amounts of water and iodine are used [4]. The GA stoichiometry is shown as follows:

$$\begin{aligned} &SO_2 + 16H_2O + 9I_2 \rightarrow \\ &(2HI + 10H_2O + 8I_2)_{\text{HIx phase}} + (H_2SO_4 + 4H_2O)_{\text{Sulfuricacid phase}} \end{aligned} \qquad (2\text{-}4)$$

According to GA stoichiometry, considerable excess amounts of iodine (9 moles) and water (16 moles) are required to drive the splitting of the acids through a spontaneous phase separation process. These over-stoichiometry amounts of water and iodine create two immiscible phases: a light H_2SO_4/H_2O and a heavy $HI/I_2/H_2O$ phase, which must be concentrated before each is sent for decomposition. The separation steps would become a huge burden later in the downstream sections as the diluted streams need to be concentrated and purified. The consumption of energy for heating, cooling, pumping and separating results in a decrease of the overall efficiency of the cycle [6, 30-32]. The theoretical limit of the efficiency for the total process is estimated to be 51% assuming ideal reversible reactions [4]. The best estimate was 33–36% based on the GA flow sheet analysis in 1982 [33]. Liberatore et al. [34] at ENEA assessed the energy and economics of an industrial plant powered by concentrated solar energy. They report an

efficiency of 34% while a total heat-to-hydrogen efficiency of 21% was obtained with a hydrogen production cost of about 8.3 €/kg. Leybros et al. [35] at CEA estimated 12 €/kg of hydrogen based on the analysis conducted for a sulfur-iodine cycle coupled to a nuclear heat source. In all cases, increasing the amount of excess water and iodine used in the process decreased plant efficiency.

Depending on the operating conditions and stoichiometry, undesirable hydrogen sulfide and elemental sulfur formation in reactions (2-5) and (2-6) may also lower the plant efficiency [32].

$$6HI+H_2SO_4 \leftrightarrow S+3I_2+4H_2O \quad (2\text{-}5)$$

$$8HI+H_2SO_4 \leftrightarrow H_2S+4I_2+4H_2O \quad (2\text{-}6)$$

Sakurai et al. [9] investigated the operating conditions under which the above reactions are dominant: Both reactions proceed at a higher temperature, higher acid concentrations and low iodine excess. However, reaction (2-6) is favoured between 295 K and 368 K over reaction (2-5), and the opposite under low iodine excess. The minimum value of 3.4 mole I_2/mole H_2SO_4 was selected to avoid side reactions. Similarly, a value of 3.9 and 4 mole I_2/mole H_2SO_4 was suggested by Giaconia et al. [6] and Lee at el. [36], respectively. As can be seen, the occurrence of the side reactions in the Bunsen reaction mixture affects the process efficiency significantly and avoiding them is crucial for the process optimization.

Despite many attempts for optimization of the GA stoichiometry, the detailed mechanism of the Bunsen reaction is not well understood. Initially, GA believed that the formation of tri-iodide was necessary for the Bunsen reaction to occur. Giaconia et al. [30] and De Beni et al. [10] show that a complete reaction is possible when iodine is selected to be the limiting reagent, which

contradicts the GA thermodynamics calculations. Later, GA admitted that ΔG was wrongly calculated by the HSC Chemistry program. Correcting the calculations, ΔG was negative both with or without a tri-iodide ion [32]. Calabrese and Khan [37] studied the aqueous solution of iodine in the presence of KI. They noticed the formation of I_3^- ions and a number of protonated poly-iodine complexes while no I_5^- or I_7^- ions were found in the solution. Later, based on Raman's experimental tests, Spadoni et al. [38] found that the chemistry of ternary mixtures of HI–I_2–H_2O was highly dependent on I_2:HI molar ratio. They noticed that up to a 1:1 ratio, I_3^- and its corresponding ion pair HI_3^- were the dominant iodine compounds while at higher values, the formation of higher poly-iodine and poly-iodide compounds were certainly possible. The following subsection describes the improvements performed so far to the Bunsen reaction to optimize GA stoichiometry.

2.2.1.1. Optimizing the stoichiometry and phase separation behaviours

Most researchers have tried to improve the Bunsen reaction phase separation by varying iodine and water contents as well as the reaction temperature. Among them, the most comprehensive study was done by Lee et al. [36] where an optimal operating window of 4–6 mole excess iodine and 11–13 mole excess water within a temperature range of 330–350 K was proposed according to experimental data collated from literature as well as their own experiments. This avoided side reactions and increased the HI concentration above the azeotrope. Compared to the GA stoichiometry, reducing iodine content resulted in operating below the solidification point of iodine. Giaconia et al. [6] also investigated the LLE phase separation behaviour of products of the Bunsen reaction. It was understood that temperature and I_2 content have almost no effect on the sulfuric acid and HI concentrations in the two phases unless using a huge amount of iodine at

120 ºC. They suggested the molar ratio of $HI/H_2O/I_2/H_2SO_4$=0.11/0.61/0.22/0.06 to run the Bunsen reaction at a relatively mild temperature whilst using the lowest iodine excess. Maatouk et al. [39] studied quaternary $H_2SO_4/HI/I_2/H_2O$ mixtures and discovered that an increase in iodine concentration and a decrease in water concentration modified the LLE phase separation, however, too low a concentration of water promotes undesired reactions. Guo et al. [40] studied the purification of sulfuric acid and HI by reverse Bunsen reaction in continuous mode in a packed column. An increase in temperature promoted purification of the HIx phase as almost all I^- in the H_2SO_4 phase was found to be removed at temperatures over 140 °C. Zhu et al. [41] investigated the effects of the solution composition in the quaternary $H_2SO_4/HI/I_2/H_2O$ feed as well as the operating temperature. They showed that the increases in both the iodine content and temperature reduced impurities in both phases by avoiding side reactions, however, the effect of the iodine content was more significant compared to temperature. They also achieved the concentrations of HI in the HIx phase above the azeotropic composition. Parisi et al. [31] also conclude that the separation of the two phases was quite slow at temperatures lower than 35 °C, unless a great excess of water was used. They also mention that the sulfates from the HIx phase could be quantitatively removed when both the temperature and the iodine content were high enough. In this case, the secondary reactions were negligible. As can be seen, even though all conditions are optimized, excess amounts of reactants are required. Therefore, alternative methods have been proposed to run the Bunsen reaction to avoid the GA over-stoichiometry reaction scheme as discussed below.

2.2.1.2. Alternative methods to run the Bunsen reaction

The use of solvent has been considered for running the Bunsen reaction to avoid the large excess of water in the GA reaction scheme. In fact, when excessively used, water could play the role of both reagent and solvent, allowing separation of HI and H_2SO_4 into two immiscible phases

without the use of a large excess of iodine, minimizing the cost of recovery in the downstream section and leading to an increase in process efficiency. Also, the effect of material corrosion occurring in the HI–H_2O azeotropic mixture recovery can be minimized. On the other hand, despite reducing the amount of water used in the GA stoichiometry, to drive the reaction thermodynamically, an excess amount of water is always needed. To replace water, the candidate solvent must dissolve the Bunsen reaction reagents (I_2, SO_2 and H_2O), resulting in a desired recovery of H_2SO_4 and HI [30]. Initially, De Beni et al. [10] and later Giaconia et al. [30] used tri-n-butyl phosphate (TBP) as a solvent for the Bunsen reaction. TBP was able to dissolve SO_2, iodine and water acceptably. The excess quantity of water created two inseparable phases: a heavier phase (H_2SO_4 phase, which was more dilute than that in the GA process) containing H_2SO_4 and H_2O and a lighter phase (TBP phase where the composition of HI was significantly higher than the azeotrope) including non-dissolved SO_2, HI, H_2O and TBP. As TBP formed a complex with HI, a complete reaction occurred preventing side reactions with SO_2 from taking place. At the end, the separation of TBP from HI became the main concern because the thermal means caused solvent degradation. Although backwashing the HI-TBP was possible with an excess of water, the HI solution produced was extremely dilute at ~1.5 wt%. Thermal means and a membrane separation could possibly have been used to overcome the azeotrope, but the thermal energy required was too significant for the process to be feasible [42]. Taylor et al. [43] studied the products of the Bunsen reaction by using dibutylbutylphosphonate (DBBP) and Cyanex® 923 as a replacement for TBP. They observed that the performance of both DBBP and Cyanex® 923 were relatively better than TBP in terms of HI extraction, H_2SO_4 extraction, SO_2 solubility and iodine solubility. However, the recovery of the HI was not successful from DBBP due to breakage of the solvent, similar to TBP. On the other hand, small amounts of HI were recovered from Cyanex® 923 using distillation.

Backwashing the HI loaded Cyanex® 923 was also barely successful. Later, Taylor et al. [44] investigated the performance of Cyanex® 923 on the real Bunsen reaction products. They conclude that Cyanex® 923 may outweigh using TBP since it reduced the quantity of excess water required to drive the reaction forward from 18 mole of excess water with the TBP to a 4 mole excess with the Cyanex® 923. However, they failed to recover HI in any significant quantity. Barbarossa et al. [45] proposed polystyrene-divinyl-benzene (PSDVB) as an alternative solvent for the Bunsen reaction. The PSDVB, an aromatic polymer, captured the sulfuric acid so that a sulfunic polymer (S-PSDVB) was formed, which could later be separated by filtration. A sulfuric acid recovery of around 56% was found using this method. However, this value was too low to be used in an industrial process. An imidazolium-based ionic liquid was used as a reaction medium instead of water, based on its high solubility for SO_2, I_2, and adjustable miscibility with water to avoid the azeotropic HI-H_2O mixture [46]. Although the initial low-temperature Bunsen reaction was successfully performed, no HI was detected in the gas phase, and instead the reaction evolved H_2S gas, which led to the investigation of a new Sulfur-Sulfur thermochemical cycle. Taylor et al. [32] studied three subsets of ionic liquids, namely the $[FAP]^-$, $[Tf_2N]^-$ and $[TMPP]^-$ for use in the Bunsen reaction, mainly for investigation of their HI extraction potential. Despite having high thermal stability, the ionic liquids tested were not suitable for use in the Bunsen reaction.

In addition to organic solvents, other methods have been employed. Nomura et al. [11, 12] first proposed an electrochemical cell for the Bunsen reaction equipped with a cation-exchange membrane as the separator, using sulfuric-acid-dissolving sulfur dioxide as the anolyte and hydriodic-acid-dissolving iodine as the catholyte. Runs were performed at temperatures between 40 °C and 90 °C. They observed that both HI and H_2SO_4 were at higher concentrations than reported in literature for the liquid–liquid separation. During the Bunsen reaction operation, a 93%

reduction in iodine and a 69% reduction in water were recorded. Without electricity recovery from the waste heat, optimizing HI and H_2SO_4 concentrations allowed a thermal efficiency achievement of 42.1%. Immanuel et al. [47, 48] and Gokul et al. [49] indicate the absence of any side reaction at the electrodes, however cross-contamination of anolyte and catholyte solutions was observed by the presence of iodide ions in the anolyte and sulphate ions in the catholyte. Similarly, Giaconia et al. [30] observed a significant reduction in iodine concentration and cross-contamination in both compartments.

The addition of a precipitating agent to the Bunsen reaction products is another alternative to separate HI from the heavier phase, which was investigated by Giaconia et al. [30]. Adding lead sulfate to react with HI allowed iodide precipitation in the form of lead iodide from the reaction environment. In this way, pure anhydrous HI could be removed by treatment with phosphoric acid. Although, a significant reduction in excess iodine was observed, handling large amounts of solids was a concern as the phosphoric acid concentration step became very energy-intensive. As observed, so far no suitable process has been found to separate the Bunsen reaction products in an efficient way. In the following section, the processes in which the HI phase is decomposed are reviewed.

2.2.2. HIx decomposition section

In order to produce hydrogen, the heavier phase resulting from the Bunsen reaction must be purified and recycled back to the Bunsen reaction section. This endothermic reaction (2-2) (300–450 ^{o}C) is believed to be the most challenging step because of the presence of an azeotropic point in the HI_X mixture that prevents simple distillation. The extraction of HI from the HI_X mixture is also energy-demanding due to the high volume of water. The low equilibrium conversion of this reaction (ca 20% at 400 ^{o}C) is another concern [50]. To decompose HI from the

Bunsen reaction products, three major methods have been employed so far: extractive distillation, reactive distillation and electro-electrodialysis.

Two flow sheets were proposed by GA to use phosphoric acid for extracting water from the HIx phase in an extractive distillation. Applying this method, the existence of phosphoric acid first led to separation of iodine. Separation of HI then easily occurred from the mixture by a simple distillation. In the gaseous (or possibly liquid) phase, HI was finally decomposed and separated by using membranes [50]. The cost estimate indicates that 40 % of the total capital cost was due to the phosphoric acid extraction step as it consumed a large amount of heat and electricity [33].

A reactive distillation was initially developed by Roth and Knoche in Germany in which HI was decomposed directly from a ternary liquid $H_2O/HI/I_2$ solution under high pressure and temperature. A gas-liquid equilibrium was subsequently formed in the middle of the column, and the solubilized iodine in the lower liquid phase was removed from the bottom while a mixture of gaseous H_2 and water was recovered at the top of the column [51]. However, the need for very high pressure (up to 22 bar) [51], lack of thermodynamic data for design of the column [50] and more importantly, the design of corrosion-resistant materials to handle the corrosive mixture of HI and iodine in such harsh operating conditions, became serious obstacles for commercialization. The use of a catalyst allows a noticeable temperature reduction to achieve acceptable reaction rates [52]. Catalytic decomposition of HI gas on platinum wire was initially reported by Hinshelwood et al. [53]. Recently, several groups [52, 54-66] have studied various transition metals as catalysts for the HI decomposition reaction such as Ni, Mo, Pd, Ir, Ru, Rh and Pt by comparing their activities on various supports such as zeolites, hydrophobic supports, active carbon, and so on. Among them, platinum group metals supported on activated carbon or γ-Al_2O_3 were found to have the highest activities [62]. It was understood that the source of carbon and its preparation method

significantly affected the surface characteristics indicating catalytic activity and stability. The presence of platinum was also found to magnify the catalytic activity while preventing adsorption of iodine on the catalyst surface [67].

Another alternative method is called the Electro–electrodialysis (EED) process, which breaks the HI–H_2O azeotrope featuring an ion exchange membrane to increase HI molality of the HIx solution leading to the efficient separation of HI. Onuki et al. at Japan Atomic Energy Research Institute (JAERI) [68, 69] studied the concentration of HI using polymeric membranes at elevated temperatures. However, high electric resistance of the anion exchange membrane was identified as a negative point. JAERI improved the HI concentration process by using electro-electrodialysis (EED) as well. It was proved that the electrical energy demand of EED to produce hydrogen of 1 mole was 69.8 kJ/mol-H_2, which was lower than that of the steam recompression in the GA process [70]. The corrosive mixture of iodine-iodide solution, the high demand for catalyst development and the extensive need for the separation and purification of the downgraded acid are the most challenging factors of this section. The last step of the S-I water-splitting cycle is briefly described as follows.

2.2.3. H_2SO_4 decomposition section

Sulfuric acid, as the most well-known section of the S-I water-splitting cycle, is decomposed smoothly with almost no side reactions in two endothermic stages based on the following reactions [4]:

$$H_2SO_4(g) \rightarrow H_2O(g) + SO_3(g) \quad (450\ ^\circ C) \tag{2-7}$$

$$SO_3(g) \rightarrow SO_2(g) + 0.5O_2(g) \quad (800–900\ ^\circ C) \tag{2-8}$$

Sulfuric acid could be decomposed to its anhydride SO_3 with or without a catalyst, while the decomposition of SO_3 proceeded in the presence of a catalytic reaction [71]. Sulfur dioxide, water and iodine were then recycled to the Bunsen reaction section. The activity of metal or metal oxide components in the sulfuric acid decomposition is reported as follows [72, 73]: Pt $=Cr_2O_3 > Fe_2O_3 > CeO_2 > Al_2O_3$. To improve the mono-metallic/metal oxide catalysts, the bi- or tri-metallic catalysts have also been studied so that the corrosion of catalyst components at a temperature lower than 850 °C can be minimized. Even though all parameters were fully optimized, the energy requirements to concentrate diluted sulfuric acid from the previous section, the need for active and stable catalysts and, most importantly, corrosion are the highlighted challenges to be faced in this section.

2.3. Summary

In this chapter, sulfur-iodine cycle, as the most widely studied thermochemical water-splitting cycle, was reviewed. Despite the extensive research, the S-I water-splitting cycle still suffers from many obstacles, which decrease the whole process efficiency making the commercialization phase more difficult. The mixture of highly corrosive acids plus iodine dictated using highly corrosion-resistant materials, which in turn could be a financial burden for process optimization. In addition, since the long-term effects of such a corrosive environment have never been studied, the reaction medium could also become corroded gradually in the course of time imposing the consideration of high capital cost investment. To drive the Bunsen reaction thermodynamically, an elevated temperature was also required and this led to iodine deposition in the tubes, which was responsible for the set-up blockage. Besides, the side reactions were almost unavoidable even though the most optimized operating window was selected. The excess amount

of water is another challenging issue because it made more diluted phases downstream resulting in less efficient upgrading. Therefore, a new approach is required to overcome the described challenges in the S-I water-splitting cycle. The next chapter introduces a low temperature process for hydrogen production, which has been developed according to the S-I water-splitting cycle in Dr. Hui Wang's research group.

CHAPTER THREE

A LOW-TEMPERATURE HYDROGEN PRODUCTION PROCESS BASED ON THE H_2S SPLITTING CYCLE FOR SUSTAINABLE OIL SANDS BITUMEN UPGRADING

This chapter summarizes the experimental and theoretical studies that led to the development of a low-temperature hydrogen production process called the hydrogen sulfide splitting cycle, based on the sulfur-iodine thermochemical water-splitting cycle, previously reviewed in Chapter 2. The new cycle is capable of converting waste hydrogen sulfide from Canadian oil sands bitumen upgrading into hydrogen as a value-added product. The contribution of this thesis to the previous works done in Dr. Hui Wang's research group is also briefly presented. These attempts resulted in the co-authorship of two published journal papers in *Fuel Processing Technology Journal* and the *International Journal of Hydrogen Energy* as described in Chapter 1. My contributions to these two papers are the following: (1) identifying the SO_2 dissolving mechanism in the Bunsen reaction multiphase system and calculating the equilibrium constant between iodine and iodide species in the presence of toluene, (2) conducting the Bunsen reaction using a batch reactor to help an M.Sc. student realize the rate controlling step in the multiphase system. The efforts later directed the focus toward the study of the Bunsen reaction as the key step of both H_2S splitting and S-I water-splitting cycles in the continuous mode using Corning® Advanced-Flow™ Reactors, which is extensively discussed in Chapters 7 and 8.

3.1. H_2S Splitting Cycle

Based on the inspiration of the S-I water-splitting cycle, Wang [14] proposed the following cycle. The only difference is that the sulfuric acid decomposition reaction was replaced with the reaction between H_2S and sulfuric acid. This cycle consists of three chemical reactions:

$H_2S + H_2SO_4 \rightarrow S + SO_2 + 2\ H_2O$ (120–150 ^oC) (3-1)

$2H_2O + I_2 + SO_2 \rightarrow H_2SO_4 + 2HI$ (25 ^oC) (3-2)

$2HI \rightarrow H_2 + I_2$ (25 ^oC) (3-3)

The overall reaction is:

$H_2S \rightarrow H_2 + S$ (3-4)

If elemental sulfur continues to be further oxidized into SO_2:

$O_2 + S \rightarrow SO_2$ (3-5)

The reactions (3-2) and (3-3) would occur in doubled scale, thus giving rise to another new cycle called the H_2S-H_2O splitting cycle, represented by the following reactions:

$H_2S + H_2SO_4 \rightarrow S + SO_2 + 2H_2O$ (3-1)

$O_2 + S \rightarrow SO_2$ (3-5)

$2SO_2 + 4H_2O + 2I_2 \rightarrow 4HI + 2H_2SO_4$ (3-6)

$4HI \rightarrow 2H_2 + 2I_2$ (3-7)

The overall reaction is:

$H_2S + O_2 + 2H_2O \rightarrow H_2SO_4 + 2\ H_2$ (3-8)

The overall reaction (3-8) shows that one mole of oxygen and two moles of water react with one mole of H_2S in the feed stream to produce one mole of hydrogen and one mole of sulfuric acid, which is economically favoured over the basic H_2S splitting reaction (3-4). Using thermodynamic data, Yu et al. [74] studied the upper limit of the thermal efficiency of the H_2S splitting cycle and H_2S-H_2O splitting cycle (as described above) and compared the results with the work done by Goldstein et al. [75] for the sulfur-iodine water-splitting cycle. They found that the upper bound of thermal efficiency was 0.41 for the H_2S splitting and 0.36 for the H_2S-H_2O splitting, which were lower than that of the sulfur-iodine water-splitting (0.51) [75]. However, by exclusively considering the external energy that meets the requirement of heat and work for reactions and pumping, higher values for the thermal efficiency, 0.66 and 0.70, respectively, were obtained. Regardless of having higher thermal efficiency compared to the S-I water-splitting cycle, the H_2S splitting cycle is carried out at milder temperatures and has more potentials for higher heat recovery which could be coupled with the primary heat source easier. The following sections briefly review the literature regarding each reaction pertaining to the H_2S splitting cycle. Also reviewed is my contribution, mainly the investigation of the Bunsen reaction, which is not only beneficial to the H_2S splitting cycle but also to the S-I water-splitting cycle to avoid problematic issues affecting optimization of the whole process.

3.2. Reaction between H_2S and H_2SO_4 (H_2S oxidation)

Originally, Wang et al. [76-79] studied reaction (3-1), the first reaction in the H_2S splitting cycle, for the feasibility of H_2S removal using sulfuric acid. The following side reaction, seen in the Claus process, is inevitable when H_2S contacts the H_2SO_4 solution [76]:

$$2H_2S + SO_2 \rightarrow 3S + 2H_2O \quad (3\text{-}9)$$

To avoid reaction (3-9), the conditions that maximize the SO_2 production reaction (3-1) were studied [80]. Kinetic studies showed that reaction (3-1) is favoured over reaction (3-9) in a concentrated sulfuric acid solution where SO_2 is mainly produced [77, 78]. The continuous operation of the reaction between H_2S and H_2SO_4 at various concentrations was also studied [79] in a packed-bed or trickle-bed column reactor to determine mass transfer behaviour, the wetted packing surface area and the rate-determining step between reaction (3-1) and mass transfer. The results at the studied temperatures and sulfuric acid concentrations show that the rate-determining step can be identified by comparing the mass transfer coefficient and the specific reaction rate as the gas-side mass transfer and the reaction alternatively controlled. The wetted interface area of the packing (ceramic Raschig rings) was also determined by an empirical correlation developed by Onda et al. [81]. At the end, it was found that the separation of sulfur and the spent acid was possible as they did not contaminate each other and were easily separated by phase separation at a temperature above 120 ^oC. Therefore, the reaction (3.1) should be operated at temperatures higher than 120 ^oC to ensure that produced elemental sulfur stays in molten form, preventing the reactor from plugging. As can be seen, the first reaction of the H_2S splitting cycle is well studied and the operating conditions are fully optimized.

3.3. The Bunsen reaction in the multiphase gas-liquid-liquid system

The Bunsen reaction, the key step reaction of the sulfur-iodine water-splitting, and the H_2S splitting cycle, was studied in Dr. Hui Wang's research group to avoid the complexities and common challenges encountered in the GA reaction scheme [17]. Efforts have been made to select a suitable solvent for iodine so that this reaction could be easily run at ambient temperature to avoid excess quantities of iodine and water.

Based on the screening results, toluene was chosen as the solvent for I_2 due to its low toxicity, relatively high boiling point, low solubility in water, low level of reactivity with I_2, HI, and H_2SO_4, and relatively high solubility for I_2 [82]. In this way, the dissolved iodine could react with water and sulfur dioxide at low temperatures to mitigate severe corrosion, side reactions, and iodine vapour deposition that are normally occurred in conventional solvent-free routes. Nuclear Magnetic Resonance (NMR) spectroscopy was used to test whether halogenation would occur between toluene and iodine. NMR spectroscopy was taken for pure toluene as well as for the iodine-toluene solution and iodine-toluene-7.6 M hydroiodic acid solution mixtures after contacting for 24 hrs. No detectable iodotoluene was found in the mixtures.

During the Bunsen reaction, a multiphase reaction occurred when I_2-toluene contacted water. I_2 transferred from the toluene phase resulting in acid products (HI, and H_2SO_4) in the water phase. Initially, it was believed that the HI was released as the gas product after reaction completion and the H_2SO_4 stayed in the water phase leading to an easy separation from the organic phase. However, this idea contradicted the results of the HSC software and later the experimental studies since the Bunsen reaction acid products formed in the water phase after I_2-toluene reacted with water [82].

SO_2 was not only dissolved in water but also in toluene. The SO_2 solubility quantities in mole fraction at 293 K (20 ^oC) in water and in toluene were found to be 0.0297 (1.70 mol/L) and 0.325 (4.50 mol/L), respectively, based on the study by Makitra et al. [83]. Therefore, the Bunsen reaction appears to follow the following two-step mechanism [17]:

$$SO_2 + H_2O \rightleftharpoons H^+ + HSO_3^- \quad (3\text{-}10)$$

$$H^+ + HSO_3^- + I_2 + H_2O \rightleftharpoons H_2SO_4 + 2HI \quad (3\text{-}11)$$

SO_2 could be provided to the reaction sites either from a gas mixture or from the I_2-toluene solution where it dissolves while I_2 is transferred from the toluene phase. Reaction (3-11) occurs either at the interface of the organic phase and the aqueous phase or in the aqueous phase. When HI forms, I_2 may dissolve in the HI solution. This mechanism can be illustrated through the concentration profile of the Bunsen reaction system as shown in Figure 3.1.

3.3.1. Equilibrium between iodine and iodide species in the presence of toluene

The solubility of iodine in water is very low, however it does dissolve in hydroiodic acid significantly once HI has formed from the Bunsen reaction. The distribution of I_2 between the toluene phase and the aqueous phase was previously studied [82].

The equilibrium between I_2 and I^- species can be described mathematically when an I_2-toluene solution and water are involved, based on the following equation:

$$I_{2,\,tol} + cI^-_{,\,aqu} \leftrightarrow (I_2 \cdots cI^-)_{,\,aqu} \tag{3-12}$$

$$K_{eq} = \frac{[I_2 \cdots cI^-]_{aqu}}{[I_2]_{tol}[I^-]_{aqu}{}^c} \tag{3-13}$$

Then the distribution coefficient, D, can be defined as

$$D = \frac{[I_2 \cdots cI^-]_{aqu}}{[I_2]_{tol}} = K_{eq}[I^-]_{aqu}{}^c \tag{3-14}$$

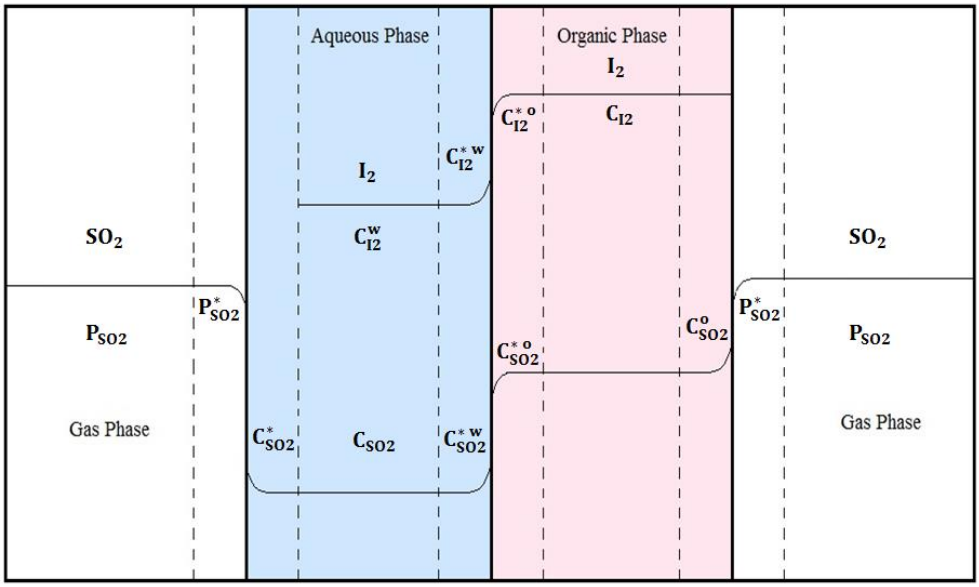

Fig 3.1. The concentration profile of the gas-liquid-liquid Bunsen reaction multiphase system [17]

Contact cells were used where the I_2-toluene solution of known concentration and the HI aqueous solution of known concentration were loaded. The two phases were separated and each I_2 concentration was analyzed after giving sufficient time for the contact between phases at room temperature. Equations (3-12) to (3-14) show the corresponding concentrations of I_2 in each phase. $I_{2,\ tol}$ and $I^-_{,\ aqu}$ are iodine in toluene and iodide anion in the aqueous solution, respectively. $(I_2 \cdots cI^-)$ is the associated species of I_2 and I^- in the aqueous phase, and K_{eq} is the equilibrium constant. The bracket ([ ]) stands for the molarity concentration of the defined species. From the analysis of data, Figure 3.2 was plotted and the values of K_{eq} and c were calculated by linear regression to be K_{eq} = 3.754 and c = 1.156. Usually, the reaction between I_2 and I^- forms I_3^-, resulting in the value of one for c. The higher value of c may suggest that part of the I^- anions, say 15.6 %, was not used in the formation of HI_3^- or, less likely, there were errors in the measurement.

The dashed line shown in Figure 3.2 is the result obtained from forcing c to be one. This may confirm the results of Spadoni et al. [38] where they found that the mixture HI–I_2–H_2O is highly dependent on the I_2:HI molar ratio and up to a 1:1 ratio, I_3^- and its corresponding ion pair, HI_3^-, are the dominant iodine compounds while at higher values, the formation of higher poly-iodine and poly-iodides compounds are certainly possible.

3.3.2. Apparent kinetics of the Bunsen reaction with iodine-toluene solution

In order to understand the kinetic characteristics of the Bunsen reaction in the multiphase system, the apparent reaction rate of the Bunsen reaction was studied in a gas-liquid-liquid multiphase system where toluene was used as the I_2 solvent.

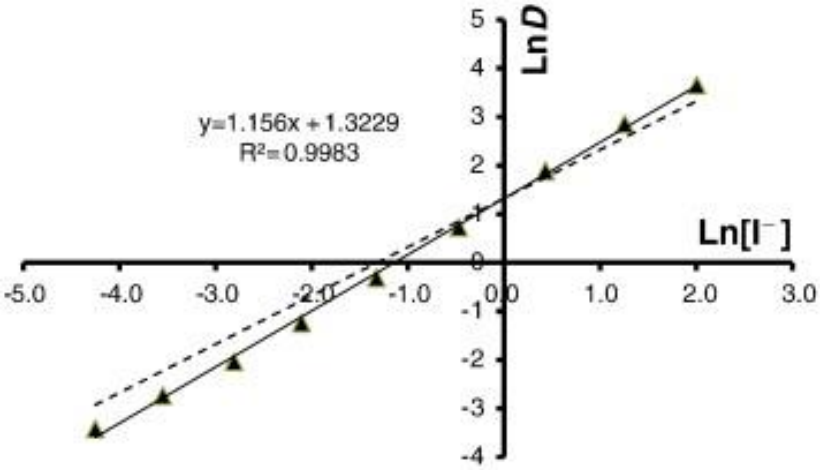

Fig 3.2. Linear correlation between the logarithm of distribution coefficient, D, and that of iodide concentration [17]

The operating conditions, such as the effects of liquid volume, toluene/water volume ratio and agitation speed on the apparent SO_2 absorption/reaction rate, were investigated in a closed system of a volume-fixed batch reactor to identify the rate-determining step [84]. For this purpose, the initial rate-analysis method was used where the reaction rate was recorded by the pressure drop of SO_2 versus time.

No significant reaction enhancement was observed on the SO_2 mass transfer from the gas phase to the liquid phase, however, increasing the agitation speed and toluene/water ratio in the liquid enhanced the reaction rate noticeably. The comparison of the rate of SO_2 absorption in the liquids of different compositions, toluene, toluene and water, or I_2-toluene solution and water, indicated that the SO_2–dissolving-in-liquid phase was the rate-controlling step, if the gas phase resistance was negligible. This was confirmed by the small value of the activation energy (6.02 kJ/mol) obtained by the fitting of the reaction rate at various temperatures using Arrhenius equation. To quantify the effect of the agitation speed and toluene/water ratio, an effective interface area between the gas phase and liquid phase (the cross-sectional area of the reactor between gas and liquid) was used to separate the specific reaction rate from the apparent rate equation. The reaction rate was found to be the first order with respect to both SO_2 and I_2.

As can be seen, to increase the reaction yield, improving the contact between reactants in the multiphase system became crucial.

3.4. HI decomposition section

Despite many advantages of using toluene, toluene merely plays the role of the organic solvent to dissolve iodine and SO_2 and the recovery of H_2SO_4 and HI which is offered by traditional solvents such as tri-n-butyl phosphate (TBP) is not observed in this multiphase system. We decided

on a direct separation of the two acids by electrolysis as shown in Figure 3.3. The electrolysis was conducted using a custom-made, dual chamber electrolysis cell and a custom-made potentiostat equipped with a Nafion 117 membrane for separating the anode chamber and the cathode chamber and Pt electrodes as both the anode and the cathode. This method is capable of decomposing the HI to H_2 at room temperature without the need of separation of excess iodine, H_2SO_4 and HI or even using any catalysts. It also can break the azeotrpic point of the mixture while reducing the demand on high quality steam. Together with the previous studies of other reactions in the H_2S splitting cycle explained earlier in this chapter, this work led to a low-temperature process of hydrogen production from the H_2S [17].

In the following section, knowledge gaps and objectives are identified on the basis of the literature review in Chapter 2 and the research studies in the batch reactor presented in this chapter.

3.5. Knowledge gaps and objectives

The introduction of toluene as the I_2 solvent has significantly improved the GA reaction stoichiometry. In other words, severe corrosion, an excess quantity of water, side reactions, and iodine vapour deposition can be avoided if the Bunsen reaction is conducted at ambient temperature. On the other hand, the existence of a new phase resulted in a multiphase reaction where the understanding of the reaction mechanism seemed to be necessary. Therefore, in this chapter, the mechanism of the multiphase Bunsen reaction was discussed in detail and the equilibrium constant between iodine and iodide was calculated in the presence of toluene. Finally, the rate-limiting step was identified to be SO_2-dissolving-in-the-liquid phase, based on the research contributed by the previous work conducted in a batch reactor to investigate the apparent kinetics of the Bunsen reaction with an iodine-toluene solution.

Fig 3.3. An electrolysis unit to produce hydrogen for direct separation of HI and sulfuric acids at room temperature

The investigation of the H_2S splitting cycle led to the creation of a low-temperature process where the conventional challenges of the S-I water-splitting cycle could be significantly minimized; however, upgrading diluted sulfuric acid is still necessary in order to increase the cycle efficiency. The required energy could possibly be provided from the heat produced from burning elemental sulfur in reaction (3-5), however the SO_2 production route in the first section (H_2S oxidation) is not limited only to elemental sulfur oxidation and could be extended to any exothermic reaction that use waste sulfur-containing materials from industry to produce SO_2. Since there are not many reports in the literature that investigate heat recovery from the various SO_2 production routes to feed the Bunsen reaction, in Chapter 5 the chemistry of the feasible routes is discussed, and their possible applications introduced. Finally, an exergy analysis was performed to identify the methods that improve the energy efficiency of these cycles.

Based on the results in this chapter, it was concluded that mass transfer efficiency becomes an important issue to increase the contacts between gas-liquid-liquid phases. Corning® Advanced-Flow ™ Reactors have proven that the gas-liquid mass transfer coefficient can be increased significantly compared to other conventional gas-liquid reactors [18]. Therefore, in Chapter 6, I explain how these glass, factory-made reactors were used to study the mass transfer behaviours of SO_2-water and SO_2-toluene as well as the absorption of the gaseous SO_2 in the whole multiphase mixture in the absence of the Bunsen reaction.

Despite many attempts to investigate the Bunsen reaction in Dr. Hui Wang's research group, it was never studied in the continuous mode. Chapter 7 presents investigation of the Bunsen reaction in the continuous mode in the presence of toluene as the solvent for iodine, where the effects of operating conditions on the SO_2 absorption and I_2 reaction rates were studied in the Corning® Advanced-Flow™ Reactors.

Finally, Chapter 8 describes a hydrogen production plant that was designed to produce 51,000 tonnes/year of hydrogen, which is the amount needed for a typical heavy oil upgrader which is followed by an economic analysis of the designed plant.

3.6. Summary

This chapter reviews the literature related to the H_2S splitting cycle and also describes the contributions that resulted in identifying the rate-limiting step of the Bunsen reaction in the multiphase system. A reaction scheme is suggested for the multiphase Bunsen reaction. It was found that the Bunsen reaction occurred soon after the I_2 contacted the water-toluene interface. SO_2 was also significantly dissolved in toluene, making the reaction mechanism more complicated. Accordingly, to increase the mixing efficiency, a conventional reactor may not be the best option.

Based on the distribution of I_2 between the toluene phase and the aqueous phase, the equilibrium constant was calculated between I_2 and I^- species. It was apparent that the formation of higher poly-iodine and poly-iodides compounds would clearly be possible at a higher I_2:HI molar ratio.

According to the apparent reaction rate study of the Bunsen reaction in the gas-liquid-liquid multiphase system, the SO_2-dissolving-in-liquid phase is the rate-controlling step, which was confirmed by the value for the fitting of the reaction rate at various temperatures by Arrhenius equation.

Finally, the knowledge gaps and objectives are identified on the basis of the literature review in Chapter 2 and the research studies in the batch reactor presented in this chapter.

CHAPTER FOUR

EXPERIMENTAL

The experiments in this thesis were conducted in two different research centres. The initial data were collected in the Low Flow Advanced-Flow Reactor (hereafter LF-AFR) at the University of Saskatchewan. Then, similar experiments were performed in the next commercially available size of Corning® Advanced-Flow™ Reactor products (G1-AFR) at the Corning Reactor Technology Center, China, where the gas and liquid analyses were performed in the Department of Biochemical Engineering, Changzhou University. This chapter describes the experimental apparatuses, introduces operating conditions and lists the chemicals used for the experiments. Following this, I present the measurement techniques, analysis methods, mass balance and the reproducibility of the data.

4.1. Experimental set-ups and operating conditions

The flow pathway of the Corning AFRs (both the LF and G1-AFRs) consists of identical heart-shaped cells with variable cross sections, which render the fluid to form a jet and repeat splitting and mixing through the pathway (divergent-convergent configuration) [85]. This mechanism helps to increase the contact area among the phases. Commercially, AFRs are designed in different sizes (LF, G1, G2, G3 and G4) based on the state of the research and requirements, from the laboratory (micro-channel) to production scale (millimeter scale). The interconnected fluidic module design allows using several modules in cascades for multiple-step reactions [86]. Each glass module is sandwiched between two fluid-heating plates, which makes temperature control possible [21]. Because different reactors were used for performing the experiments, this

section is divided into two parts to clarify the conditions under which the experiments were conducted.

4.1.1. Corning LF-AFR

Figure 4.1 shows the LF-AFR (the smallest model of the Corning reactor products, also called microchannel AFR) modules and their connections used in this study at the University of Saskatchewan. The heart-shaped cells and flow pathway can also be seen. The internal volume of each fluidic module of the LF-AFR is about 0.4 mL, which allows for liquid flow rates in the range of 0–10 mL/min. Fluidic modules might be used in parallel or series based on the research requirements. Five modules were used: Module 1 had two fluid inlet ports (A1 and A2), allowing two fluids to mix and/or react. Module 2 had one inlet port (A3), allowing a third fluid to be preheated. All the fluids met at the third module, mixing and reacting, which continued in modules 4 and 5 in order to extend the residence time. For a typical run, a gas mixture of SO_2 and N_2, supplied from cylinders and controlled by two mass flow controllers (1179A Mass-Flo®, MKS), was fed to port A2. Water and toluene (with or without I_2) were also pumped into the reactor via ports A1 and A3 or A3 and A1, respectively, using 100-Legato KD scientific syringe pumps.

The experiments were carried out at the temperature in the ambient range (22-70 ^oC), at different gas flow rates ranging from 22 to 85.7 mL/min at standard temperature and pressure (STP), and at different liquid flow rates from 0.3 to 4.5 ml/min. The outlet of the reactor was open to the atmospheric pressure. A manual control valve was designed to keep the level of the liquid constant at the lower-middle of the separator so that the outlet gas could be easily purged only from the top of the separator. At the bottom of the separator, liquid was collected where the organic phase was sampled with a glass pasture pipet. The water phase was sampled from the bottom of the separatory funnel without any dilution.

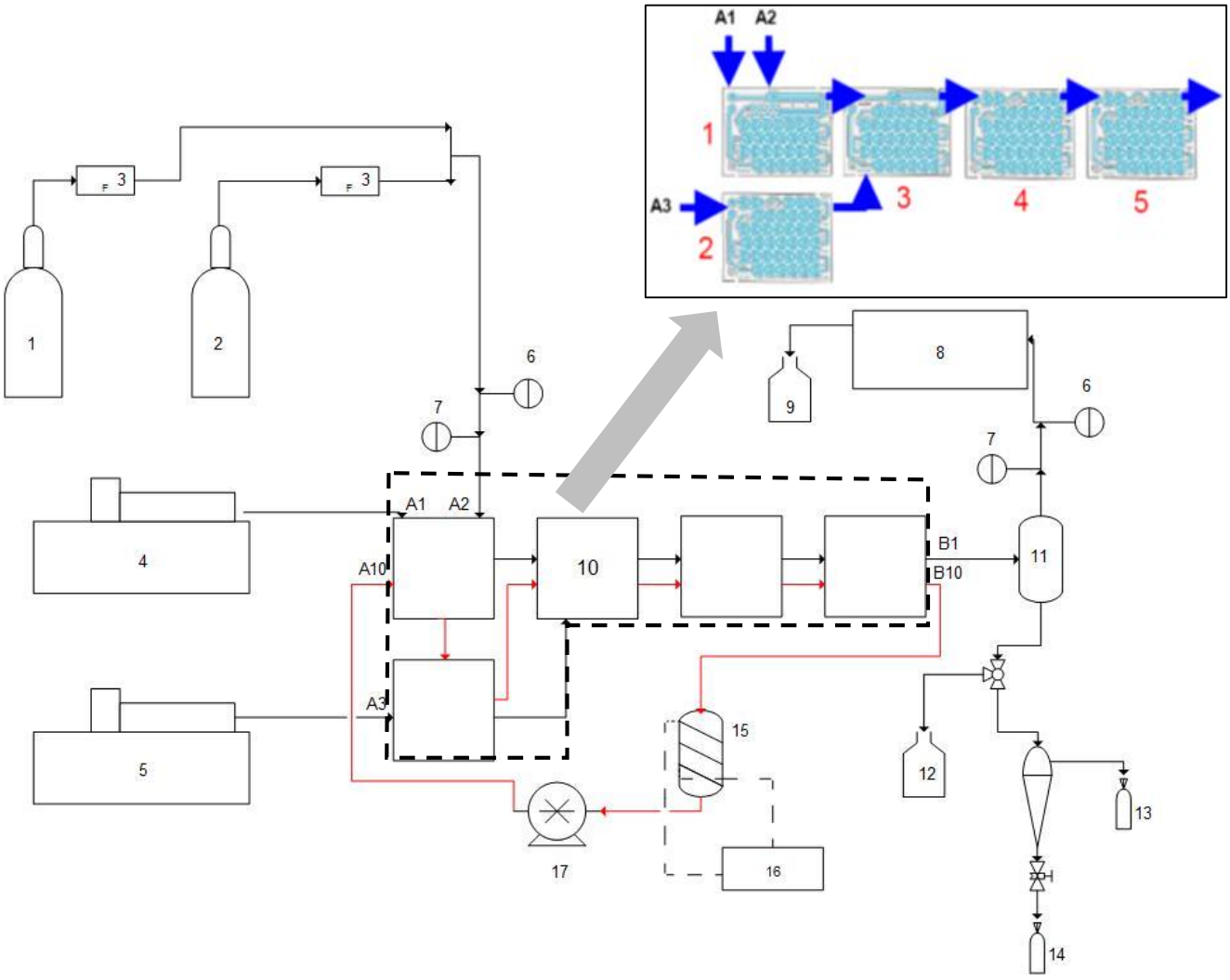

Fig 4.1. Schematic diagram of experimental set-up for the Bunsen reaction using the LF-AFR: (1) N_2 tank; (2) SO_2 tank; (3) Mass flow controller; (4) Organic syringe pump; (5) Water syringe pump; (6) Pressure indicator; (7) Temperature indicator; (8) Gas Chromatograph; (9) Scrubber; (10) Corning® Advanced-Flow™ Reactor; (11) Gas-liquid separator; (12) Waste tank; (13) Organic phase sampling vial (14) Water phase sampling vial; (15) water (oil) bath (16) Temperature controller; (17) Hot fluid pump

As soon as the steady state (at least the equivalent of three times the internal volume of the reactor should be processed) was reached, sampling of gas and liquid could be started. The outlet stream of the reactor (module 5) was conducted to a small glass T-shaped gas-liquid separator where the gas stream was separated from the liquid. The gas exited from the top to be analyzed by an online GC, while the liquid was collected from the bottom. The fluid properties of the Gas-Liquid-Liquid phases are shown in Table 4.1.

4.1.2. Corning G1-AFR

The second set of experiments was conducted in a G1-AFR at the Corning Reactor Technology Center, China. The internal volume of each fluidic module of the G1-AFR is about 20 times larger than those in the LF-AFR: 8 mL with a maximum allowable flow rate of 200 mL/min for the liquids. The rest of the conditions, such as material, geometry, and design conditions, remained the same. For this study only two fluidic modules (modules 1 and 3) were used, one for mixing SO_2-N_2 and the organic phase and the other one for the reaction where water was directly mixed with the mixture of SO_2-N_2 and the organic phase coming from module 1. Similar to the previous runs in the LF-AFR, the gas mixture of SO_2 and N_2, from cylinders controlled by two mass flow controllers (5850S smart mass flow, Brooks Instruments Inc.), was fed to port A2. Toluene (with or without I_2) and water were also pumped into the reactor via ports A1 and A3 (the fluidic module 2 was not used), respectively, using a PTFE Fuji Technic Tokyo pump for the organic phase and a Stainless Steel Jiangsu Hanbon Science & Technology Co. pump for water. The experiments were carried out at the temperature in the ambient range (22-80 ^{o}C), at different gas flow rates ranging from 600 to 2000 mL/min at standard temperature and pressure (STP), and at different liquid flow rates from 30 to 90 ml/min. The outlet of the reactor was also open to the atmospheric pressure. The set-up design of the G1-AFR was exactly the same as the LF-AFR

Table 4.1. Fluid properties of water, toluene and sulfur dioxide at 20 ºC and atmospheric pressure [87]

fluid	density (kg/m^3)	viscosity (Pa.s)	surface tension (N/m)
water	998.2	1.0×10^{-3}	0.072
toluene	866.89	0.59×10^{-3}	0.028
sulfur dioxide	2.71	1.25×10^{-5}	---

except for the gas phase, which was analyzed offline using Cole-Parmer Tedlar bags at the specific time intervals. Two 10-liter bottles of concentrated sodium hydroxide (5 mol/lit) were used in series to capture non-reacted SO_2 at the reactor outlet. The calibration curves for the mass flow controllers and the pumps in two series of experiments are presented in Appendix A.

4.2. Chemicals

The chemicals used for the experiments in the LF-AFR were mostly ACS grade as received: iodine (99.8%, Acros Organics), sulfur dioxide (99.98%, Praxair), nitrogen (99.99 %, Praxair), sodium hydroxide (97 %, EMD), sodium thiosulfate anhydrous (99.5%, Fisher), sodium iodide (99.999 %, Acros Organics), toluene (99.95 %, BDH), sulfuric acid (96 wt%, Fisher) and phenolphthalein and thyodene as the indicators.

The chemicals used for the experiments in the G1-AFR were also ACS grade as received: iodine (99.8%, Shanghai Shenbo), sulfur dioxide (99.99%, Shanghai Weichuang Gas), nitrogen (99.999%, Changzhou Wujin Huayang Gas), sodium hydroxide (96%, Sinopharm Chemical Reagent), sodium thiosulfate anhydrous (99%, Shanghai Lingfeng Chemical Reagent), potassium iodide (98.5%, Shanghai Shenbo Chemical), toluene (99.5%, Sinopharm Chemical Reagent), and phenolphthalein and thyodene as the indicators. All the solutions used in both series of experiments and analyses were prepared by diluting the corresponding chemicals with deionized water.

4.3. Measurement techniques and analysis methods

4.3.1. Liquid phase analyses

The concentrations of iodine in toluene and iodide in water were measured for the runs in the LF-AFR by a Shimadzu UV mini 1240 UV-Vis spectrophotometer while the corresponding measurements for the runs in the G1-AFR were carried out at Changzhou University using a Gold

Spestrumlab 53 UV-Vis spectrophotometer of Shanghai Lengguang Technology with Mandel 10 mm path length quartz cuvettes. The proton concentration in the water phase was determined by titration with a standard sodium hydroxide solution using phenolphthalein as the indicator. The iodine concentration in the water phase was determined by titration with a standard sodium thiosulfate using thyodene as the indicator. The calibration curves for the liquid phase analyses are presented in Appendix B.

4.3.2. Gas phase analyses

Non-reacted SO_2 was analyzed using a Varian CP-3800 gas chromatograph equipped with TCD conducted in the LF-AFR. The internal normalization method was used for the gas calibration in the LF-AFR because this technique corrects for the sample-size error when the sample size is variable [88]. Since the volume of gas after either reaction or absorption is drastically decreased in the system, therefore, the amount of sample injected into the GC sample loop would become different each time at the outlet compared to the reactor inlet and the external calibration method might not have given accurate results. However, for the experiments conducted in the G1-AFR, the external calibration method was used. Due to unavailability of the online method, gaseous sulfur dioxide samples were stored in Cole-Parmer Tedlar bags and then were analyzed by a Taizhou Zhonghuan Analysis Instrument Co. RPP-2000S Fluorescence Sulfur instrument at Changzhou University. The details of the measurement procedure for GC analysis and calibration curves for the experiments are described in Appendix C.

The consumption rate of sulfur dioxide was determined by the difference in the two flow rates, in and out of the reactor, measured with the mass flow controller and gas chromatograph, respectively. As a result of the measurement, the total amount of sulfur dioxide consumed per unit of volume of the reactor and time is considered as the absorption rate.

4.4. Mass balance

4.4.1. Water-SO_2 mixture

The runs with constant mole fractions of gas (y_{SO_2}=0.50) and gas flow rates (30 mL/min at STP) were conducted repeatedly at a constant water flow rate (0.5 mL/min) in the LF-AFR at room temperature in order to check the mass balance of the sulfur dioxide. For each run, 10 mL of water was collected for the titration with a 0.3 M sodium hydroxide standard solution while gas samples were analyzed by GC, based on the procedure mentioned in the previous section. The results presented in Table 4.2 indicate that the sulfur dioxide balance was laid below 5%.

Similar runs were conducted with constant mole fractions of gas (y_{SO_2}=0.50) and gas flow rates (900 mL/min at STP) at constant water flow rates (30 mL/min) in the G1-AFR at room temperature with the same analysis procedure as mentioned above. However, the gas phase was analyzed differently according to the Section 4.3.2. The results presented in Table 4.3 show that the sulfur dioxide balance was laid below 5% in the G1-AFR similar to the results observed for the LF-AFR.

4.4.2. Toluene-SO_2 mixture

The runs with constant mole fractions of gas (y_{SO_2}=0.50) and gas flow rates (30 mL/min at STP) were conducted at constant toluene flow rates (1.75 mL/min) in the LF-AFR at room temperature. For each run, 10 mL of toluene was collected and then mixed with 50 mL of a 0.3 M sodium hydroxide standard solution.

Table 4.2. Results for SO_2 balance in the LF-AFR for SO_2-water mixture (water flow rate=0.5 mL/min, gas flow rate=30 mL/min, SO_2 mole fraction=0.5, T=22 ^oC)

No.	inlet SO_2 (mmol/min)	outlet SO_2 in water (mmol/min)	outlet SO_2 in gas phase (mmol/min)	(in-out)/in*100
1	0.67	0.19	0.48	0
2	0.67	0.19	0.48	0
3	0.67	0.20	0.48	1.5

Table 4.3. Results for SO_2 balance in the G1-AFR for SO_2-water mixture (water flow rate=30 mL/min, gas flow rate=900 mL/min, SO_2 mole fraction=0.5, T=22 ^oC)

No.	inlet SO_2 (mmol/min)	outlet SO_2 in water (mmol/min)	outlet SO_2 in gas phase (mmol/min)	(in-out)/in*100
1	40.2	18.5	20.5	3.0
2	40.2	18.8	20.1	3.2
3	40.2	19.4	20.1	1.7

The resulting solution was titrated with a 0.1 M hydrochloric acid standard solution and the amount of consumed NaOH determined the amount of absorbed SO_2 in toluene while SO_2 concentration was measured by GC in the gas phase. The results presented in Table 4.4 indicate that the sulfur dioxide balance was equal to or below 5%.

The similar runs with constant mole fractions of gas (y_{SO_2}=0.50) and gas flow rates (800 mL/min at STP) were conducted at a constant toluene flow rate (40 mL/min) in the G1-AFR at room temperature. The analysis procedure for toluene is the same as above while the gas phase analysis was conducted according to the Section 4.3.2. The results presented in Table 4.5 indicate that the sulfur dioxide balance was below 5%.

4.5. Reproducibility of data

It is necessary to test the reliability of the experiments' measurements by reproducibility of the data. In this thesis, each experiment was repeated three times and the standard error of the mean was measured, as illustrated in Chapters 6 and 7.

Table 4.4. Results for SO_2 balance in the LF-AFR for SO_2-toluene mixture (toluene flow rate=1.75 mL/min, gas flow rate=30 mL/min, SO_2 mole fraction=0.5, T=22 ^oC)

No.	inlet SO_2 (mmol/min)	outlet SO_2 in toluene (mmol/min)	outlet SO_2 in gas phase (mmol/min)	(in-out)/in*100
1	0.67	0.12	0.52	5.0
2	0.67	0.15	0.50	3.0
3	0.67	0.16	0.50	1.5

Table 4.5. Results for SO_2 balance in the G1-AFR for SO_2-toluene mixture (toluene flow rate=40 mL/min, gas flow rate=800 mL/min, SO_2 mole fraction=0.5, T=22 ºC)

No.	inlet SO_2 (mmol/min)	outlet SO_2 in toluene (mmol/min)	outlet SO_2 in gas phase (mmol/min)	(in-out)/in*100
1	17.85	5.0	12.6	1.4
2	17.85	4.5	12.9	2.5
3	17.85	4.4	12.7	3.0

4.6. Summary

In this chapter the experimental set-ups are illustrated, the operating conditions and the chemicals used for the experiments are detailed and the measurement techniques and analysis methods are presented. The initial sets of data were collected in the LF-AFR at the University of Saskatchewan and then similar experiments were performed at a higher scale using a G1-AFR at the Corning Reactor Technology Center, China. The gas and liquid analyses were performed in the Department of Biochemical Engineering, Changzhou University. Finally, the mass balance and reproducibility of data are explained.

CHAPTER FIVE

EXERGY ANALYSIS OF HYDROGEN PRODUCTION FROM DIFFERENT SULFUR-CONTAINING COMPOUNDS BASED ON THE H_2S SPLITTING CYCLE

Based on the S-I water-splitting cycle, the H_2S splitting cycle, consisting of three reactions, was developed in Dr. Hui Wang's research group. This cycle splits 1 mole of H_2S into 1 mole of hydrogen gas and 1 mole of elemental sulfur while sulfuric acid and iodine are being cycled within the system. During the work, it was realized that hydrogen could also be produced from different sulfur-containing feedstocks as long as it could be converted into SO_2 to feed the Bunsen reaction. SO_2 could also come from the SO_2 emission control unit when reversible physical absorption is used. Therefore, various chemical reaction routes could be developed to produce hydrogen, making use of sulfur-containing compounds, which exist in different industry sectors as byproducts or waste products. In this chapter, I propose the chemistry of the routes, discuss their possible applications, and use exergy analysis to study the possible ways to improve the energy efficiency of every SO_2 production route. The contents of this chapter was published in the *International Journal of Hydrogen Energy* as described in Chapter 1, to which my contributions were performing the exergy analysis and calculations under the supervision of Dr. Hui Wang and drafting the paper and its revisions. Pascal Mertins was involved in the preliminary exergy calculations. Dr. Wang proposed the open-loop cycles, suggested performing an exergy analysis on them and participated in paper preparation, revision and submission.

5.1. H_2 production routes from various sulfur-containing feedstocks

Route 1 is the basic H_2S splitting cycle that contains three chemical reactions, shown as follows [14]:

$$H_2S(g) + H_2SO_4(l) \rightarrow SO_2(g) + S(s) + 2H_2O(l) \quad (5\text{-}1)$$

$$SO_2(g) + I_2(l) + 2H_2O(l) \rightarrow H_2SO_4(l) + 2HI(l) \quad (5\text{-}2)$$

$$2HI(l) \rightarrow H_2(g) + I_2(l) \quad (5\text{-}3)$$

The overall reaction is:

$$H_2S(g) \rightarrow H_2(g) + S(s) \quad (5\text{-}4)$$

The H_2S splitting cycle can be performed in different stoichiometry if the elemental sulfur from reaction (5-1) is further oxidized into SO_2. The new cycle consists of four reactions, (Route 2) [14]:

$$0.5H_2S(g) + 0.5H_2SO_4(l) \rightarrow 0.5SO_2(g) + 0.5S(s) + H_2O(l) \quad (5\text{-}5)$$

$$0.5S(s) + 0.5O_2(g) \rightarrow 0.5SO_2(g) \quad (5\text{-}6)$$

$$SO_2(g) + I_2(l) + 2H_2O(l) \rightarrow H_2SO_4(l) + 2HI(l) \quad (5\text{-}2)$$

$$2HI(l) \rightarrow H_2(g) + I_2(l) \quad (5\text{-}3)$$

The overall reaction is:

$$0.5H_2S(g) + H_2O(l) + 0.5O_2(g) \rightarrow H_2(g) + 0.5H_2SO_4(l) \quad (5\text{-}7)$$

In comparison to Route 1, Route 2 produces more H_2 from 1 mole of H_2S. Intentionally, these two routes were developed to provide H_2 for hydrotreating processes in the petroleum

industry, especially in oil sands bitumen upgrading, from their waste product H_2S. If successful, self-supporting hydrogen production could be developed and reliance on natural gas as a feedstock could be eased [14].

Route 3 is for situations where H_2S can be directly burnt into SO_2 through an intensively exothermic reaction.

$$H_2S(g) + 1.5O_2(g) \rightarrow SO_2(g) + H_2O(g) \quad (5\text{-}8)$$

$$SO_2(g) + I_2(l) + 2H_2O(l) \rightarrow H_2SO_4(l) + 2HI(l) \quad (5\text{-}2)$$

$$2HI(l) \rightarrow H_2(g) + I_2(l) \quad (5\text{-}3)$$

The overall reaction is:

$$H_2S(g) + H_2O(l) + 1.5O_2(g) \rightarrow H_2(g) + H_2SO_4(l) \quad (5\text{-}9)$$

Reaction (5-8) is not new. It is one of the reactions in the Claus Process where H_2S is converted to elemental sulfur. The reaction heat is so intensive that the associated temperature rise can only be controlled by removing sequential heat in a multistage process [89]. The application of this route is suitable for the natural gas industry where H_2S is removed by absorption methods such as amine solution absorption. Both clean natural gas and hydrogen could be provided from the gas plants. In fact, as the sulfur market has been saturated (especially in Canada), recovering hydrogen from H_2S appears to be worthier than recovering sulfur. Engineers designing to-be-built gas plants could consider adopting this process.

Route 4 produces hydrogen from elemental sulfur:

$$S(s) + O_2(g) \rightarrow SO_2(g) \quad (5\text{-}10)$$

$$SO_2(g) + I_2(l) + 2H_2O(l) \rightarrow H_2SO_4(l) + 2HI(l) \quad (5\text{-}2)$$

$$2HI(l) \rightarrow H_2(g) + I_2(l) \quad (5\text{-}3)$$

The overall reaction is:

$$S(s) + 2H_2O(l) + O_2(g) \rightarrow H_2(g) + H_2SO_4(l) \quad (5\text{-}11)$$

The sulfur oxidation, reaction (5-10), must take place in a sulfur burner, and should be performed at temperatures above the melting point of elemental sulfur (392 K) to keep the sulfur in its molten state. Since the auto-ignition temperature of sulfur in the air at moderate pressures is 533 K, the furnace where the oxidation takes place must be above this temperature. Once sulfur is injected into the burner, which is preheated to 600–628 K, it is oxidized into SO_2 with air and the temperature of the exiting gas mixture (10–12 vol % SO_2 plus air) from the burner can reach as high as 1250–1400 K [90]. The application of this route is suitable for situations where a Claus sulfur recovery plant is in place and H_2 is in need. More generally, the abundance of elemental sulfur in Canada could be a further feedstock to produce H_2 [91].

SO_2 captured from stack gas could be fed into the cycle for H_2 production as well. This gives rise to Route 5. This option suits power plants where sulfur-containing fossil fuels are burned and SO_2 is emitted in the stack gas.

$$SO_2(g) + I_2(l) + 2H_2O(l) \rightarrow H_2SO_4(l) + 2HI(l) \quad (5\text{-}2)$$

$$2HI(l) \rightarrow H_2(g) + I_2(l) \quad (5\text{-}3)$$

The overall reaction is:

$$SO_2(s) + 2H_2O(l) \rightarrow H_2(g) + H_2SO_4(l) \quad (5\text{-}12)$$

Sulfur dioxide is one of the most harmful air pollutants. For example, burning a 3.5% sulfur content coal results in a SO_2 concentration in the stack gas of about 0.2–0.25% by volume (2000–2500 ppm) [92]. To restrict the emission of sulfur oxides into the atmosphere, different processes have been suggested and extensively investigated, which include the amine absorption process, a conventional flue gas desulfurization process and a neutralization process by utilizing sodium hydroxide or sodium carbonate [93], [94] and [95]. However, the scrubbing of the stack gas with aqueous ammonia solutions is presently the most promising process as it is one of the simplest and most economical ways of getting the sulfur oxides out of the stack gas. Ammonia in the scrubber liquor can react with the SO_2 dissolved in the liquid phase to produce ammonium sulfite and ammonium bisulfite. To recycle ammonia, the liquid effluent from the scrubber is subjected to a decomposition or stripping operation separating sulfur dioxide from the stream of ammonia [96].

5.2. Exergy analysis for SO_2 production in every route

Exergy is defined as the maximum theoretical work possible during the process when a system passes from a given state to the dead state. The dead state means a system that is in thermal and mechanical equilibrium with its environment in which the value of exergy is zero [97]. By converting the pressure and temperature of a system to those of the environment,

thermomechanical or physical exergy is calculated, which is the maximum amount of work the system can possibly do during the converting process. However, when its physical exergy is zero, a system may still be out of equilibrium with its environment in some other respects. The reason can be attributed to the nature of the components making up the system and the environment. The difference leads to values for the chemical exergy. The sum of the thermomechanical exergy and chemical exergy is called the total exergy [98].

Exergy analysis is usually applied to an existing process to discover those aspects where improvements could effectively enhance the overall energy efficiency of the process [99]. In this chapter, exergy analysis is performed to assess the chemical reactions of the five routes of hydrogen production through the open-loop H_2S splitting cycle from varieties of sulfur-containing feedstock. From the exergy analysis, one can tell the potential energy that the processes of a route can destroy. In other words, when the to-be-destroyed energy can be recovered and reused, the energy efficiency can be improved.

The difference among the five routes of hydrogen production from different sulfur-containing compounds is how the SO_2 is provided to the Bunsen reaction in the cycle. Therefore, in this chapter, the terminology, *SO_2 production route,* is also used to refer to the various hydrogen production routes. The exergy analysis is only performed for the SO_2 production section, according to the chemical reactions of SO_2 production in the five routes.

This analysis consists of three steps. The first step calculates the amount of destructed exergy to bring the reactants to the reaction conditions. The second step evaluates the exergy change associated with the chemical reaction. And the third step investigates the destructed exergy while the product stream is brought to the Bunsen reaction conditions. Obviously, step 1 and step 3 are considered as physical processes while step 2 is treated as a chemical one. During this

analysis, the reference environment is defined as the air at 298 K (25 °C) of temperature and 101.3 kPa (1 atm) of pressure. At this condition, the air consists of N_2 = 75.67%, O_2 = 20.35%, H_2O (g) = 3.12%, CO_2 = 0.03% and other gases = 0.83% [100]. For all the chemical reactions, reactants and products are assumed to be at the reaction temperature and the pressure of 1 atm, and all the processes are assumed to occur at steady state as well. Moreover, all the processes are assumed to continue to completion. This analysis uses the base of 1 mole of hydrogen produced per cycle. Therefore, all the other quantities are determined in terms of the stoichiometry of a chemical reaction or the composition of the mixture in consideration. For a steady state reaction process, the amount of reaction heat is defined as

$$Q = H_P - H_R = \sum (n_P (\bar{h}_f^o + \bar{h} - \bar{h}_o))_P - \sum (n_R (\bar{h}_f^o + \bar{h} - \bar{h}_o))_R \quad (5\text{-}13)$$

where n is the moles of reactants and products, and enthalpy of formation is denoted with $\bar{h}_f^o$. The enthalpy of formation is the energy released or absorbed when the compound is formed from its elements, the compound and elements all being at T_o and P_o. The molar enthalpy of a compound at a state other than the standard state is found by adding the molar enthalpy change between the standard state and the state of interest to the enthalpy of formation. Also, the exergy balance for a process involving chemical reactions can be written as

$$\sum ex_{in} - \sum ex_{out} - ex_{destructed} = \Delta ex_{system} \quad (5\text{-}14)$$

The exergy associated with a process with a flow at a specified state is the sum of thermomechanical and chemical exergies, which is given as follows:

$$\overline{ex} = \overline{ex}^{phys} + \overline{ex}^{ch} = (\bar{h} - \bar{h}_o) - T_o(\bar{S} - \bar{S}_o) + \frac{V^2}{2} + gz + \overline{ex}^{ch} \quad (5\text{-}15)$$

For a steady-state system where Δex_{system} is zero, combining equations (5-14) and (5-15) yields

$$\begin{aligned}\overline{ex}_{destruction} = &\sum \left[(\bar{h} - \bar{h}_o) - T_o(\bar{S} - \bar{S}_o) + \frac{V^2}{2} + gz + \overline{ex}^{ch} \right]_{in} \\ &- \sum \left[(\bar{h} - \bar{h}_o) - T_o(\bar{S} - \bar{S}_o) + \frac{V^2}{2} + gz + \overline{ex}^{ch} \right]_{out} + (1 - \frac{T_o}{T_F})Q\end{aligned} \quad (5\text{-}16)$$

where Q is the heat that interacts with the system (negative for exothermic reactions). It is rational to assume the molar kinetic exergy ($V^2/2$) and molar potential exergy (gz) of substances are equal to zero. Then,

$$\begin{aligned}\overline{ex}_{destruction} = &\sum \left[(\bar{h} - \bar{h}_o) - T_o(\bar{S} - \bar{S}_o) + \overline{ex}^{ch} \right]_{in} - \sum \left[(\bar{h} - \bar{h}_o) - T_o(\bar{S} - \bar{S}_o) + \overline{ex}^{ch} \right]_{out} \\ &+ (1 - \frac{T_o}{T_F})Q\end{aligned} \quad (5\text{-}17)$$

The enthalpy and entropy of formation and standard chemical exergy values of elements and compounds involved in this study are presented in Tables 5.1 and 5.2, respectively. In general, the standard chemical exergy of a component j is calculated from the standard chemical exergy of its elements [98] by using the following equation:

Table 5.1. Enthalpy and entropy of formation, and standard chemical exergy of elements [101, 102]

component	$\bar{h}_f^0$ (kJ/kmol)	$\bar{S}_f^0$ (kJ/kmol.K)	$\overline{ex}^{ch}$ (kJ/kmol)
H_2 (g)	0	130.57	236090
O_2 (g)	0	205.03	3970
S (s)	0	32.054	609600
N_2 (g)	0	191.61	720

Table 5.2. Enthalpy and entropy of formation, and standard chemical exergy of compounds [101, 102]

component	$\bar{h}_f^o$ (kJ/kmol)	$\bar{S}_f^o$ (kJ/kmol.K)	$\overline{ex}^{ch}$ (kJ/kmol)
H_2S (g)	-20500	205.77	812000
H_2SO_4 (l)	-813989	156.9	161020
H_2O (g)	-241830	188.84	9500
H_2O (l)	-285830	69.95	900

$$\overline{ex}_j^{ch} = \Delta_f g^o_{j,298.15} + \sum n_i \overline{ex}_i^{ch} \quad (5\text{-}18)$$

Applying Shomate equations [101], enthalpy and entropy values of each compound are evaluated for each step. These equations are presented as follows:

$$\bar{h} - \bar{h}_0 = A*T + B*T^2/2 + C*T^3/3 + D*T^4/4 - E/T + F - H \quad (5\text{-}19)$$

$$\bar{S} = A*\ln(T) + B*T + C*T^2/2 + D*T^3/3 - E/(2*T^2) + G \quad (5\text{-}20)$$

where T is 1/1000 of the specified temperature (in K) of the compound and A, B, C, D, E, F, G and H are Shomate constants.

At steady state, the rate at which exergy enters the system should be equal to the rate at which exergy exits plus the rate at which exergy is destroyed within the system. Consequently, the exergetic efficiency, or exergy efficiency, considering a steady-state steady-flow process, can be defined using the following equation [103]:

$$\eta_{ex} = \frac{\overline{ex}_{out}}{\overline{ex}_{in}} = 1 - \frac{\overline{ex}_{destroyed}}{\overline{ex}_{in}} \quad (5\text{-}21)$$

where $\overline{ex}_{in}$ is the molar exergy that enters plus heat, and $\overline{ex}_{out}$ is the molar exergy that exits the system plus heat. Considering the above procedure and assuming no work was involved in all processes, exergy analyses were conducted for all the SO_2 production routes on the basis of one mole of hydrogen. The operating conditions of the reactions used for the exergy analyses were found from reference papers, which are depicted in Table 5.3.

Table 5.3. Operating conditions of the reactions involved in exergy analysis

reaction	temperature [K]	pressure [kPa]	reference
(5-1), (5-5)	393.15	101.3	[14]
(5-6), (5-10)	1300	150	[90]
(5-8)	1573	101.3	[89]
(5-2)	393.15	101.3	[6]
(5-3)	723.15	101.3	[6]

5.3. Sample calculation using route 3

Route 3, the H_2S oxidation by O_2, was used to illustrate the calculation procedure. As discussed, there were three steps involved to convert the reactants, H_2S and O_2, from the initial state, 298 K (25 °C) and 101.3 kPa (1 atm), to the products, SO_2 and H_2O, at the Bunsen reaction conditions, 298 K (25 °C) and 101.3 kPa (1 atm), as shown in Fig 5.1.

The first step was to bring the reactants of H_2S oxidation to the reaction temperature, which is considered as a physical step. An energy balance for this step is written as follows:

$$n_1 \bar{h}_1 + n_2 \bar{h}_2 + Q_{in} = n_3 \bar{h}_3 + n_4 \bar{h}_4 \tag{5-22}$$

An exergy balance can be written as

$$\overline{ex}_{destruction} = [n_1 \bar{ex}_1 + n_2 \bar{ex}_2 + (1 - \frac{T_0}{1573}) Q_{in}] - [n_3 \bar{ex}_3 + n_4 \bar{ex}_4] \tag{5-23}$$

Chemical reaction occurred at step 2 in which hot stream materials underwent a strong exothermic reaction. The energy balance associated with this step is

$$\begin{aligned} Q_{reaction} &= H_P - H_R = n_5(\bar{h}^o_{f5} + \bar{h}_5 - \bar{h}^o_5) + n_6(\bar{h}^o_{f6} + \bar{h}_6 - \bar{h}^o_6) \\ &- n_3(\bar{h}^o_{f3} + \bar{h}_3 - \bar{h}^o_3) - n_4(\bar{h}^o_{f4} + \bar{h}_4 - \bar{h}^o_4) \end{aligned} \tag{5-24}$$

And, the destructed exergy of this step is calculated as follows:

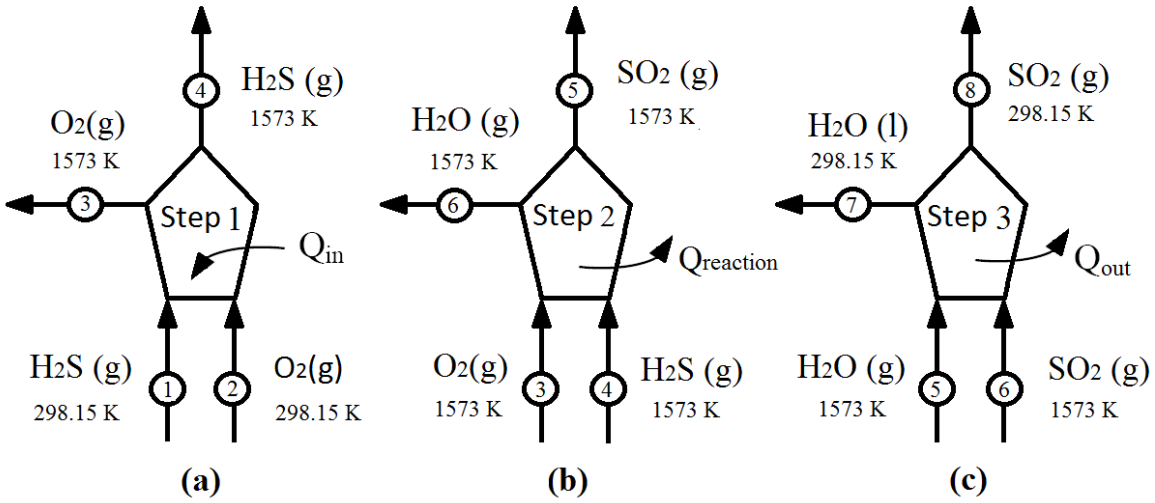

Fig 5.1. A schematic of material and heat streams in the steps of H_2S oxidation route (route 3). (a) Bringing reactants to the reaction temperature and pressure; (b) Reaction step at the given temperature and pressure; and (c) Bringing products to the Bunsen reaction temperature and pressure

$$\overline{ex}_{destruction} = \left[(\bar{h} - \bar{h}_o) - T_o(\bar{S} - \bar{S}_o) + + \overline{ex}^{ch}\right]_3 + \left[(\bar{h} - \bar{h}_o) - T_o(\bar{S} - \bar{S}_o) + \overline{ex}^{ch}\right]_4$$
$$- \left[(\bar{h} - \bar{h}_o) - T_o(\bar{S} - \bar{S}_o) + \overline{ex}^{ch}\right]_5 - \left[(\bar{h} - \bar{h}_o) - T_o(\bar{S} - \bar{S}_o) + \overline{ex}^{ch}\right]_6 + (1 - \frac{T_o}{1573})Q_{reaction} \quad (5\text{-}25)$$

The energy balance and destructed exergy of H_2O and SO_2 cooling down, the 3rd step in the route, are given as

$$n_5 \bar{h}_5 + n_6 \bar{h}_6 = Q_{out} + n_7 \bar{h}_7 + n_8 \bar{h}_8 \quad (5\text{-}26)$$

$$\overline{ex}_{destruction} = [n_5 \bar{ex}_5 + n_6 \bar{ex}_6] - [n_7 \bar{ex}_7 + n_8 \bar{ex}_8] + (1 - \frac{T_0}{298.15})Q_{out} \quad (5\text{-}27)$$

Exergy values of all the streams in this route were calculated using equations (5-22–5-27). The results are presented in Table 5.4. The results suggest that the main contribution to the destructed exergy comes from steps 2 and 3.

5.4. Destructed exergy for different SO_2 production routes

Following the calculation procedure shown in the previous section, the exergy destructed during SO_2 production is calculated and the results are summarized in Table 5.5. The irreversibility is defined as exergy destroyed or wasted work potential resulting from friction, mixing, chemical reactions, heat transfer, unrestrained expansion, non-quasi-equilibrium compression, and/or expansion, which always generates entropy; and anything that generates entropy always destroys exergy. In other words, the irreversibility represents the energy that could have been converted into work but was wasted instead. Although the exergy change of a system can be positive or negative during a process, exergy destroyed cannot be negative for irreversible processes. It also

Table 5.4. Exergy values of various streams associated with route 3 shown in Fig 5.1

stream No.	exergy values (kJ/mol H_2)		
	Step 1	Step 2	Step 3
1	812.00	----	----
2	5.96	----	----
3	46.42	46.42	----
4	847.61	847.61	----
5	----	355.25	355.25
6	----	42.02	42.02
7	----	----	0.90
8	----	----	313.40
Exergy transfer by heat (kJ/mol H_2)	98.14	-422.31	0
Destructed Exergy (kJ/mol H_2)	22.07	74.45	82.98

Table 5.5. Exergy destruction for different SO_2 production routes

route No.	destructed Exergy (kJ/mol H_2)			
	Step 1	Step 2 (reaction step)	Step 3	total
1	1.87	40.45	3.18	45.50
2	0.93	56.21	16.00	73.14
3	22.07	74.45	82.98	179.49
4	13.01	66.76	29.57	109.34
5				-

equals zero for a totally reversible process and when a process is impossible it takes negative values [104]. According to the above discussion, for an efficient system, the exergy output should be maximized in order to reach as close as possible to a reversible process.

Basically, the first route, SO_2 production from the reaction between H_2S and sulfuric acid, has the lowest value of destructed exergy. This indicates that the amount of lost work is quite small and the majority of the input energy can be converted to useful work. On the other hand, the potential for energy recovery is relatively low, compared to other routes. To meet the requirements for hydrogen in the hydrotreating plants, the second route is the sole choice because it produces 2 mole H_2 from 1 mole H_2S. The exergy destructed in this route is larger than route 1 due to reaction (5-6), which is an exothermic reaction.

It is obvious that SO_2 production from direct oxidation of H_2S (route 3) has the most amount of exergy destructed. It means that there would be more potential to recover the energy carried by the high-temperature material streams in this route to produce electricity, high quality steam, or to meet the energy need for other reactions in the cycle. Similarly, a considerable amount of energy may be recovered from route 4 when SO_2 is produced from elemental sulfur oxidation because of the highly exothermic nature of the reaction. Table 5.6 shows the heat values related to every step and the sum of different routes. A positive sign means heat is needed and a negative sign means heat is given off. The overall heat associated with every route is negative. An example of one of the possible uses of recovered heat to improve the overall energy efficiency of a route is found in routes 3 and 4. Here, the heat recovered is sufficient to support the endothermic reaction, HI decomposition, where the heat needed is 200 kJ/mol H_2.

To keep an operation economical, air is applied as the source of oxygen in most industrial applications. Figure 5.2 compares the difference of exergy destructed between using oxygen and

Table 5.6. Total heat associated with SO_2 production in different routes

route no.	released or absorbed heat (kJ/mol H_2)			
	Step 1	Step 2	step 3	Total
1	17.34	-28.62	-20.89	-32.16
2	8.67	-156.07	-34.70	-182.10
3	121.09	-507.97	-118.19	-505.07
4	66.00	-313.62	-51.07	-298.69
5				-

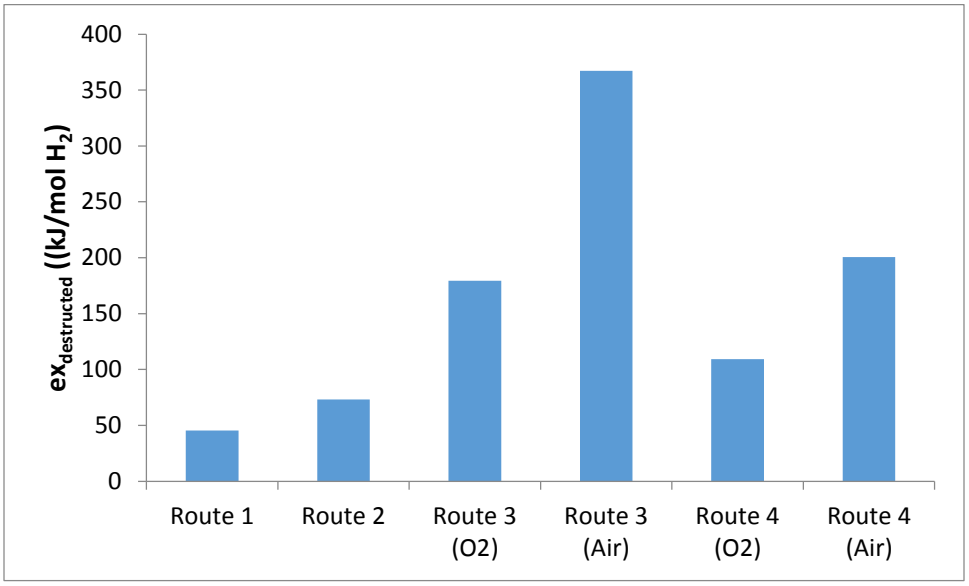

Fig 5.2. Comparison of molar exergy destruction in each route for SO_2 production

using air for routes 3 and 4. It is clear that by using air, the amount of exergy destructed is almost doubled. However, the total released heat stayed unchanged.

Regarding the reacting step (step 2) associated with route 3 and route 4, destructed exergy stayed unchanged when oxygen was replaced by air while the exergy of step 1 and step 2 in both routes increased considerably, approaching three times. Thus, the results analysis reveals that a noticeable amount of irreversibility occurred during physical steps highlighting the critical area to be considered for energy recovery. In route 5, SO_2 is obtained from desulfurization units in operations such as coal-fired power stations. An exergy analysis was not performed for this route. Although the exergy analysis was just performed for the SO_2 production step in the hydrogen production routes using various sulfur-containing compounds as feedstock, overall consideration should be taken so that the potential use of the recovered energy can be found.

Table 5.7 presents the exergetic efficiency results for the different routes of SO_2 production. Relative to the inlet and outlet exergy for a route, the destructed exergy is small, thus the exergy efficiency of all the routes is high.

To this point, there are no existing industrial processes using either of these routes to produce H_2. Of course, the overall energy efficiency will depend on operating factors, like the amount and capacity of the equipment, feedstock availability, and the infrastructure and energy requirements to support the purification steps.

Table 5.7. Exergetic efficiencies of different SO_2 production routes

route no.	inlet exergy (kJ/mol H_2)	outlet exergy (kJ/mol H_2)	destructed exergy (kJ/mol H_2)	η_{ex}*100
1	2880.54	2835.04	45.50	98.42
2	1949.06	1875.92	73.14	96.24
3 (O_2)	2207.41	2027.91	179.49	91.87
3 (Air)	2683.91	2316.82	367.09	86.32
4 (O_2)	1658.82	1549.48	109.34	93.41
4 (Air)	1893.49	1692.86	200.62	89.40
5				-

5.5. Summary

A novel chemical cycle of hydrogen production from splitting hydrogen sulfide has been proposed. This cycle consists of three reactions: SO_2 production, the Bunsen reaction and HI decomposition. The chemical feasibility study of this hydrogen sulfide chemical-splitting cycle has laid the foundation for using sulfur-containing compounds as feedstock to produce hydrogen. Five possible routes, based on the hydrogen sulfide splitting cycle using different sulfur-containing compounds for hydrogen production, are described in this chapter. The main difference among these five routes is the way SO_2 is produced.

Three possible routes use H_2S (H_2S splitting, H_2S splitting when elemental sulfur is further oxidized and direct oxidation of H_2S), which is the waste product of gas plants and the petroleum industry. In route 4, the hydrogen production begins with oxidation of elemental sulfur, which is a byproduct of the Claus Process and is abundant in Canada. The possible fifth route directly uses SO_2 scrubbed from the stack gas of power plants with the aqueous ammonia solutions.

The performed calculations of molar destructed exergy for every single route except route 5 show the inherent energy recovery potential of hydrogen production using different sulfur-containing feedstocks. Direct oxidation of H_2S seems to have the most irreversibility while H_2 production using elemental sulfur as a feedstock could potentially be competitive, depending on the customers' requirements. Either way, the overall efficiencies will depend on further factors, which should be considered for detailed analysis of each route.

CHAPTER SIX

MASS TRANSFER STUDIES OF MULTIPHASE BUNSEN REACTION IN CORNING® ADVANCED-FLOW™ REACTORS

Using an iodine-toluene solution to provide flowing iodine for the Bunsen reaction, renders the reaction to occur at ambient temperature such that side reactions, I_2 vapour deposition, and corrosion challenges can be either overcome or eased. However, using toluene as the iodine solvent makes the Bunsen reaction a multiphase reaction system, which includes gas, aqueous, and organic phases. Therefore, a mass transfer study appears to be necessary in order to enhance process efficiency. Glass-made Corning® Advanced-Flow™ Reactors (the LF and G1-AFRs) were chosen to run the multiphase Bunsen reaction due to their excellent resistance to corrosion and their unique designs to improve mass transfer efficiency of multiphase fluids. In this chapter, I report on the performance of the Corning® Advanced-Flow™ Reactors, studied by estimating the Reynolds numbers based on the operating conditions applied to both the LF and G1-AFRs. Then, the effect of changing feeding positions of reactants was investigated for the LF-AFR and finally the absorption rate of sulfur dioxide was measured for different combinations of a SO_2-water-toluene mixture in both the LF and G1-AFRs. This was followed by a mass transfer study for binary systems including SO_2-water and SO_2-toluene applying the two-film theory to identify the optimum operating conditions to be used when iodine is involved in the multiphase mixture. This chapter has resulted in a paper that is ready for submission. My contributions were set-up preparation, performing the experiments, analyzing the gas and liquid samples, calculating the liquid side overall mass transfer coefficients under the supervision of Dr. Hui Wang at both the University of Saskatchewan and the Corning Reactor Technology Center, China, and drafting the paper. Dr. Wang helped in analyzing results and participated in paper preparation.

6.1. Overall mass transfer coefficient by applying two-film theory in the AFRs

To determine the overall mass transfer coefficients, the two-film theory is introduced in this section. According to this theory [105], the flux of the mass transfer of gas molecules A into liquid through the interface (z = 0) can be written as

$$N_{A,z=0} = \frac{P_A - H_A C_A}{\frac{1}{k_G} - \frac{H_A}{k_L}} = K_G(P_A - P_A') \text{ or } = \frac{\frac{P_A}{H_A} - C_A}{\frac{1}{k_G H_A} - \frac{1}{k_L}} = K_L(c_A' - c_A) \quad (6\text{-}1)$$

where, N_A is the molar flux of A molecules from gas to liquid in the direction perpendicular to the mass transfer (mol m^{-2} s^{-1}), P_A is the partial pressure of SO_2 (Pa), H_A is Henry's law constant (Pa m^3 mol^{-1}), C_A is the concentration of SO_2 in liquid (mol m^{-3}), k_g is the mass transfer coefficient in the gas phase (mol m^{-2} s^{-1} Pa^{-1}) and k_L is the mass transfer coefficient in the liquid phase (m s^{-1}); $P_A' = H_A C_A$, and $C_A' = P_A/H_A$, K_G and K_L are the overall gas phase and liquid phase mass transfer coefficients (mol Pa^{-1} m^{-2} s^{-1} and m s^{-1}), respectively. As explained later in the Section 6.2, the ideal plug-flow model was assumed for liquid and gas in both the LF and G1-AFRs, and the performance equation was developed by combing the rate equation with the material (mole) balance. Taking a slice of the reactor along the material flow direction as the volume element (dV) for mass balance, of which the interface area per volume is a (m^2 m^{-3}, or m^{-1}),

$$\text{A lost in gas phase} = -F_G dy_A = \text{A gained in liquid} = \frac{F_L}{c_t} dc_A = N_{A,z=0}\, a\, dV \quad (6\text{-}2)$$

where, F_G and F_L are the total molar flow rates of gas and liquid (mol s^{-1}), respectively, and C_t is the total concentration of liquid (mol m^{-3}).

Considering $y_A = P_A/P_t$ (P_t is the total pressure of gas), and combining equation (6-1) and equation (6-2), integration on either side gives the reactor size (V_r).

$$V_r = \frac{F_G}{K_G a.P_t}\int_{P_{A1}}^{P_{A2}} \frac{dP_A}{(P_A - P'_A)} = \frac{F_L}{K_L a.c_t}\int_{c_{A1}}^{c_{A2}} \frac{dc_A}{(c'_A - c_A)} \quad (6\text{-}3)$$

Upon integration of the liquid side equation from inlet (C_{A1}) to outlet (C_{A2}), the overall volumetric mass transfer coefficient (K_La) becomes

$$K_L a = \frac{1}{\tau} \mathrm{Ln} \frac{c^*_A - c_{A1}}{c^*_A - c_{A2}} \quad (6\text{-}4)$$

where C^*_A is the equilibrium concentration of SO_2 in liquid phases (water or toluene) corresponding to the partial pressure of SO_2 in the gas phase at the inlet ($P_{SO_2,in}$), C_{A1} is the concentration of SO_2 in the liquid phase at the inlet, which is always zero, τ is the residence time of the liquid flow in the AFR (C_t/F_L) and K_La is the overall volumetric mass transfer coefficient. C^*_A is calculated based on the partial pressure of SO_2 at the reactor inlet using Henry's law; and C_{A2} is obtained at the reactor outlet based on the dissolved SO_2 (the difference between SO_2 inlet and outlet in the gas phase and the liquid flow). Considering the residence time of the liquid, the overall mass transfer coefficients in the LF and G1-AFRs at different operating conditions were estimated using equation (6-4).

6.2. Flow regimes

The specific design of Corning AFRs is somehow different from what is normally observed for straight channels. When the fluid is entered into the heart-shaped cell it hits the first curved

post and splits into two streams until reaching a second cylindrical post where the two streams recombine [85]. Therefore, for hydrodynamics study, the neck of the heart cell (H=400 μm, W=300 μm for the LF-AFR and H=1.12 mm, W=1 mm for the G1-AFR) is considered as the reference to define dimensionless parameters such as the Reynolds number.

$$Re=(\rho u D_h)/\mu \quad (6\text{-}5)$$

where ρ and μ are the average density and viscosity of fluids, respectively, u is the total super-facial velocities of the two phases and D_h is the hydraulic diameter. The calculated ranges for the two-phase Reynolds numbers for the LF-AFR are 2360–3970 for gas and liquid flow rates ranging from 22–85.7 ml/min and 0.3–4.5 ml/min, respectively, which are variable from transition to turbulent. For the G1-AFR these values are 29991–32296 for gas and liquid flow rates ranging from 600–2000 ml/min and 30–90 ml/min, respectively, indicating a fully developed flow at the neck of the heart cell.

Based on the visualization experiments, which were done for a CO_2-water system by Nieves Remacha et al. at MIT [85] by using a G1-AFR, it was observed that two-phase flow in the AFR included a sequence of dynamic events: detachment, elongation, deformation, breakup, and coalescence of bubbles as they passed through the continuous phase. Confined geometry, small dimensions, and the presence of obstacles that disturb the flow mainly caused these events.

Although these dynamic events were quite different from what had been observed in either stirred vessels or straight microchannels, by performing tracer experiments for families of the LF and G1-AFRs, the residence time distribution (RTD) was observed to be narrow [20]. This indicates that each heart-shaped cell can be considered as an ideal stirred vessel where complete

mixing occurs. However, the flow throughout the whole reactor can be treated as plug flow because there was no back mixing among the cells.

6.3. The effect of changing feeding position of reactants

The LF-AFR was chosen to test the effect of mixing the order of the gas mixture of N_2 and SO_2, water, and toluene, using the ports combinations of A1, A2 and A3; A1, A3 and A2, and A3, A2 and A1, respectively. Absorption runs with a constant gas flow rate (85 mL/min at STP) and SO_2 mole fractions (y_{SO_2}=0.824) and two levels of water and toluene flow rates were conducted at room temperature (22 ^oC). Tables 6.1 and 6.2 show the detailed experimental variables and calculated results.

The results indicate that the SO_2 absorption rate by the liquid was independent of the feed positions when other operational parameters such as the SO_2 mole fraction in gas, gas flow rate, liquid flow rate, and toluene to water ratio in liquid were maintained the same. However, the slightly higher absorption rate in the latter table was due to the higher toluene to water ratio used.

To maintain the consistency in the later experiments, the first and second feeding scenarios, for instance mixing SO_2 with either liquid in the first module, were frequently used for most of the runs in the LF and G1-AFRs.

Table 6.1. SO_2 absorption rate measured in the LF-AFR at different inlet positions of gas and liquids (water flow rate=0.5 mL/min, toluene flow rate=0.5 mL/min, gas flow rate=85 mL/min, SO_2 mole fraction=0.824, T=22 ^oC)

A1	A2	A3	SO_2 outlet flow rate (mL/min)	SO_2 outlet mole fraction	SO_2 absorption rate (mol/m^3. s)
water	SO_2-N_2	toluene	16.50	0.5239	15.02
toluene	SO_2-N_2	water	16.55	0.5246	15.00
toluene	water	SO_2-N_2	16.43	0.5228	15.04

Table 6.2. SO_2 absorption rate measured in the LF-AFR at different inlet positions of gas and liquids (water flow rate=0.1 mL/min, toluene flow rate=0.9 mL/min, gas flow rate=85 mL/min, SO_2 mole fraction=0.824, T=22 ^oC)

A1	A2	A3	SO_2 outlet flow rate (mL/min)	SO_2 outlet mole fraction	SO_2 absorption rate (mol/m^3. s)
SO_2-N_2	toluene	water	13.56	0.4749	15.84
SO_2-N_2	water	toluene	13.35	0.4710	15.90
toluene	water	SO_2-N_2	13.39	0.4717	15.89

6.4. SO_2 absorption in water

6.4.1. Absorption in the LF-AFR

Absorption runs with a constant gas flow rate (75 mL/min at STP) at various SO_2 mole fractions were conducted at room temperature (22 ^oC) and three water flow rate levels in the LF-AFR. Table 6.3 shows the detailed experimental variables and calculated results. Figures 6.1 and 6.2 also visually show the effects of the SO_2 mole fraction and water flow rate on the SO_2 absorption rate and the overall liquid-side mass transfer coefficient, respectively.

At a constant mole fraction of sulfur dioxide, a sharp increase could be seen in sulfur dioxide absorption when the flow rate of water was increased. Enhancing the mole fraction of SO_2 at a constant water flow rate also increased the absorption rate.

A strong dependency on water flow rates was observed as well for the overall mass transfer coefficients at constant SO_2 mole fractions. The K_La values almost coincided at the lowest water flow rate at all mole fraction of SO_2 while at higher water flow rates, absorption became larger when the mole fraction of SO_2 was further increased. Nieves-Remacha et al. studied the effects of operating conditions on the hydrodynamics of a water-CO_2 system using a G1-AFR [85]. Based on their observations, the average bubble size and bubble size distribution depend only on the gas and liquid flow rates. Having large bubbles is detrimental to mass transfer due to reduction in the specific interfacial area. At the lowest flow rate of water, most of the heart-shaped cells were occupied by large bubbles, which made inadequate contact between the gas and liquid resulting in poor mass transfer. On the other hand, the bubble size decreased with increasing the liquid flow (Q_L) because of increased shear rates at the inlet of the heart-shaped cells.

At all water flow rates, increasing the mole fraction of sulfur dioxide raised the inlet (c^*_{A1}) and outlet (c^*_{A2}) equilibrium concentrations of sulfur dioxide in the water, respectively, leading to

Table 6.3. Details of overall mass transfer calculations for SO_2-water in the LF-AFR

(gas flow rate =75 mL/min, T=22 ^oC, A1: water and A2: SO_2-N_2)

Q_L (mL/min)	$y_{A\ in}$	$P_{t\ in}$ (kPa)	C^*_{A1} (mol/L)	$P_{t\ out}$ (kPa)	C^*_{A2} (mol/L)	C_{A2} (mol/L)	1/t (1/s)	Ln(X)*	K_L.a*100 (1/s)
0.3	0.636	231	2.02	148	1.21	1.10	0.00189	0.786	0.148 ± 0.01
	0.737	231	2.33	148	1.42	1.32	0.00189	0.836	0.158 ± 0.01
	0.824	258	2.91	148	1.60	1.73	0.00189	0.903	0.170 ± 0.02
	0.933	231	2.96	145	1.82	1.86	0.00189	0.990	0.187 ± 0.01
0.5	0.636	251	2.19	145	1.12	1.11	0.00314	0.707	0.222 ± 0.01
	0.737	245	2.47	144	1.33	1.29	0.00314	0.736	0.231 ± 0.01
	0.824	238	2.68	141	1.48	1.58	0.00314	0.891	0.280 ± 0.01
	0.933	238	3.04	141	1.75	2.00	0.00314	1.07	0.337 ± 0.01
0.7	0.636	258	2.24	144	1.06	1.04	0.00440	0.624	0.275 ± 0.01
	0.737	258	2.60	141	1.24	1.27	0.00440	0.669	0.295 ± 0.01
	0.824	231	2.61	137	1.40	1.46	0.00440	0.822	0.362 ± 0.01
	0.933	231	2.95	134	1.63	1.88	0.00440	1.01	0.446 ± 0.01

* the second term of equation (6-4)

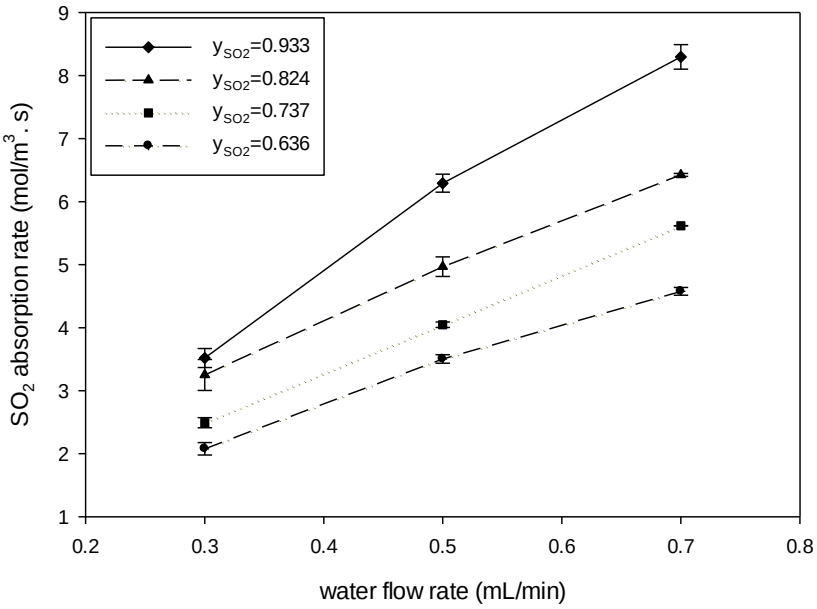

Fig 6.1. SO_2 absorption rate versus water flow rate in the LF-AFR (gas flow rate=75 mL/min, T=22 ^oC, A1: water and A2: SO_2-N_2)

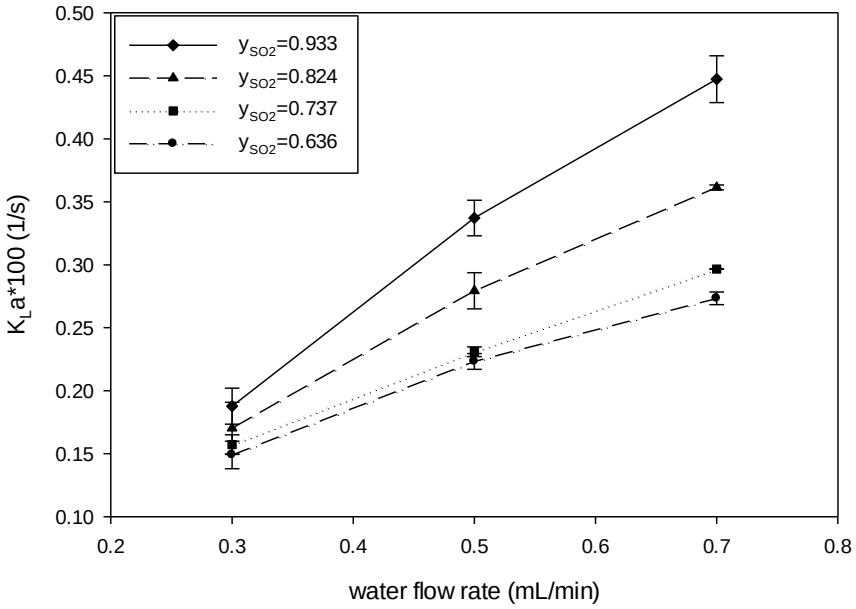

Fig 6.2. Overall mass transfer coefficients of SO_2 versus water flow rate in the LF-AFR (gas flow rate =75 mL/min, T=22 ^oC, A1: water and A2: SO_2-N_2)

an increase in overall mass transfer coefficients. Comparing the values of c_{A2}^{*} with the c_{A2}, two different behaviours were observed. At low mole fraction values of sulfur dioxide, C_{A2} stayed below the equilibrium values, while at high mole fractions, the latter was higher. This was mainly due to the higher partial pressure of sulfur dioxide at the inlet that made SO_2 dissolve quickly in water. However, at the outlet when the pressure dropped significantly, the new equilibrium was hard to reach and the outlet concentration (C_{A2}) became oversaturated.

Absorption rates with a constant mole fraction of gas (y_{SO_2}=0.933) at various gas flow rates (at STP) were also measured at room temperature (22 ^{o}C) and three water flow rate levels. Table 6.4 shows the detailed experimental variables and calculated results. Figures 6.3 and 6.4 also show the effects of gas flow rate and water flow rate on the SO_2 absorption rate and the overall liquid-side mass transfer coefficient.

At constant water flow rates, no significant changes were observed as the flow rate of gas was increased. However, at constant Q_G, SO_2 absorption was significantly elevated when the liquid flow rate was increased. Despite the sharp increase in gas flow rates, the overall mass transfer coefficients tended to decrease gently. Most likely, increasing the gas flow rate shifted the average bubble size to a larger value at a constant liquid flow rate. Nieves-Remacha et al. first observed this phenomenon for a CO_2-water system using a G1-AFR. The bubble size distributions kept becoming broader by increasing the gas flow rates with a larger effect at the lowest water flow rate, whereas increasing the liquid flow rate narrowed the bubble size distribution [85]. When the gas flow rates were increased for each level of water flow rate, the amounts of C_{A1}^{*} and C_{A2}^{*} were increased accordingly. On the other hand, the amount of absorbed SO_2 (C_{A2}) remained quite constant for all three water flow rate levels. As a result, at each level, the logarithm term of the overall mass transfer coefficients (shown in equation (6-4)) began to decrease and then the

Table 6.4. Details of overall mass transfer calculations for SO_2-water in the LF-AFR

(SO_2 mole fraction=0.933, T=22 ^oC, A1: water and A2: SO_2-N_2)

Q_L (mL/min)	Q_G (mL/in)	$P_{t\ in}$ (kPa)	C^*_{A1} (mol/L)	$P_{t\ out}$ (kPa)	C^*_{A2} (mol/L)	C_{A2} (mol/L)	1/t (1/s)	Ln(X)*	$K_L.a*100$ (1/s)
0.3	53.57	191	2.45	125	1.56	1.62	0.00189	1.09	0.205 ± 0.01
	64.29	219	2.79	142	1.79	1.67	0.00189	0.910	0.172 ± 0.02
	75.00	232	2.97	152	1.92	1.65	0.00189	0.814	0.154 ± 0.02
	85.72	252	3.22	163	2.06	1.66	0.00189	0.725	0.137 ± 0.01
0.5	53.57	205	2.62	125	1.53	1.69	0.00314	1.04	0.325 ± 0.02
	64.29	219	2.80	131	1.63	1.77	0.00314	1.00	0.316 ± 0.01
	75.00	239	3.06	142	1.76	1.86	0.00314	0.938	0.295 ± 0.01
	85.72	259	3.31	152	1.90	1.87	0.00314	0.830	0.261 ± 0.01
0.7	53.57	198	2.53	118	1.41	1.60	0.00440	0.998	0.439 ± 0.01
	64.29	218	2.79	124	1.51	1.65	0.00440	0.897	0.395 ± 0.01
	75.00	232	2.97	131	1.61	1.77	0.00440	0.911	0.401 ± 0.02
	85.72	252	3.22	142	1.74	1.87	0.00440	0.867	0.382 ± 0.01

* the second term of equation (6-4)

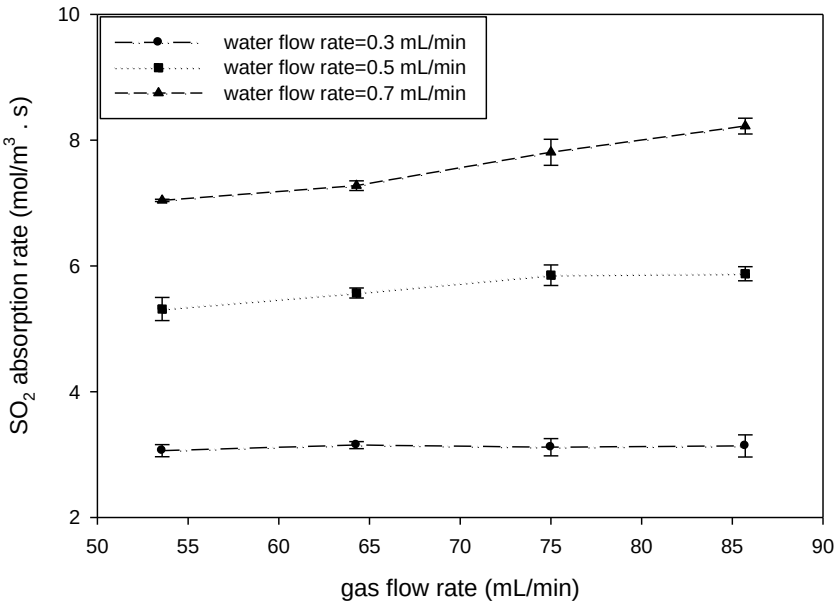

Fig 6.3. SO_2 absorption rate versus gas flow rate in the LF-AFR (SO_2 mole fraction=0.933, T=22 ^oC, A1: water and A2: SO_2-N_2)

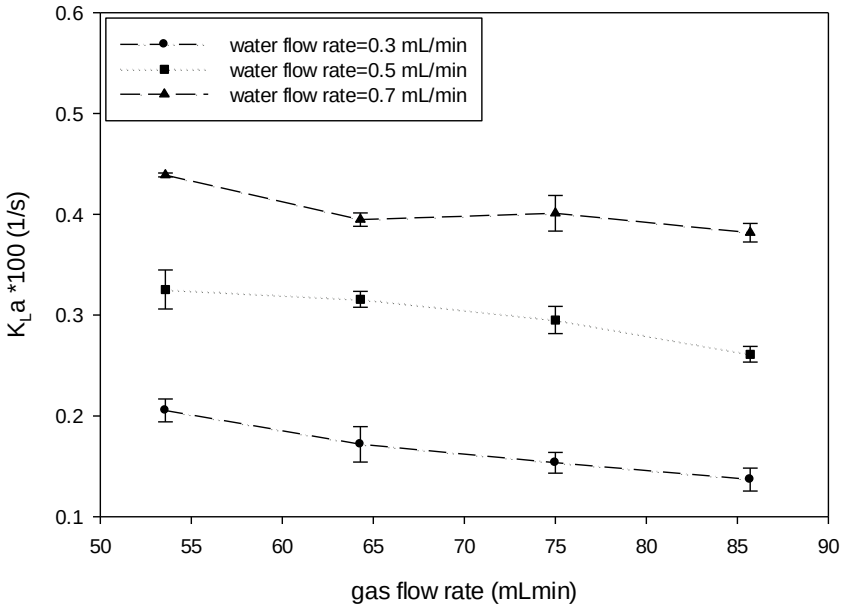

Fig 6.4. Overall mass transfer coefficients of SO_2 versus gas flow rate in the LF-AFR (SO_2 mole fraction=0.933, T=22 ^oC, A1: water and A2: SO_2-N_2)

coefficients became smaller at higher gas flow rates. Comparing the values of c^*_{A2} with c_{A2}, oversaturation was also observed for most of the runs.

6.4.2. Absorption in the G1-AFR

Absorption runs with a constant mole fraction of gas (y_{SO_2}=0.50) at various SO_2 flow rates at STP were conducted at room temperature (22 ^oC) and four water flow rate levels in the G1-AFR. Table 6.5 shows the detailed experimental variables and calculated results. Figures 6.5 and 6.6 show the effects of SO_2 flow rate and water flow rate on the SO_2 absorption rate and the overall liquid-side mass transfer coefficient, respectively.

At a constant flow rate of gas, a gradual increase could be seen in sulfur dioxide absorption when the flow rate of water was increased. The absorption rate of sulfur dioxide was also increased steadily by enhancing the flow rate of gas at a constant water flow rate. On the other hand, the relevant overall mass transfer coefficient values were quite constant as the water flow rate was further increased at a constant gas flow rate and they tended to decline marginally at the higher water flow rates while the K_La values were smoothly increased as the flow rate of gas was enhanced. This observation is not quite in agreement with our findings in the LF-AFR and the study of the CO_2-water system by Nieves-Remacha et al. [85] since no significant change was observed by varying the gas and liquid flow rates in the G1-AFR.

As can be seen from Table 6.5, at a constant gas flow rate, the value of C_{A2} was decreased by increasing the flow rates of water, while C^*_{A1} was increased, making smaller quantities of the second term of equation (6-4). On the other hand, the residence time was decreased, which in turn resulted in the increase of 1/t values. Therefore, quite constant overall mass transfer coefficients could be obtained regardless of varying the gas and liquid flow rates.

Table 6.5. Details of overall mass transfer calculations for SO_2-water in the G1-AFR

(SO_2 mole fraction=0.50, T=22 ^oC, A1: water and A2: SO_2-N_2)

Q_L (mL/min)	Q_G (mL/in)	$P_{t\ in}$ (kPa)	C^*_{A1} (mol/L)	$P_{t\ out}$ (kPa)	C^*_{A2} (mol/L)	C_{A2} (mol/L)	1/t (1/s)	Ln(X)*	$K_L.a*100$ (1/s)
30	1600	191	1.31	102	0.45	0.63	0.06250	0.657	4.10 ± 0.02
	1800	184	1.26	102	0.47	0.66	0.06250	0.745	4.65 ± 0.04
	2000	205	1.40	102	0.46	0.75	0.06250	0.761	4.75 ± 0.03
45	1600	205	1.40	102	0.38	0.49	0.09372	0.430	4.03 ± 0.02
	1800	205	1.40	102	0.40	0.54	0.09372	0.482	4.51 ± 0.01
	2000	226	1.55	102	0.40	0.60	0.09372	0.487	4.56 ± 0.02
50	1600	219	1.50	102	0.35	0.48	0.10417	0.383	3.98 ± 0.02
	1800	226	1.55	102	0.36	0.52	0.10417	0.411	4.27 ± 0.01
	2000	240	1.64	102	0.38	0.56	0.10417	0.416	4.33 ± 0.01
60	1600	226	1.55	102	0.33	0.41	0.12500	0.307	3.83 ± 0.01
	1800	240	1.64	102	0.33	0.46	0.12500	0.329	4.11 ± 0.02
	2000	260	1.78	102	0.34	0.50	0.12500	0.332	4.14 ± 0.02

* the second term of equation (6-4)

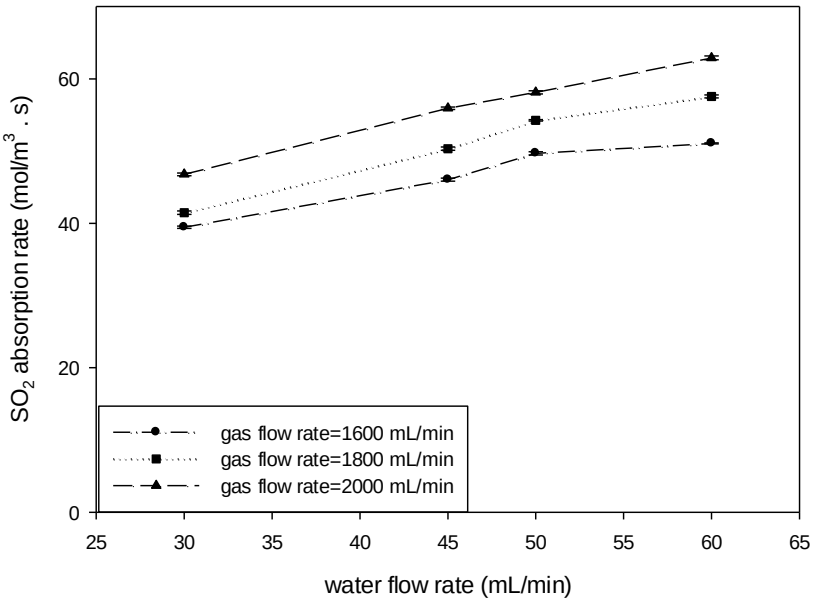

Fig 6.5. SO_2 absorption rate versus water flow rate in the G1-AFR (SO_2 mole fraction=0.50, T=22 ^oC, A1: water and A2: SO_2-N_2)

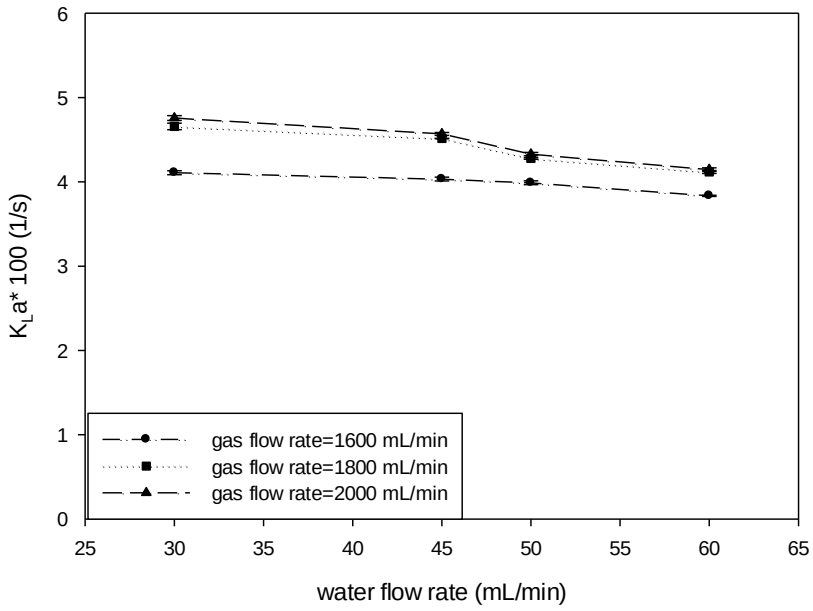

Fig 6.6. Overall mass transfer coefficients of SO_2 versus water flow rate in the G1-AFR (SO_2 mole fraction=0.5, T=22 ^oC, A1: water and A2: SO_2-N_2)

6.5. SO_2 absorption in toluene

6.5.1. Absorption in the LF-AFR

Absorption runs with a constant gas flow rate (75 mL/min at STP) at various SO_2 mole fractions were conducted at room temperature (22 ^oC) and three toluene flow rate levels. Table 6.6 shows the detailed experimental variables and calculated results. Figures 6.7 and 6.8 also show the effects of SO_2 mole fraction and toluene flow rate on the SO_2 absorption rate and the overall liquid-side mass transfer coefficient. The absorption rate and K_La values were increased when SO_2 mole fractions and toluene flow rates were further increased.

As can be seen, the values of the outlet equilibrium concentrations (c^*_{A2}) are always larger than the outlet concentration (c_{A2}) of SO_2 in toluene, showing toluene's high tendency for SO_2 absorption. This tendency became even greater when the gas phase had less resistance against mass transfer. Figure 6.7 shows the significant drop in total pressure at a constant toluene flow rate, leading to a fairly large gap between the highest mole fraction (y_{SO_2}=0.933) and the other three mole fraction levels.

Absorption rates with a constant mole fraction of gas (y_{SO_2}=0.933) at various gas flow rates (at STP) were also measured at room temperature (22 ^oC) and three toluene flow rate levels. Table 6.7 shows the detailed experimental variables and calculated results. Figures 6.9 and 6.10 also show the effects of gas flow rate and toluene flow rate on the SO_2 absorption rate and the overall liquid-side mass transfer coefficient where the resistance of the gas phase is negligible.

Increasing the toluene flow rate at constant gas flow rates increased the rates of absorption and overall mass transfer coefficients. At a constant toluene flow rate, mass transfer coefficients were also sharply increased by increasing gas flow rates.

Table 6.6. Details of overall mass transfer calculations for SO_2-toluene in the LF-AFR

(gas flow rate =75 mL/min, T=22 ^oC, A1: toluene and A2: SO_2-N_2)

Q_L (mL/min)	$y_{A\ in}$	$P_{t\ in}$ (kPa)	C^*_{A1} (mol/L)	$P_{t\ out}$ (kPa)	C^*_{A2} (mol/L)	C_{A2} (mol/L)	1/t (1/s)	Ln(X)*	$K_L.a*100$ (1/s)
0.65	0.636	202	5.78	133	2.67	1.80	0.00400	0.373	0.149 ± 0.01
	0.737	202	6.69	126	3.08	2.22	0.00400	0.404	0.162 ± 0.01
	0.824	202	7.48	123	3.59	2.59	0.00400	0.425	0.170 ± 0.01
	0.933	169	7.08	116	4.22	3.41	0.00400	0.658	0.263 ± 0.01
0.90	0.636	217	6.20	130	2.31	1.47	0.00563	0.271	0.152 ± 0.01
	0.737	210	6.96	124	2.65	1.84	0.00563	0.307	0.173 ± 0.01
	0.824	204	7.52	120	3.14	2.16	0.00563	0.339	0.191 ± 0.01
	0.933	176	7.36	109	3.56	2.83	0.00563	0.484	0.273 ± 0.01
1.27	0.636	238	6.78	127	1.83	1.22	0.00797	0.199	0.158 ± 0.01
	0.737	231	7.62	120	1.93	1.56	0.00797	0.228	0.182 ± 0.01
	0.824	203	7.52	116	2.55	1.73	0.00797	0.261	0.208 ± 0.01
	0.933	177	7.41	107	2.86	2.20	0.00797	0.353	0.281 ± 0.01

* the second term of equation (6-4)

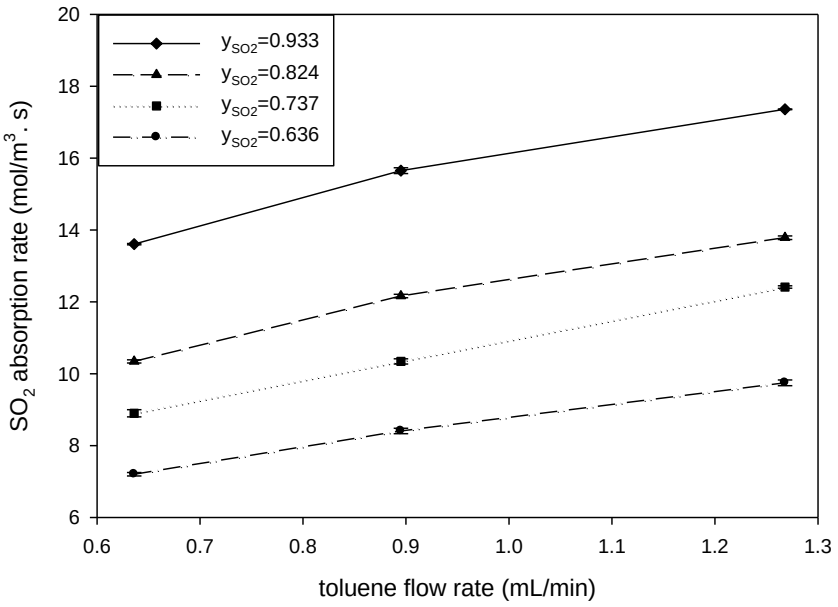

Fig 6.7. SO_2 absorption rate versus toluene flow rate in the LF-AFR (gas flow rate =75 mL/min, T=22 ^oC, A1: toluene and A2: SO_2-N_2)

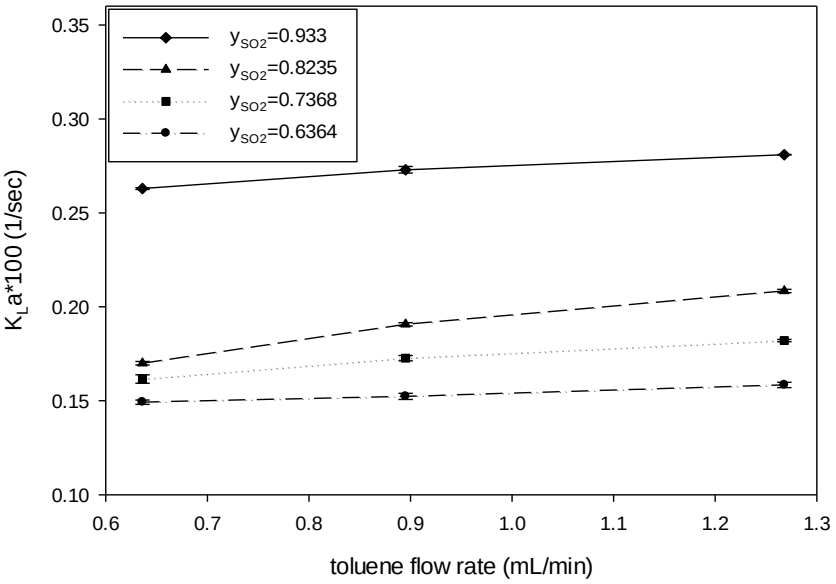

Fig 6.8. Overall mass transfer coefficients of SO_2 versus toluene flow rate in the LF-AFR (gas flow rate =75 mL/min, T=22 ^oC, A1: toluene and A2: SO_2-N_2)

Table 6.7. Details of overall mass transfer calculations for SO_2-toluene in the LF-AFR

(SO_2 mole fraction=0.933, T=22 ^oC, A1: toluene and A2: SO_2-N_2)

Q_L (mL/min)	Q_G (mL/in)	$P_{t\ in}$ (kPa)	C^*_{A1} (mol/L)	$P_{t\ out}$ (kPa)	C^*_{A2} (mol/L)	C_{A2} (mol/L)	1/t (1/s)	Ln(X)*	$K_L.a*100$ (1/s)
0.65	53.57	148	6.21	95.0	3.14	2.81	0.00400	0.603	0.241 ± 0.01
	64.29	162	6.79	109	3.82	3.14	0.00400	0.622	0.249 ± 0.01
	75.00	169	7.08	116	4.22	3.41	0.00400	0.658	0.263 ± 0.01
	85.72	176	7.31	119	4.41	3.76	0.00400	0.723	0.289 ± 0.01
0.90	53.57	148	6.21	95.0	2.65	2.20	0.00563	0.438	0.247 ± 0.01
	64.29	162	6.79	95.0	2.90	2.54	0.00563	0.469	0.264 ± 0.01
	75.00	176	7.36	109	3.56	2.83	0.00563	0.484	0.273 ± 0.01
	85.72	183	7.65	112	3.81	3.11	0.00563	0.522	0.294 ± 0.01
1.27	53.57	142	5.96	96.0	2.02	1.65	0.00797	0.324	0.258 ± 0.01
	64.29	158	6.63	96.0	2.33	1.94	0.00797	0.346	0.276 ± 0.01
	75.00	177	7.41	107	2.86	2.20	0.00797	0.353	0.281 ± 0.01
	85.72	184	7.69	110	3.16	2.46	0.00797	0.385	0.307 ± 0.01

* the second term of equation (6-4)

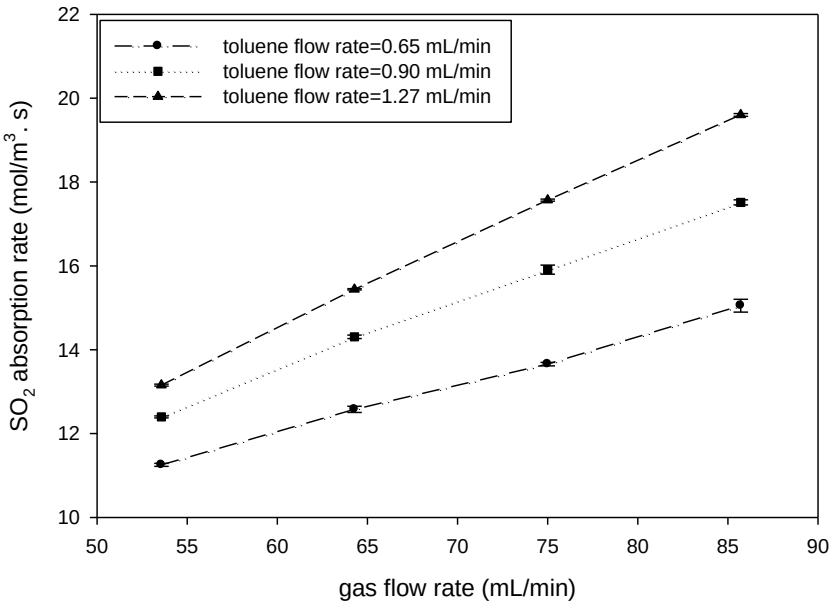

Fig 6.9. SO_2 absorption rate versus gas flow rate in the LF-AFR (mole fraction of SO_2=0.933, T=22 ^oC, A1: toluene and A2: SO_2-N_2)

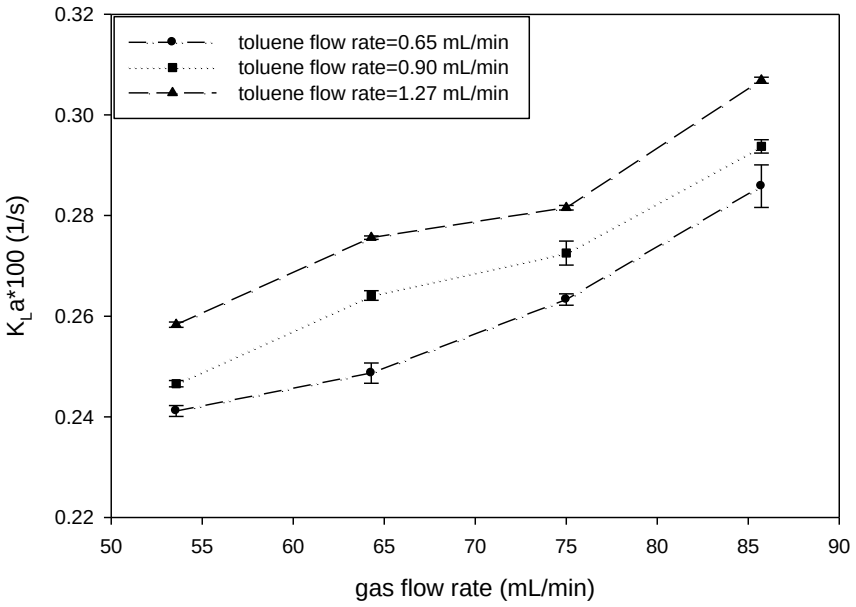

Fig 6.10. Overall mass transfer coefficients of SO_2 versus gas flow rate in the LF-AFR (mole fraction of gas=0.933, T=22 ^oC, A1: toluene and A2: SO_2-N_2)

Increasing the flow rates of gas made an increase in the inlet partial pressures and c^*_{A1} values. On the other hand, increasing the amount of absorbed SO_2 at the outlet (c_{A2}) made the logarithm term in equation (6-4) larger, accordingly. Thus, larger mass transfer coefficients were obtained at higher gas flow rates.

6.5.2. Absorption in the G1-AFR

Absorption runs with a constant gas mole fraction (y_{SO_2}=0.50) at various SO_2 flow rates at STP were conducted at room temperature (22 ^oC) and four toluene flow rate levels. Table 6.8 shows the detailed experimental variables and calculated results. Figures 6.11 and 6.12 show the effects of increasing the gas and toluene flow rates on the SO_2 absorption rate and the overall liquid-side mass transfer coefficient.

The absorption rate values increased quite sharply at the beginning and they became fairly constant at the higher flow rate of toluene. Except for the highest flow rate, almost constant values were recorded for K_La parameters in the toluene-SO_2 system while they were gradually increased by increasing the gas flow rate.

By comparing the data obtained in the G1-AFR to the work by Nieves-Remacha et al. [85], who used a Corning G1-AFR for CO_2 and water with flow rates ranging from 5.6–103 ml/min and 10–80 ml/min, respectively, their calculated mass transfer coefficients (0.13~1.5 s^{-1}) were 1 order of magnitude larger. Indeed, the reason for obtaining smaller mass transfer coefficient values in this work could be the different gas-liquid system or assumption for calculation.

Table 6.8. Details of overall mass transfer calculations for SO_2-toluene in the G1-AFR

(SO_2 mole fraction=0.50, T=22 ^oC, A1: toluene and A2: SO_2-N_2)

Q_L (mL/min)	Q_G (mL/in)	$P_{t\ in}$ (kPa)	C^*_{A1} (mol/L)	$P_{t\ out}$ (kPa)	C^*_{A2} (mol/L)	C_{A2} (mol/L)	1/t (1/s)	Ln(X)*	$K_L.a*100$ (1/s)
39.63	1600	171	3.83	102	0.37	0.58	0.08256	0.164	1.35 ± 0.01
	1800	185	4.14	102	0.38	0.64	0.08256	0.168	1.38 ± 0.01
	2000	192	4.30	102	0.41	0.66	0.08256	0.168	1.39 ± 0.01
59.45	1600	219	4.92	102	0.23	0.48	0.12385	0.103	1.28± 0.01
	1800	233	5.23	102	0.25	0.53	0.12385	0.107	1.33 ± 0.01
	2000	247	5.54	102	0.25	0.59	0.12385	0.113	1.40 ± 0.01
66.06	1600	219	4.92	102	0.23	0.43	0.13763	0.092	1.27± 0.01
	1800	233	5.23	102	0.24	0.48	0.13763	0.096	1.32 ± 0.01
	2000	247	5.54	102	0.25	0.53	0.13763	0.100	1.38 ± 0.01
79.26	1600	267	6.00	102	0.18	0.38	0.16513	0.066	1.10 ± 0.01
	1800	274	6.15	102	0.18	0.43	0.16513	0.073	1.20 ± 0.01
	2000	281	6.31	102	0.21	0.46	0.16513	0.076	1.26 ± 0.01

* the second term of equation (6-4)

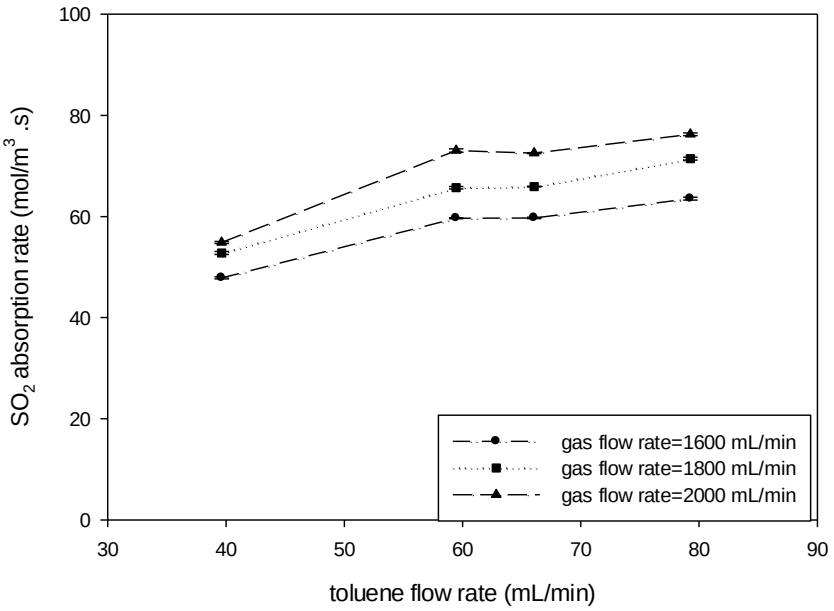

Fig 6.11. SO_2 absorption rate versus toluene flow rate in the G1-AFR (SO_2 mole fraction=0.50, T=22 ^oC, A1: toluene and A2: SO_2-N_2)

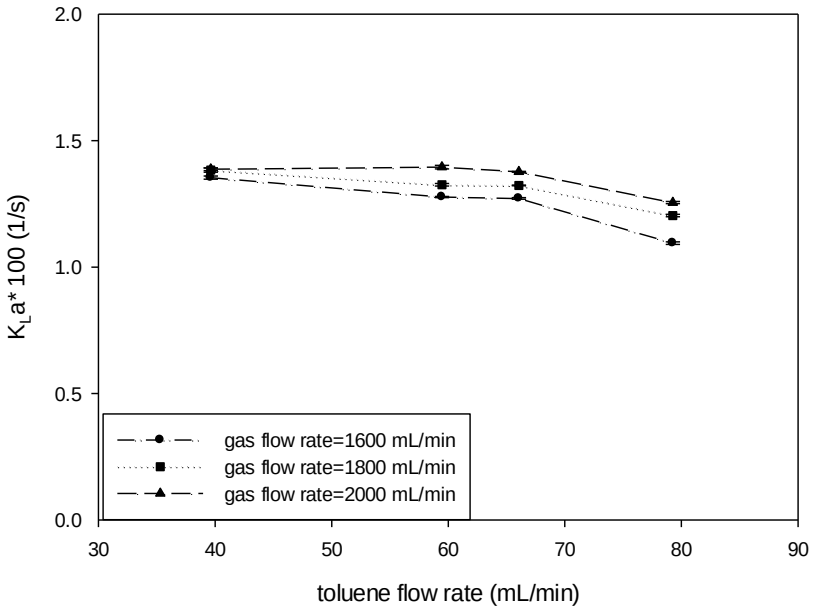

Fig 6.12. Overall mass transfer coefficients of SO_2 versus toluene flow rate in the G1-AFR (SO_2 mole fraction=0.50, T=22 ^oC, A1: toluene and A2: SO_2-N_2)

6.6. Comparison between the results of mass transfer study in the LF and G1-AFRs

In this section, SO_2 absorption runs are conducted with one-module LF-AFR and the results are compared with the runs of five-module LF-AFR measured in the Sections 6.4.1 and 6.5.1. Then, the new SO_2 absorption results of one-module LF-AFR are compared with the results of the SO_2 absorption runs in the G1-AFR presented in the Sections 6.4.2 and 6.5.2.

SO_2 absorption runs were conducted using four water flow rate levels (0.3, 0.5, 0.7 and 1.0 mL/min) and four toluene flow rate levels (0.65, 0.9, 1.27 and 1.5 mL/min) with a one-module LF-AFR and a constant mole fraction (y_{SO_2}=0.933) and flow rate (53.57 mL/min at STP) of sulfur dioxide at room temperature. The results are shown in Tables 6.9 and 6.10. Similar absorption, i.e., the amount of SO_2 absorbed per second, was observed, compared with that by the five-module LF-AFR, indicating that under the conditions used, absorption is mainly conducted in the first module. To calculate K_La using equation (6-4), when the concentration terms are similar, residence time, or the number of fluidic modules, results in different values of K_La. In other words, in five-module experiments, the last four modules may not contribute significantly in absorption, but the longer residence time linearly decreased the K_La values.

The newly conducted SO_2 absorption runs using one-module LF-AFR were also compared with the runs using one-module G1-AFR with a constant mole fraction (y_{SO_2}=0.50) and flow rate (2000 mL/min at STP) of sulfur dioxide for four water flow rate levels (30, 45, 50 and 60 mL/min) and four toluene flow rate levels (39.6, 59.5, 66.1 and 79.3 mL/min) at room temperature and the results are shown in Tables 6.11 and 6.12. To unify the effects of liquid flow rate and reactor volume on the K_La variation, the ratio of the liquid flow rate to the reactor volume was used for comparison.

Table 6.9. Comparison between SO_2-water absorption runs in the LF-AFR using different fluidic modules

	one-fluidic module LF-AFR		five-fluidic module LF-AFR	
Q_L (mL/min)	SO_2 absorption * 10^6 (mol/s)	$K_L.a$ * 100 (1/s)	SO_2 absorption * 10^6 (mol/s)	$K_L.a$ * 100 (1/s)
0.3	7.55	1.18	8.11	0.205
0.5	13.1	1.90	14.1	0.325
0.7	18.5	2.55	18.7	0.439
1.0	24.5	3.19	25.1	0.545

Table 6.10. Comparison between SO_2-toluene absorption runs in the LF-AFR using different fluidic modules

	one-fluidic module LF-AFR		five-fluidic module LF-AFR	
Q_L (mL/min)	SO_2 absorption * 10^6 (mol/s)	$K_L.a$ * 100 (1/s)	SO_2 absorption * 10^6 (mol/s)	$K_L.a$ * 100 (1/s)
0.65	29.7	1.66	29.8	0.241
0.90	32.6	1.69	32.9	0.247
1.27	34.8	1.70	34.9	0.258
1.50	35.0	1.71	35.1	0.266

Table 6.11. Comparison between SO_2-water absorption runs using the LF-AFR and the G1-AFR

one-fluidic module LF-AFR			one-fluidic module G1-AFR		
Q_L (mL/min)	(Q_L/V_r)	$K_L.a$ * 100 (1/s)	Q_L (mL/min)	(Q_L/V_r)	$K_L.a$ * 100 (1/s)
0.3	0.8	1.18	30	3.8	4.75
0.5	1.3	1.90	45	5.6	4.56
0.7	1.8	2.55	50	6.3	4.33
1.0	2.5	3.19	60	7.5	4.14

Table 6.12. Comparison between SO_2-toluene absorption runs using the LF-AFR and the G1-AFR

one-fluidic module LF-AFR			one-fluidic module G1-AFR		
Q_L (mL/min)	(Q_L/V_r)	$K_L.a$ * 100 (1/s)	Q_L (mL/min)	(Q_L/V_r)	$K_L.a$ * 100 (1/s)
0.65	1.6	1.66	39.6	4.9	1.39
0.9	2.3	1.69	59.5	7.4	1.40
1.27	3.2	1.70	66.1	8.2	1.38
1.5	3.8	1.71	79.3	9.9	1.26

As can be seen in Table 6.11, for the SO_2-water binary system, increasing the Q_L/V_r from 0.8 to 2.5 in the LF-AFR resulted in a significant increase in the K_La values from 1.18 to 3.19. Apart from the opposite trend that is observed for the same system in the G1-AFR, i.e., decreasing K_La with the increase of the Q_L/V_r values, the K_La for both reactors are in the same order of magnitude indicating that the SO_2 absorption in both reactors was almost the same and a seamless scaling-up was observed from the LF-AFR to the G1-AFR. The results presented in Table 6.12 also point out the fact that the SO_2 absorption efficiency is quite similar in both reactors.

6.7. SO_2 absorption in water-toluene mixture

Calculating mass transfer coefficients in a ternary system is somewhat difficult using typical models such as bi-film theory [106]. Therefore, to predict the behaviour of a three-phase system, only absorption rates were studied for both the LF and G1-AFRs in this section.

6.7.1. Absorption in the LF-AFR

The absorption runs with a constant mole fraction of SO_2 (y_{SO_2}=0.933) and liquid flow rate (1.5 mL/min) at various gas flow rates (at STP) were conducted at room temperature (22 ^oC) and five water volumetric fraction levels in the liquid phase where the gas phase resistance was negligible. Figure 6.13 shows the effects of increasing the volumetric fraction of water and the gas flow rate on the SO_2 absorption rate.

The absorption rates were significantly enhanced as the flow rate of gas increased. A sharp decreasing trend in absorption rates could also be seen when the toluene fraction was reduced. In other words, water retarded the mass transfer rates due to having a lower solubility for SO_2 compared to toluene and this decreasing trend became more significant at higher water fractions.

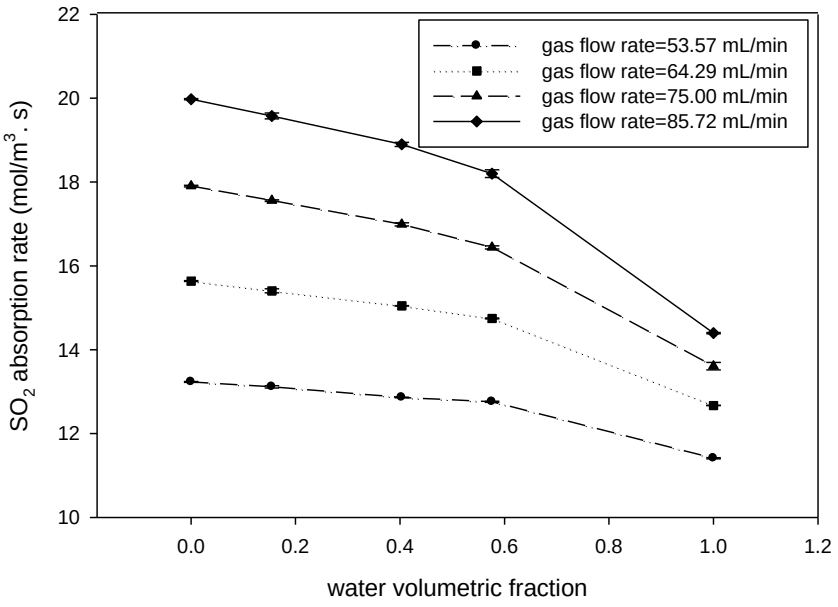

Fig 6.13. SO_2 absorption rate versus water volumetric fraction in the LF-AFR (mole fraction of SO_2=0.933, liquid flow rate=1.5 mL/min, T=22 ^oC, A1: toluene, A2: SO_2-N_2 and A3: Water)

The absorption runs with constant mole fraction of gas (y_{SO_2}=0.933) and water volumetric fraction (0.25) at various gas flow rates (at STP) were also conducted at room temperature (22 ^oC) and five liquid flow rate levels where the gas phase resistance was negligible. Figure 6.14 shows the effects of the liquid flow rate and gas flow rate on the SO_2 absorption rate. At all gas levels, enhancing liquid flow rates increased the absorption rates. However, larger liquid flow rates gave a smooth rise to absorption values. This was mainly due to the complete absorption of SO_2 in toluene. It is expected to reach a flat line when the flow rate is further increased. Absorption rates of SO_2 were also increased at a constant liquid flow rate by increasing gas flow rates, leading to an increase in mass transfer at high flow rates.

6.7.2. Absorption in the G1-AFR

The absorption runs with a constant mole fraction of gas (y_{SO_2}=0.50) and water volumetric fraction (0.15) at various gas flow rates (at STP) were also conducted at room temperature (22 ^oC) and four liquid flow rate levels. Figure 6.15 shows the effects of the liquid flow rate and gas flow rate on the SO_2 absorption rate.

Increasing the liquid flow rates smoothly increased the absorption rates. Increasing gas flow rates also increased the absorption rates of SO_2 at a constant liquid flow rate. Unlike the LF-AFR, larger values for absorption rates were measured by using the G1-AFR where the water fraction was further increased. In fact, when the water fraction was increased, the rate of absorption was enhanced accordingly.

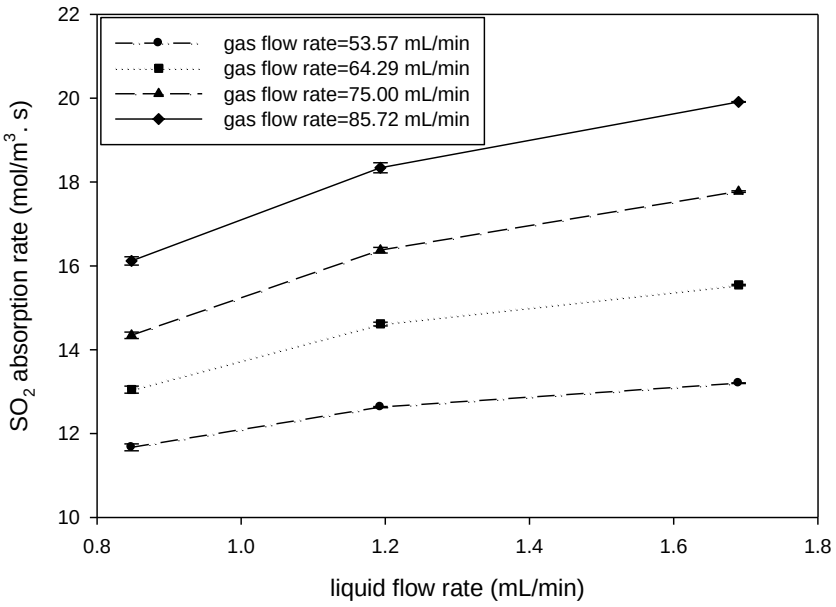

Fig 6.14. SO_2 absorption rate versus liquid flow rate in the LF-AFR (mole fraction of SO_2=0.933, water volumetric fraction [water/toluene] =0.25 [0.33], T=22 ^oC, A1: toluene, A2: SO_2-N_2 and A3: Water)

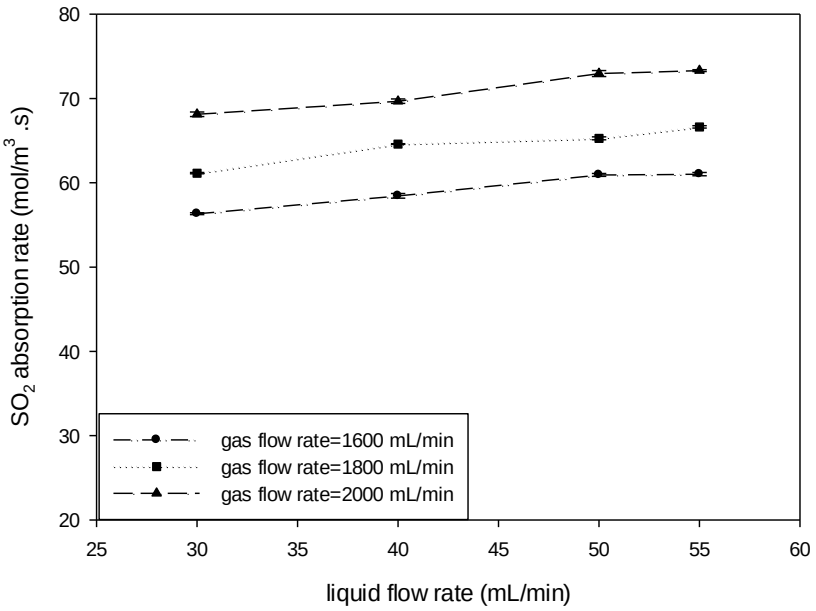

Fig 6.15. SO_2 absorption rate versus liquid flow rate in the G1-AFR (mole fraction of SO_2=0.50, water volumetric fraction [water/toluene] =0.15 [0.17], T=22 ^oC, A1: SO_2-N_2, A2: toluene and A3: Water)

6.8. Summary

Corning® Advanced-Flow™ Reactors can be used to conduct the multiphase Bunsen reaction, where toluene is used to dissolve iodine. In this chapter, the absorption rates of sulfur dioxide have been measured for different combinations of the SO_2-water-toluene mixture in the LF-AFR and the G1-AFR including SO_2-water and SO_2-toluene binary systems and the SO_2-water-toluene ternary system to identify the optimum operating conditions to be used when iodine is involved in the multiphase mixture. The overall mass transfer coefficients have also been calculated for the binary systems. The mass transfer coefficients were highly dependent on the gas and the liquid flow rates for the binary systems in the LF-AFR, however this dependency was not observed for the G1-AFR. Gas phase composition played a big role in the SO_2-toluene binary system where the K_La values were smaller for the situations with the highest gas phase resistance. Comparing the K_La values for both reactors, smaller quantities were unexpectedly obtained for the LF-AFR. Therefore, the SO_2 absorption runs were repeated with a one-module LF-AFR and the results were compared with the runs of five-module LF-AFR. Similar absorption, i.e., the amount of SO_2 absorbed per second, was observed, compared with that by the five-module LF-AFR, indicating that under the conditions used, absorption was mainly conducted in the first module and the addition of extra fluidic modules after contacting module did not contribute to the increase of the rate of absorption and most of the SO_2 was absorbed in the contacting module. The new results of the one-module LF-AFR were also compared with the results of the SO_2 absorption runs in the G1-AFR. It was concluded that the absorption efficiency was quite similar in both the LF and G1- AFRs as the K_La were in the same order of magnitude for both reactors.

CHAPTER SEVEN

MULTIPHASE BUNSEN REACTION IN CORNING® ADVANCED-FLOW™ REACTORS

This chapter presents my investigation of the Bunsen reaction. This key reaction was studied by feeding SO_2 gas, water, and I_2/toluene solution into the LF and G1-AFRs. SO_2 and I_2 were used as the limiting reactants in turn, and the effects of operating conditions on the rate of SO_2 and I_2 in the AFRs were studied. The SO_2 absorption rate was measured based on the difference of the molar flow rate of SO_2 in the gas phase per unit volume and the I_2 reaction rate was measured based on the difference of the molar flow rate of I_2 in the I_2/toluene solution at the inlet and outlet of the reactors. Based on the previous work [17], the excess amount of water was used compared with the amount that stoichiometry required for all the reaction runs. The research in this chapter has resulted in a paper that is ready for submission. My contributions were set-up preparation, and performing the experiments, analyzing the gas and liquid samples, measuring SO_2 absorption and I_2 reaction rates under the supervision of Dr. Hui Wang at both the University of Saskatchewan and the Corning Reactor Technology Center, China, and drafting the paper. Dr. Wang helped in analyzing the results and participated in the paper's preparation.

7.1. Bunsen reaction in the LF-AFR

As discussed in Chapter 3, the LF-AFR (the smallest model of the Corning reactor products) was used in this study at the University of Saskatchewan. The internal volume of each fluidic module of the LF-AFR is about 0.4 mL to be used for liquid flow rates in the range of 0–10 mL/min. Five modules were used: Module 1 had two fluid inlet ports (A1 and A2), allowing two fluids to mix and/or react. Module 2 had one inlet port (A3), allowing a third fluid to be

preheated. All the fluids met at the third module, mixing and reacting, which continued in modules 4 and 5 to increase the residence time. The experiments in this section were carried out at ambient temperature (22-70 ^{o}C) at different gas flow rates ranging from 22 to 85.7 mL/min at standard temperature and pressure (STP), and at different liquid flow rates from 1.5 to 4.5 ml/min.

7.1.1. The effect of increasing water volumetric fraction (SO_2 as the limiting reactant)

The runs at a constant SO_2 mole fraction of gas (y_{SO_2}= 0.909), liquid flow rate (4.0 mL/min), and gas flow rate (22 mL/min at STP) were conducted in the LF-AFR at room temperature (22 ^{o}C) and three water volumetric fraction levels (0.125, 0.25 and 0.380). Table 7.1 lists the inlet and outlet values of the flow rates of the reactants and products. The SO_2 flow rate was either lower than or close to that of I_2, rendering SO_2 the limiting reactant with nearly complete conversion because only trace amounts of sulfur dioxide were detected in the effluent gas phase for all the runs. I_2 could not be balanced based on the data listed in Table 7.1. The 15 to 33% missed iodine/iodide species is explained later. But the amount of proton (H^+) produced could be used to make the charge balance with iodide and sulfate anions, assuming all the converted SO_2 became sulfate. Figure 7.1 shows the effects of increasing the water volumetric fraction in the liquid on the SO_2 absorption and the I_2 reaction rates. An identical SO_2 absorption rate was observed regardless of the varying water fraction in the liquid and the inclusion or exclusion of the Bunsen reaction, which is clearly due to the nearly complete conversion of SO_2. However, in the Bunsen reaction, the reaction rate of I_2 was greater than that of SO_2 at a smaller water fraction in the liquid, and they became the same when the volumetric fraction of water in the liquid was 0.38.

According to Bunsen reaction stoichiometry, it is expected that two moles of water converts one mole of SO_2 and one mole of I_2 into acid products – sulfuric acid and iodic acid.

Table 7.1. Flow rate values of reactants and products corresponding to Fig 7.1

	inlet I_2 (mmol/min)	inlet SO_2 (mmol/min)	outlet I_2 (mmol/min)	outlet I^- (mmol/min)	outlet H^+ (mmol/min)
1	1.40	0.9	0.28	1.33	2.97
2	1.20	0.9	0.17	1.53	3.40
3	1.00	0.9	0.09	1.52	3.39

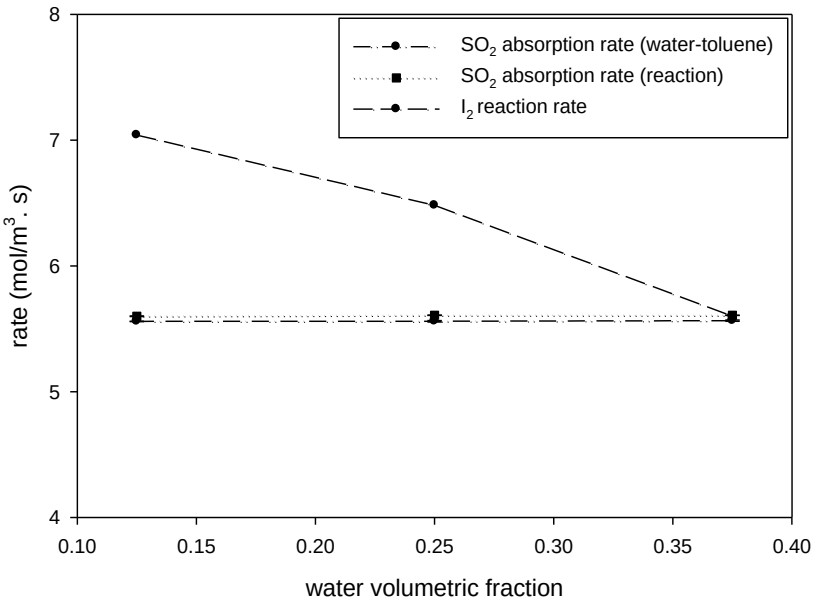

Fig 7.1. SO_2 absorption and I_2 reaction rates versus water volumetric fraction in the LF-AFR (mole fraction of SO_2=0.909, liquid flow rate=4.0 mL/min, [I_2]=0.4 mol/L, gas flow rate=22 mL/min, T=22 ^oC, A1: toluene (toluene-iodine), A2: SO_2-N_2 and A3: water)

$$2H_2O + I_2 + SO_2 \rightarrow H_2SO_4 + 2HI \quad (7.1)$$

Assuming all the SO_2 was consumed in each run, the calculated amount of H^+ agreed with the measured I^- values, however the converted I_2 was more than stoichiometry predicted for all the runs. The following reaction may have converted some of the iodine to tri-iodide:

$$I_2 + I^- \rightarrow I_3^- \quad (7.2)$$

Since iodine solubility in the HI solution is substantially higher than in water and the existence of iodide (I^-) and proton (H^+) would greatly increase the iodine solubility in water, therefore, the iodine crystals could dissolve rapidly in an iodide aqueous solution by forming soluble tri-iodide ions (I_3^-). Moreover, poly-iodine species, I_{2X}, where x=1, 2, 3, 4 etc., could also be stabilized by H^+ in the solution [37].

Zhu et al. [107] studied the kinetic and thermodynamic properties of the Bunsen reaction in the sulfur-iodine water-splitting cycle in a stirred reactor. Including reactions (7.2) and (7.3), they assumed that the produced tri-iodide took part in the following reaction as well. They considered the complex Bunsen reaction as a kinetically controlled reaction by neglecting mass transfer impacts. Then, they derived the rate of elementary reactions and a kinetic model was proposed:

$$2H_2O + I_3^- + SO_2 \rightarrow SO_4^{2-} + 3I^- + 4H^+ \quad (7.3)$$

Their experimental results agreed quite well with the proposed kinetic model. By calculating the apparent activation energies, they concluded that the complex Bunsen reaction was controlled by elementary reactions (7.2) and (7.3) as is suggested here. Therefore, the formation of I_3^- may be one of the reasons that led to I_2 unbalanced. The errors in analytical chemistry methods may be another contribution. However, the experiment shows that the maintenance of equal I_2 and SO_2 feeding rates would lead to their nearly complete conversion into acid products.

7.1.2. The effect of increasing gas flow rate (I_2 as the limiting reactant)

The runs with a constant mole fraction of gas (y_{SO_2}=0.933), liquid flow rate (1.5 mL/min), and water volumetric fraction (0.15) were conducted in the LF-AFR at room temperature (22 ^oC) and four gas flow rate levels (53.6, 64.3, 75.0 and 85.7 mL/min). Table 7.2 lists the inlet and outlet values of the flow rates of SO_2 and I_2. The inlet flow rate of SO_2 in this group of runs was 4 to 7 times that of the I_2, rendering I_2 the limiting reactant. Under this condition, the conversion of I_2 became constant at about 93%, regardless of the increase of gas flow. The difference between the inlet and outlet SO_2, which increased with the gas flow rate, was mainly due to SO_2 absorption. Figure 7.2 confirms this by showing that the SO_2 absorption rate was much greater than the I_2 reaction rate. Figure 7.2 also compares the SO_2 absorption rate by toluene, toluene-water mixture, and toluene-I_2 solution-water mixture. It can be seen that when the reaction became insignificant, the gas flow rate enhanced the interface mass transfer, which controlled the SO_2 absorption rate. The increase of the gas flow rate did not change the I_2 reaction rate, indicating that mass transfer did not control the reaction. Considering possible errors in the experiment, the constant conversion of 93%, observed with the increasing gas flow, may indicate the reaction had reached equilibrium conversion.

Table 7.2. Flow rate values of reactants and products corresponding to Fig 7.2

	$(I_2)_{in}$ (mmol/min)	$(SO_2)_{in}$ (mmol/min)	$(H_2O)_{in}$ (mmol/min)	$(I_2)_{out}$ (mmol/min)	$(SO_2)_{out}$ (mmol/min)
1	0.51	2.23	12.8	0.036	0.096
2	0.51	2.67	12.8	0.035	0.15
3	0.51	3.13	12.8	0.035	0.23
4	0.51	3.57	12.8	0.035	0.33

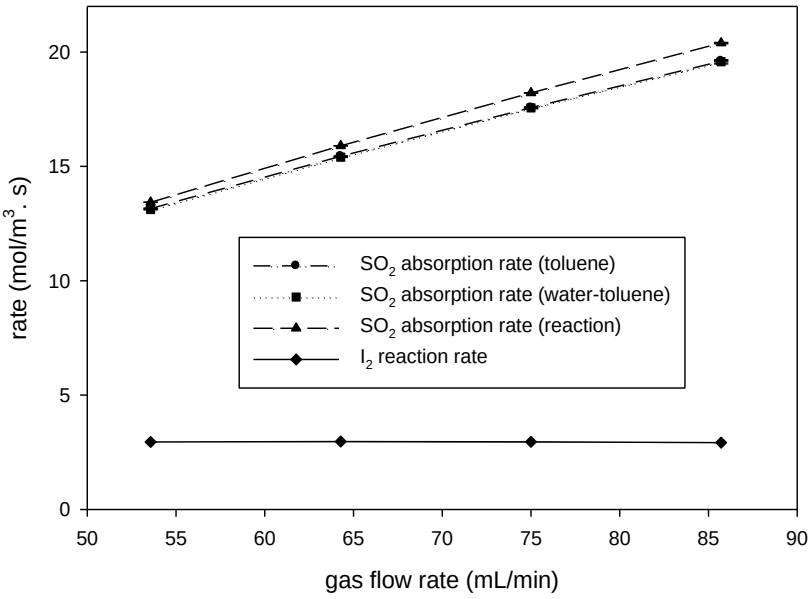

Fig 7.2. SO_2 absorption and I_2 reaction rates versus gas flow rate in the LF-AFR (mole fraction of SO_2=0.933, [I_2] = 0.4 mol/L, liquid flow rate=1.5 mL/min, water volumetric fraction=0.15, T=22 ^oC, A1: toluene (toluene-iodine), A2: SO_2-N_2 and A3: water)

7.1.3. The effect of increasing liquid flow rate (I_2 as the limiting reactant)

The runs with a constant mole fraction of gas (y_{SO_2}=0.933) and gas flow rate (53.57 mL/min at STP) were conducted at room temperature (22 ^oC) at three liquid flow rate levels with a constant water volumetric fraction (0.15) in the LF-AFR. SO_2 was excessive and I_2 was the limiting reactant. Table 7.3 shows the flow rate values of SO_2 and I_2. Figure 7.3 shows a constant SO_2 absorption rate but an increasing I_2 reaction rate. With a constant SO_2 feeding rate and sufficient liquid flow, the SO_2 was nearly completely absorbed, leading to only trace amounts of SO_2 in the existing gas. This is why a constant SO_2 absorption rate was observed. On the other hand, the increase in the liquid flow rate increased the feed rate of I_2; seemingly, it also led to the increase of the I_2 reaction rate. However, data in Table 7.3 show a constant conversion of I_2. That means under this condition, the Bunsen reaction was still equilibrium controlled.

7.1.4. The effect of increasing temperature (I_2 as the limiting reactant)

The runs with a constant mole fraction of gas (y_{SO_2}=0.933) and gas flow rate (53.57 mL/min at STP) were conducted at a constant liquid flow rate (1.5 mL/min) with a constant water volumetric fraction (0.15) in the LF-AFR at four different temperature levels where I_2 was the limiting reactant. As can be seen from Figure 7.4, SO_2 solubility was decreased by varying the temperature both for physical absorption and the reaction, while enhancement was observed for the absorption rates of SO_2 in the Bunsen reaction, especially at higher temperatures. On the other hand, increasing the temperature did not have any specific impact on the iodine reaction rate and it stayed quite constant at all temperature levels. Giaconia et al. [6] also investigated the LLE phase separation behaviour of products of the Bunsen reaction and noticed that temperature had little or no effect on the sulfuric acid and HI concentrations in the two phases unless using a huge amount

Table 7.3. Inlet and outlet values of reactants corresponding to Fig 7.3

	inlet I_2 (mmol/min)	inlet SO_2 (mmol/min)	inlet H_2O (mmol/min)	outlet I_2 (mmol/min)	I_2 conversion (%)
1	0.507	2.23	12.8	0.0340	93
2	1.01	2.23	25.6	0.0760	92
3	1.52	2.23	38.3	0.144	91

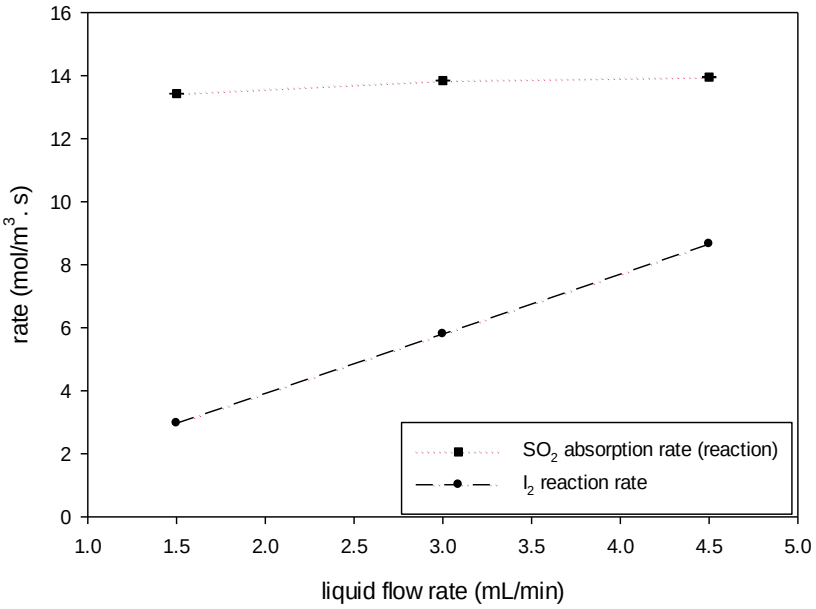

Fig 7.3. SO_2 absorption and I_2 reaction rates versus liquid flow rate in the LF-AFR (mole fraction of SO_2=0.933, water volumetric fraction=0.15, [I_2]=0.4 mol/L, gas flow rate=53.57 mL/min, T=22 ^oC, A1: (toluene-iodine), A2: SO_2-N_2 and A3: water)

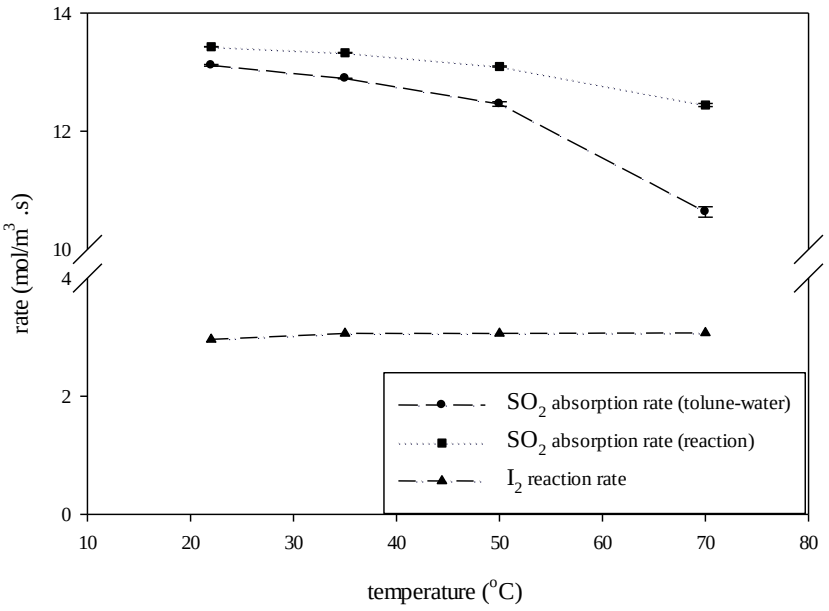

Fig 7.4. SO_2 absorption and I_2 reaction rates versus temperature in the LF-AFR (mole fraction of SO_2=0.933, liquid flow rate=1.5 ml/min, water volumetric fraction=0.15, $[I_2]$=0.4 mol/L, gas flow rate=53.57 mL/min, A1: toluene (toluene-iodine), A2: SO_2-N_2 and A3: Water)

of iodine at 120 ^{o}C.

7.2. Bunsen reaction in the G1-AFR

As explained in Chapter 3, the second set of experiments was conducted in the G1-AFR at the Corning Reactor Technology Center, China, in order to understand the effects of scaling-up on the Bunsen reaction. The internal volume of each fluidic module of the G1-AFR is about 20 times higher than the LF-AFR, at 8 mL with a maximum allowable flow rate of 200 mL/min for the liquids. The other conditions of both reactors are the same such as material, geometry, and design operating conditions. For this study only two fluidic modules (1 and 3) were used, modules 1 for mixing the SO_2-N_2 with the I_2-toluene solution and modules 3 for the reaction where water was directly introduced. The experiments were carried out at ambient temperature (22-80 ^{o}C) at different gas flow rates ranging from 600 to 2000 mL/min at standard temperature and pressure (STP), and at different liquid flow rates ranging from 30 to 90 ml/min.

7.2.1. The effect of increasing temperature (SO_2 as the limiting reactant)

The runs at a constant SO_2 mole fraction of gas (y_{SO_2}=0.50), liquid flow rate (80.0 mL/min), and two-gas flow rate levels (600 and 800 mL/min at STP) were conducted at a constant water volumetric fraction level (0.125) and at three temperature levels (22, 50 and 80 ^{o}C). Table 7.4 lists the inlet and outlet values of the flow rates of the reactants and products for a gas flow rate of 800 mL/min. Figure 7.5 also shows the SO_2 absorption and I_2 reaction rates versus temperature for two gas flow rate levels (600 and 800 mL/min at STP).

Table 7.4. Flow rate values of reactants and products corresponding to Fig 7.5 for gas flow rate=800 mL/min

no.	T (^{o}C)	inlet I_2 (mmol/min)	inlet SO_2 (mmol/min)	outlet I_2 (mmol/min)	outlet I^- (mmol/min)	outlet H^+ (mmol/min)
1	22	28.3	17.9	5.16	30.8	64.8
2	50	28.6	17.9	7.31	27.5	60.9
3	80	28.3	17.9	7.35	27.2	59.1

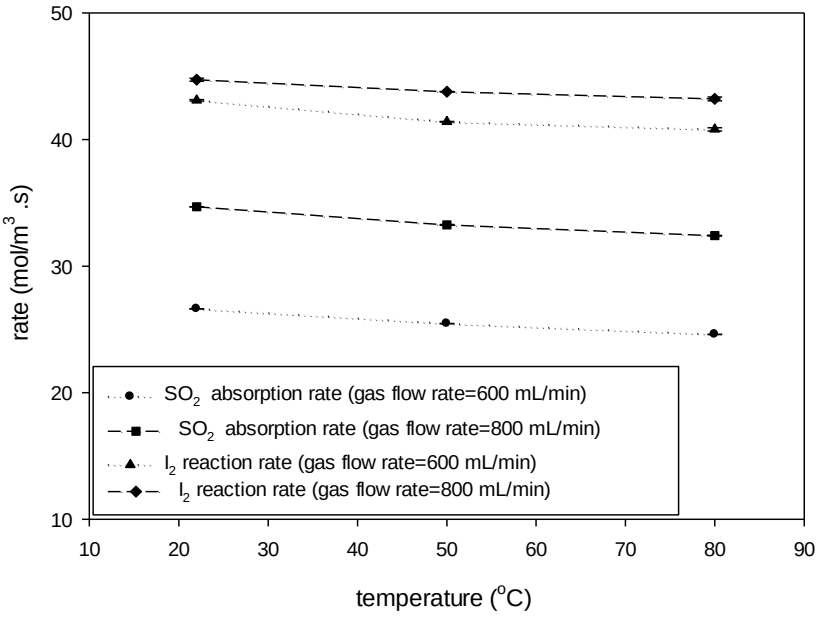

Fig 7.5. SO_2 absorption and I_2 reaction rates versus temperature in the G1-AFR (liquid flow rate=80 mL/min, mole fraction of SO_2=0.50, water volumetric fraction=0.125, $[I_2]$=0.4 mol/L, A1: (SO_2-N_2), A2: (toluene-I_2) and A3: Water)

Assuming total consumption of SO_2 for the run 1, the calculated H^+ value agreed with the measured I^- values, however the I_2 conversion was decreased at higher temperatures from 80% at 22 ^oC to 73.8 % at 80 ^oC resulting in smaller quantities of the H^+ and I^- produced. The converted I_2 was also more than stoichiometry predicted for all the runs. As discussed earlier, the missed iodine/iodide species could be due to the formation of I_3^- leading to I_2 unbalanced.

As shown in Figure 7.5, a sharp increase in SO_2 absorption was observed by increasing the gas flow rate from 600 to 800 mL/min at all temperature levels. As expected, at both gas flow rates, SO_2 absorption also decreased due to the lower solubility of gas at high temperatures. When it came to the iodine reaction rate, a relatively constant amount of consumption was obtained regardless of increasing the gas flow rate.

Attempts were made to match the I_2 reaction rate in the G1-AFR with the experiment performed with the same conditions in the LF-AFR. For this purpose, run 1 conducted in the LF-AFR in the Section 7.1.1 was selected to be compared with run 1 in this section, which was 20 times larger in terms of the gas and liquid flow rates: 400 mL/min for the SO_2 flow rate and 80 mL/min for the liquid flow rate in the G1-AFR versus 20 mL/min for the SO_2 flow rate, and 4 mL/min for the liquid flow rate in the LF-AFR at the same water volumetric fraction (0.125) and the same temperature (ambient). Under these conditions, the I_2 reaction rate for the LF-AFR was 7.05 $mol/m^3.s$ while the I_2 reaction rate rendered the value of 44.75 $mol/m^3.s$ in the G1-AFR. As can be seen, the difference is significant and cannot be ignored. Therefore, the parameter that affected the discrepancies between the results must be considered. As explained earlier, for the Bunsen reaction study three fluidic modules were used for the LF-AFR runs while only one fluidic module (V_r=8 mL) was used for the G1-AFR. By assuming only one fluidic module for the LF-AFR to be used for the reaction (V_r=0.4 mL), the I_2 reaction rate would take the value of 46.70

mol/m^3.s. Due to a higher surface area to volume, a higher reaction rate was always expected in the LF-AFR; therefore, this newly calculated rate is most likely the real value. In this way, by using only one fluidic module for the LF-AFR, the residence time of both reactors could be also scaled up. Thus, the new calculation suggests that the reaction have been completed at the contacting module in both reactors.

7.2.2. The effect of increasing temperature (I_2 as the limiting reactant)

The runs with a constant mole fraction of gas (y_{SO_2}=0.50), liquid flow rate (30 mL/min), and water volumetric fraction (0.15), were conducted at two gas flow rates (1600 mL/min and 1800 mL/min) at STP and three temperature levels (22, 50 and 80 ^oC). Figure 7.6 shows the effects of increasing the temperature on the SO_2 absorption and I_2 reaction rates.

As can be seen, increasing the temperature reduced the SO_2 absorption rate in liquid at both gas flow rate levels; however, this variation had no significant effect on the I_2 reaction rate. I_2 conversion was also quite constant and no significant difference was observed when the temperature was increased. These results are completely in agreement with the similar runs performed in the LF-AFR. One may question the reason of conducting the experiments below 80 ^oC. The main objective of choosing toluene as the I_2 solvent was to lower the reaction temperature. For this reason few levels were randomly selected and it was observed that increasing temperature not only helped in increasing the yields of products but also decreased the sulfur dioxide dissolution in the liquids. Therefore, further increase in temperature above 80 ^oC was no longer needed in both reactors.

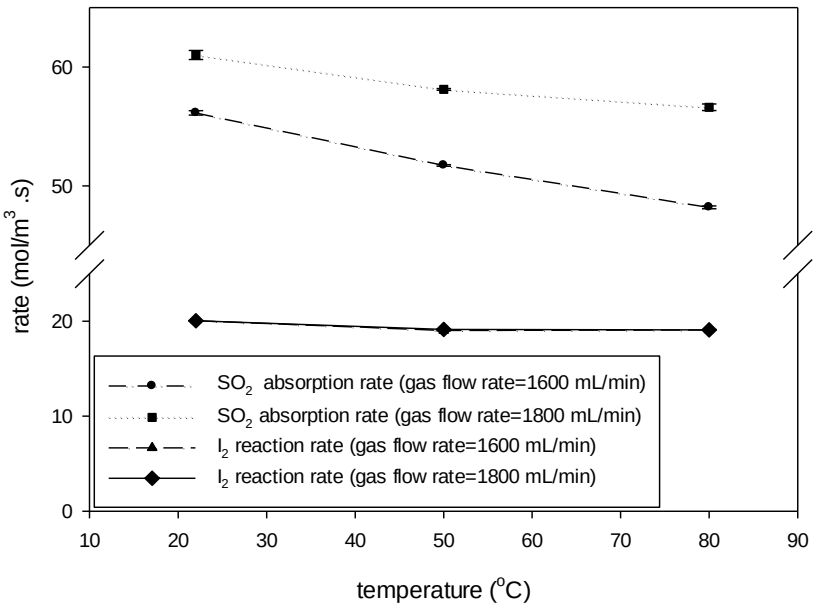

Fig 7.6. SO_2 absorption rate and I_2 reaction rate versus temperature in the G1-AFR (liquid flow rate=30 mL/min, mole fraction of SO2=0.50, water volumetric fraction=0.15, $[I_2]$=0.4 mol/L, A1: (SO_2-N_2), A2: (toluene-I_2) and A3: Water)

7.2.3. The effect of increasing liquid flow rate (I_2 as the limiting reactant)

The runs with a constant mole fraction of gas (y_{SO_2}=0.50) and gas flow rate (1800 mL/min at STP) were conducted at room temperature (22 ^oC) at six liquid flow rate levels with a constant water volumetric fraction (0.15) when SO_2 was excessive and I_2 was the limiting reactant. Table 7.5 shows the flow rate values of SO_2 and I_2. Figure 7.7 also shows the effect of increasing the liquid flow rate on the SO_2 absorption and I_2 reaction rates. The data in Table 7.5 show an almost constant conversion of I_2 regardless of varying the liquid flow rate significantly, indicating that the Bunsen reaction was still equilibrium controlled, which is similar to the results shown for the LF-AFR in the Section 7.1.3. Although the increase in the liquid flow led to the increase of the I_2 reaction rate, quite constant quantities of SO_2 absorption were obtained. Table 7.6 compares the results obtained for I_2 conversion and reaction rates in the LF-AFR, shown in the Section 7.1.3, with the runs (30, 60 and 90 mL/min) shown in this section by assuming the volume of one fluidic module for the LF-AFR. With SO_2 as the excess reactant, the results of Table 7.6 suggest a seamless scale-up when the liquid flow rate and the residence times were increased twenty times from the LF-AFR to the G1-AFR and all data almost coincide for the same operating conditions.

Table 7.5. Inlet and outlet values of reactants corresponding to Fig 7.7

no.	liquid flow rate (mL/min)	inlet I_2 (mmol/min)	inlet SO_2 (mmol/min)	inlet H_2O (mmol/min)	outlet I_2 (mmol/min)	I_2 conversion (%)
1	30	10.3	40.2	250	0.68	93.4
2	40	13.4	40.2	333	0.97	92.7
3	45	14.6	40.2	375	1.16	92.1
4	55	18.9	40.2	458	1.52	91.9
5	60	20.5	40.2	500	2.19	89.3
6	90	30.5	40.2	750	3.42	88.8

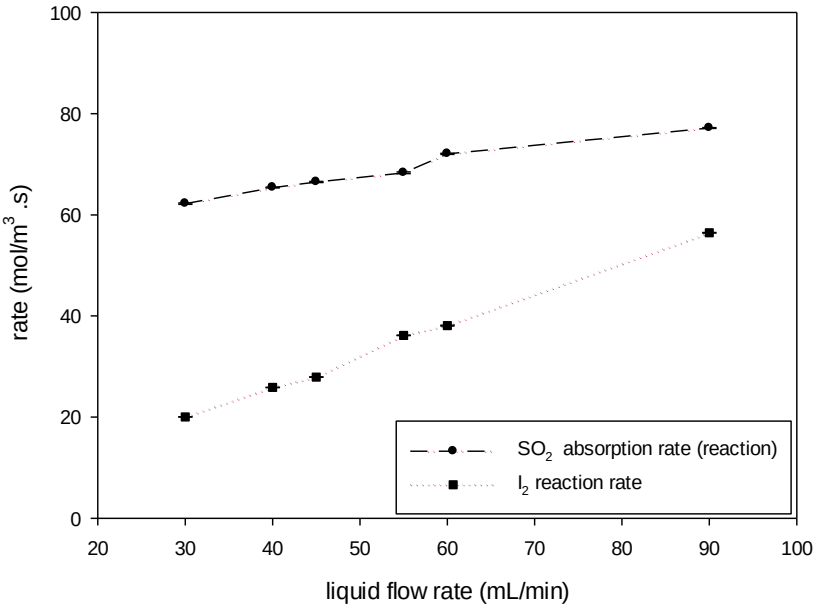

Fig 7.7. SO_2 absorption and I_2 reaction rates versus liquid flow rate in the G1-AFR (mole fraction of SO_2=0.50, water volumetric fraction=0.15, [I_2]=0.4 mol/L, gas flow rate=1800 mL/min, T=22 ^oC, A1: (SO_2-N_2), A2: (toluene-I_2) and A3: Water)

Table 7.6. Comparison of the results obtained in the LF (Section 7.1.3) and G1-AFRs

no.	liquid flow in LF (mL/min)	I_2 reaction rate ($mol/m^3.s$)	I_2 conversion (%)	liquid flow rate in G1 (mL/min)	I_2 reaction rate ($mol/m^3.s$)	I_2 conversion (%)
1	1.5	19.6	93	30	20	93
2	3.0	39.1	92	60	38.1	89
3	4.5	57.3	91	90	56.5	89

7.3. Summary

Compared to the conventional solvent-free routes for conducting the Bunsen reaction, toluene played the role of the organic solvent to carry iodine and SO_2 for the Bunsen reaction in the continuous Corning® Advanced-Flow™ Reactors. In this way, technical difficulties of GA reaction schemes were tackled effectively. No side reaction occurred either in the gas phase or in the liquid phase. Iodine vapour deposition, corrosion and huge excess amount of water and iodine were also avoided. Similar to the batch reactor results, the products of the Bunsen reaction were formed in the water phase when I_2-toluene contacted water. The feasibility of the direct separation of the Bunsen reaction products at room temperature was also previously discussed in the Chapter 3 using electrolysis.

The multiphase Bunsen reaction was conducted in the Corning-AFRs in this chapter when SO_2 and I_2 were used as the limiting reactants in turn, and the effects of operating conditions on the rates of SO_2 and I_2 were studied. No significant enhancement for sulfur dioxide absorption was observed by the reaction. Increasing the temperature reduced the SO_2 absorption rate in the liquid; however, this variation had no significant effect on the I_2 reaction rate in both reactors. It has also been determined that an increase in gas and liquid flow rates did not lead to a noticeable change in the iodine conversion in both reactors and the conversion of the iodine seems to have reached its equilibrium. By scaling-up twenty times, nearly similar data were obtained for both the LF-AFR and the G1-AFR indicating seamless scale-up for this reaction system.

CHAPTER EIGHT

A PLANT DESIGN TO PRODUCE HYDROGEN, BASED ON H_2S-H_2O SPLITTING CYCLE

In this chapter, a design for a hydrogen production plant is presented, based on the low-temperature process that was developed in Dr. Hui Wang's research group and the use of Corning AFRs for H_2S oxidation and the Bunsen reaction. The capacity of 51,000 tonnes/year of hydrogen was chosen according to the amount needed for a typical heavy oil upgrader. *Ulrich's Chemical Engineering (Process Design and Economics)* [108] and a Chemical Engineering Plant cost index value of 567 from *IHS Global Insight* [109] were used to design equipment. The rest of the sizing of equipment was done in a variety of ways including scaling-up from smaller processes, using the experimental results obtained in the Corning® Advanced-Flow™ Reactors from previous chapters, and applying engineering judgments to better understand the size of equipment needed. Students taking the course, CHE 422 (Process Engineering and Design II), performed the design work under my supervision and participation.

8.1. Process description

As previously discussed, the H_2S and H_2S-H_2O splitting cycles convert waste hydrogen sulfide from oil sands bitumen upgrading into hydrogen as a more value-added material. The process consists of three sections: In the Section 1, H_2S reacts with sulfuric acid where multiphase products are formed including downgraded sulfuric acid, elemental sulfur and sulfur dioxide in the gas phase. It is important to maximize the amount of SO_2 produced in this section to be consumed as the reactant for the Bunsen reaction. In the Section 2, this SO_2 reacts with water and iodine to produce HI and H_2SO_4 using the low-temperature process (described in Chapter 3) where the

Bunsen reaction runs at ambient temperature to substantially mitigate technical problems in the GA conventional reaction scheme. Finally, in the Section 3, the products of the Section 2 can be directly electrolyzed to produce hydrogen at room temperature. Figure 8.1 shows the details of this process.

In the following contents, the design of the H_2S-H_2O splitting cycle is explained in detail in three different sections where the auxiliary equipment and material selection for each section is clarified. Finally, an economic analysis is performed based on the designed plant

8.1.1. Section 1 (reaction between H_2S and H_2SO_4)

Section 1 includes the reaction between H_2S and H_2SO_4 in a series of Corning reactors, a decanter unit, and a high concentration evaporator. The reaction between hydrogen sulfide gas and excess sulfuric acid forms water, molten sulfur, and sulfur dioxide gas. As discussed earlier, this is the only reaction that makes the H_2S splitting cycle different from the sulfur-iodine water-splitting cycle. Operating conditions have been chosen to ensure complete conversion of all the hydrogen sulfide gas can occur [76-79]. Figure 8.2 illustrates a detailed process block diagram of the Section 1. The balanced reaction in the Section 1 can be seen as follows:

$$H_2S + H_2SO_4 \rightarrow 2H_2O + S + SO_2 \quad (8.1)$$

The molar ratio of sulfuric acid to hydrogen sulfide gas is required to be 15:1 to achieve complete conversion. The concentration of sulfuric acid enters the reactor at 96% (wt/wt) and leaves at 93% (wt/wt).

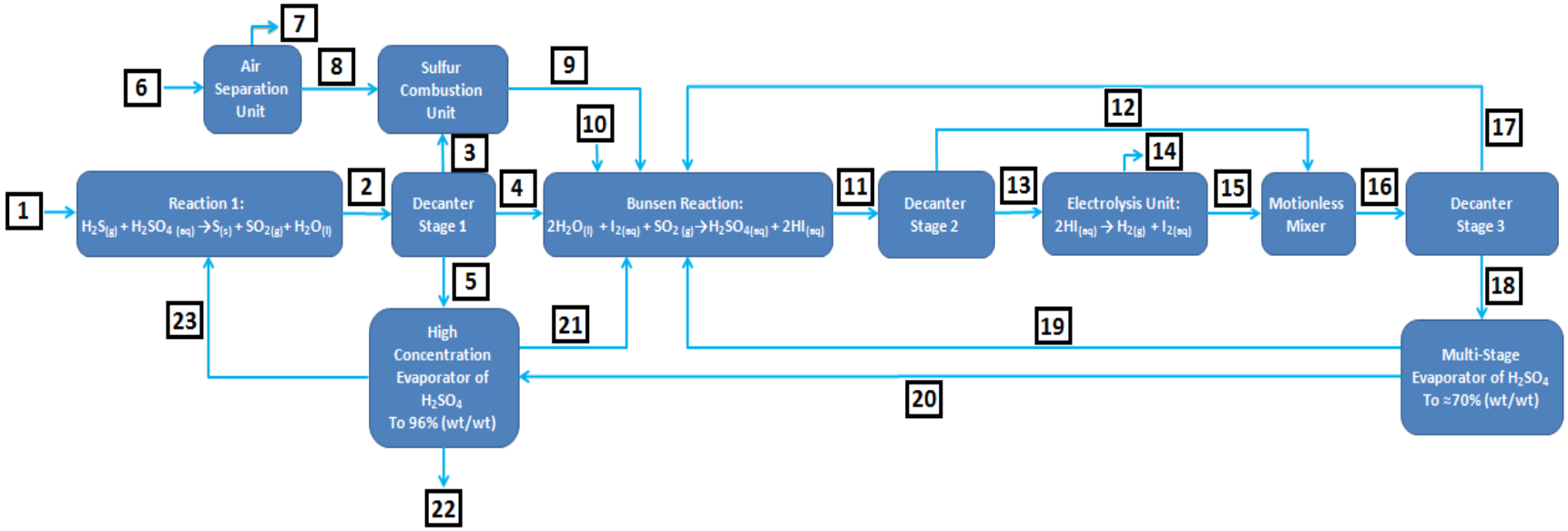

Fig 8.1. Process Block diagram of H_2S-H_2O splitting cycle to produce 51,000 tonnes/year of hydrogen (streams 1 to 23 contain: (1) hydrogen sulfide; (2) sulfuric acid, water, sulfur dioxide and elemental sulfur; (3) elemental sulfur; (4) sulfur dioxide; (5) sulfuric acid, water; (6) air; (7) nitrogen; (8) oxygen; (9) sulfur dioxide; (10) water; (11) sulfuric acid, water, iodine, toluene, hydroiodic acid; (12) iodine, toluene; (13) sulfuric acid, water, hydroiodic acid ; (14) hydrogen; (15) sulfuric acid, water, iodine; (16) sulfuric acid, water, iodine, toluene; (17) iodine, toluene; (18) sulfuric acid, water; (19) water; (20) sulfuric acid, water; (21) water; (22) sulfuric acid, water; (23) sulfuric acid, water)

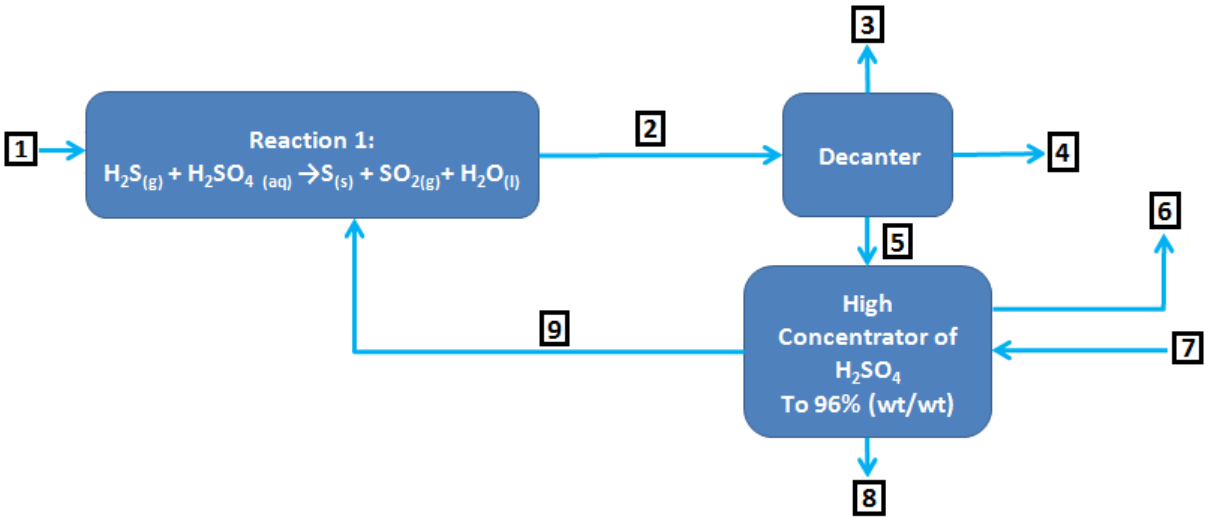

Fig 8.2. Process block diagram of the Section 1 of H_2S-H_2O splitting cycle

The reaction (8.1) operates at 150 ºC to ensure sulfur stays in molten form, which is critical to prevent the reactor from plugging. After the reaction is complete, the products are sent to a decanter unit to separate each phase. The auxiliary equipment used in the Section 1 consists of a decanter unit and a high concentration evaporator. In the decanter unit, sulfur dioxide gas exits through the top and flows into the Section 2. The molten sulfur settles out in the bottom of the unit and is sent to a combustion unit, which will be explained in more detail in the Section 2. A high concentration evaporator is used to concentrate the 93% (wt/wt) sulfuric acid from reaction (8.1) and 70% (wt/wt) from the Section 3 back up to 96% (wt/wt). This 96% (wt/wt) sulfuric acid is then recycled back into reaction (8.1), and the water removed from this unit is sent into reaction (8.2) in the Section 2.

8.1.2. Section 2 (the Bunsen reaction)

Section 2 consists of an air separation unit, sulfur combustion unit, and Corning reactors, which are used for the reaction (8.2). Figure 8.3 shows a detailed process block diagram of the Section 2. The Section 2 includes the Bunsen reaction, which is the most critical reaction of the hydrogen sulfide splitting cycle. Water, sulfur dioxide, and iodine react to form dilute sulfuric acid and hydroiodic acid in the water phase. The balanced Bunsen reaction in the Section 2 can be seen below:

$$2H_2O + SO_2 + I_2 \rightarrow H_2SO_4 + 2HI \qquad (8.2)$$

This reaction is composed of organic (I_2-toluene), aqueous (HI, H_2SO_4), and gaseous phases [17].

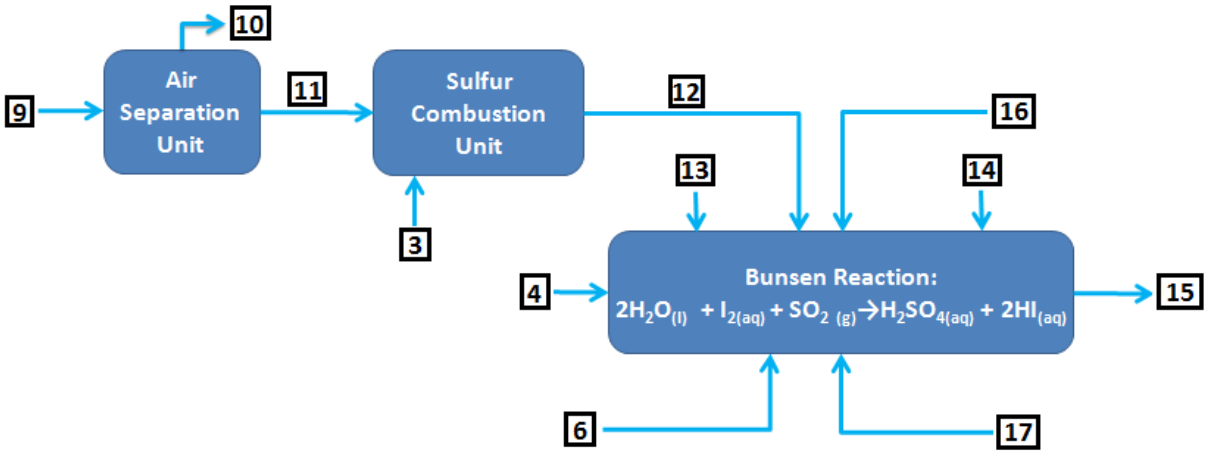

Fig 8.3. Process block diagram for the Section 2 of H_2S-H_2O splitting cycle

Corning reactors are used again to facilitate this reaction in order to guarantee a high degree of mixing and efficiency. Water is supplied from reaction (8.1), the evaporators, and a make-up stream to maintain the required amount. Excess water is required to achieve complete conversion of sulfur dioxide and to meet the 0.15 volumetric fraction obtained from lab data reported in the previous chapters. Sulfur dioxide is supplied from the reaction (8.1) and from a sulfur combustion unit. Toluene is used in the reaction (8.2) to dissolve the iodine so that the Bunsen reaction can be operated at ambient temperature. A ratio of 0.4 mole of iodine per liter of toluene is also used based on lab data to meet the reaction requirements.

A cryogenic air separator is used to produce pure oxygen, which is needed to guarantee a pure sulfur dioxide product entering the reaction (8.2) to avoid resistance in the gas phase. The benefit of using this separator is that it removes all the nitrogen before the oxygen enters the reaction, and reduces the amount of impurities in the process. A sulfur combustion unit takes in the pure oxygen supplied from the cryogenic air separator, and molten sulfur from the Section 1. The hydroiodic and sulfuric acids produced in the Bunsen reaction are sent to the Section 3 for hydrogen production.

8.1.3. Section 3 (HI decomposition)

This section includes two decanter units, an electrolysis unit, motionless mixers, and a multi-stage evaporator. Figure 8.4 shows the process block diagram of the Section 3. This section of the process is the hydrogen-producing stage via the electrolysis of hydroiodic acid. The balanced chemical equation for this reaction is described as follows:

$$2HI \rightarrow H_2 + I_2 \qquad (8.3)$$

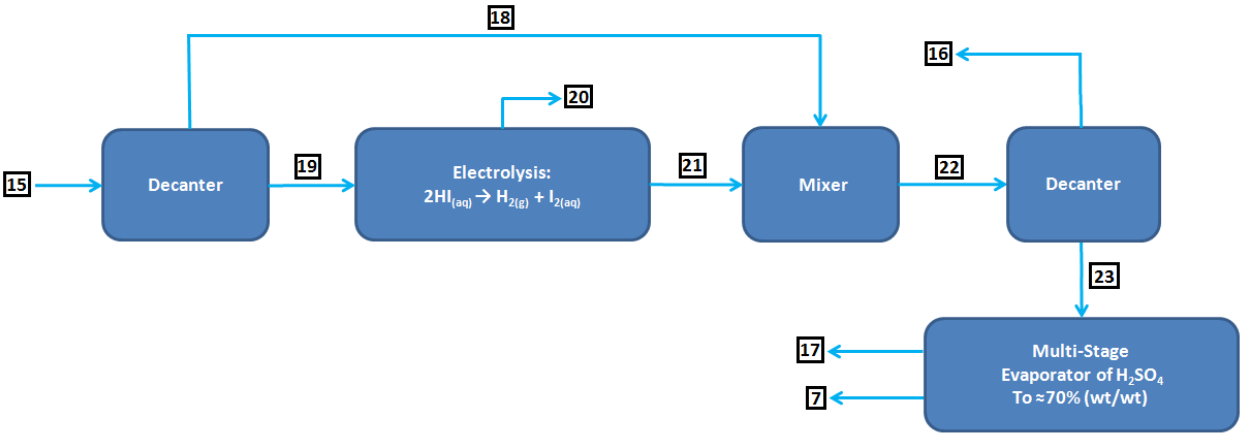

Fig 8.4. Process block diagram for the Section 3 of H_2S-H_2O splitting cycle

As previously discussed, this endothermic reaction (8.3) (300–450 ^{o}C) is believed to be the most challenging step of the thermochemical sulfur-iodine water-splitting cycle because of the presence of an azeotropic point in the HI_X mixture that prevents simple distillation. The extraction of HI from the HI_X mixture is also energy-demanding due to the high volume of water. The low equilibrium conversion (ca 20% at 400 ^{o}C) of this reaction is another concern [50]. Research into the characteristics of this reaction in Dr. Hui Wang's research group demonstrates that hydrogen can efficiently be produced from the electrolysis of hydroiodic acid at a constant voltage of 1.51 V at room temperature so that these technical challenges could be avoided [17].

Figure 8.4 shows the streams entering this section are the products from the Bunsen reaction. Therefore, the design of this section must also accommodate the flows of toluene and dilute sulfuric acid. Toluene is a poor conductor and quite flammable, so for process and safety considerations it bypasses the electrolysis unit and is re-mixed after electrolysis to dissolve the produced iodine. Sulfuric acid is a good conductor, and is used as the electrolyte for the reaction.

Decanters are used to remove the toluene before the electrolysis unit. Mixers introduce toluene back into the system and allow for iodine to be dissolved. The toluene, now containing iodine, needs to be separated again and recycled back to the Bunsen reaction. Another set of decanter units is used to carry out this separation. The aqueous phase leaving the second decanting stage consists of dilute sulfuric acid concentrated from 17% (wt/wt) to 70% (wt/wt) in a multi-stage evaporator. This stream is recycled to the Section 1 for further concentration in the high concentration evaporator. The overall flow rates of reactants and products of this process can be seen be in Table 8.1.

Table 8.1. Overall process flow rates of H_2S-H_2O splitting cycle

compound	flow rate (tonnes/year)	compound	flow rate (tonnes/year)
Inputs		Outputs	
H_2S	432,000	H_2	51,000
Air	1,675,000	H_2SO_4	1,243,000
H_2O	508,000	N_2	1,285,000
I_2	7,150		
C_7H_8	61,000		

8.2. Equipment sizing

The scale of this plant was designed to meet the hydrogen production needed for a typical heavy oil upgrader. The process was designed to handle several corrosive liquids such as sulfuric acid, hydroiodic acid and I_2-toluene solution. *Ulrich's A Guide to Chemical Engineering (Process Design and Economics)* [108] was used wherever possible to design equipment, but it does not cover every piece of equipment needed in the design. A Chemical Engineering Plant cost index value of 567 was used in this design [109]. The rest of the sizing of equipment was done in different ways including scaling-up from smaller processes, using Corning scaling-up capabilities, and applying existing facilities to calculate the size of equipment needed. The heat demand of the process was examined and heat was integrated wherever possible in the process. Detailed calculations are presented in Appendix D.

8.2.1. Section 1 (reaction between H_2S and H_2SO_4)

Section 1 has the largest heat demand of all three sections. This is due to the heat required to preheat the reactants of reaction (8.1), as well as to concentrate sulfuric acid. In order to resist the corrosion of sulfuric acid and hydrogen sulfide in the reaction 1, Corning reactors were selected to facilitate the reaction. To prevent corrosion, the decanters and evaporator are manufactured out of Alloy C-276, which is a nickel, molybdenum and chromium blend. The heat exchanger in the Section 1 also uses Alloy C-276 on the tube side and carbon steel on the shell side. The steam boiler and compressor are made of carbon steel because no acids are present.

The Corning reactors were sized by using experimental data performed in the LF-AFR. The reaction (8.1) is very fast and was found to have an approximate residence time of 2.5 seconds from lab data. Using this data, the number of G4 fluidic modules was determined to be 3,400. The decanters were designed as horizontal gravity decanters, where the different densities of sulfur and

sulfuric acid drive the separation of the products of reaction (8.1). In order to separate 1,300 m^3/hr of liquid, 16 decanters with a diameter of 4 m and length of 12 m are needed.

To provide the required amount of heat in this section, a steam boiler and compressor were implemented into the design. The energy required to generate 74,730 kg/hr of steam is 46.9 MW and the energy required to compress it from 1 bar to 20 bar is 20.9 MW. This steam is used to preheat the reactants, maintain the operating temperature of the reaction (8.1), and to concentrate the sulfuric acid recycling streams.

There are two types of sulfuric acid concentrators: high concentration and multi-stage. Multi-stage evaporators can only concentrate sulfuric acid up to 70 wt%. The combined sulfuric acid in the Section 1 is 89 wt/wt % so a high concentration evaporator was selected and designed as a forced-circulation evaporator. The amount of heat required for the evaporator was found by multiplying the mass flow rate of water that needed to be evaporated by the enthalpy of vaporization of water. The overall heat transfer coefficient was found in *Ulrich* to be 5,000 $J/s \cdot m^{2 \cdot} K$. Using this value and the energy input, the heat transfer area of the evaporator was determined to be 1,034 m^2.

A shell and tube heat exchanger is used to preheat the sulfuric acid going into the G4-Corning reactors. The amount of heat required was determined to be 252 MW using an Aspen HYSYS simulation. The corrected log mean temperature difference was calculated using the correction factor in *Ulrich*, which corresponds to the inlet and outlet temperature differences, R and S. The heat transfer area required for this heat exchanger was found to be 690 m^2 using the heat duty, corrected log mean temperature difference, and the overall heat transfer coefficient.

8.2.2. Section 2 (the Bunsen reaction)

The heat demand for the Section 2 was minimal due to running the Bunsen reaction at room temperature in the presence of toluene. Section 2 provides heat to the Section 1 from the sulfur combustion unit.

The cryogenic air separation unit, sulfur combustion unit, compressors and heat exchangers are made of carbon steel because there are no corrosive acids present. The carbon steel of the sulfur combustion unit will be lined with brick for insulation. G4-Corning reactors are used for the Bunsen reaction because of the corrosive acids and multiple phases present in the system.

The sulfur combustion unit requires a flow rate of 35,000 m^3/hr of oxygen at standard conditions. A cryogenic air separator was determined to be the best option to produce the large amount of pure oxygen needed for the sulfur combustion unit. The separation unit consists of a column, condenser, temperature swing absorption unit, turbine, compressor, and a multi-cell heat exchanger. However, the details and exact size of each piece of equipment are beyond the scope of this design.

The combustion unit has a sulfur flow rate of 25 m^3/hr. In order to reduce the size of the furnace, the oxygen stream is compressed to 10 bar using a multi-stage compressor. A total flow rate of 3,600 m^3/hr was calculated, as well as a residence time of 30 seconds, chosen from a range provided by *Ulrich*. This allowed the combustion unit to be sized as a direct-fired furnace with a diameter of 2.3 m and a height of 7.0 m.

Two stages of compressors are required to compress the oxygen from standard conditions to 10 bar. The compression ratio between stages is 3.14 and the fluid power of each compressor is 18.27 kW.

There is a large amount of heat produced from the sulfur combustion unit. This heat is used to concentrate the sulfuric acid in the multi-stage evaporator, and to subsidize the heat demand of

preheating the sulfuric acid in the Section 1. Through an Aspen HYSYS simulation, three shell and tube heat exchangers are used to collect 223 MW of heat from the combustion of sulfur. The heat transfer area of each heat exchanger is 743 m^2. This was found by the same method as the heat exchanger in the Section 1.

The Bunsen reaction sizing was done by scaling-up the flow of an LF-AFR 500 times to the flow rate of a G4 reactor. Table 8.2 shows this scale in detail.

By maintaining the same reaction characteristics determined experimentally, as discussed in the Section 1, it was found that 70,000 G4 fluidic modules are needed. The large number of fluidic modules is due to the small internal volume of each fluidic module and a high flow rate of 9,460 m^3/hr. High flow into the reactors is due to having excess reactants to achieve complete conversion, as well as excess toluene to dissolve iodine. A summary of the process requirements can be found in Table 8.3.

8.2.3. Section 3 (HI decomposition)

Section 3 consists of the electrolysis unit and auxiliary equipment to facilitate the toluene bypass, recycling to other sections, and the sulfuric acid concentration. Literature research provided information on corrosion-resistant materials and sizing the auxiliary components, while consultation with *ERCO Worldwide* provided information for the detailed design of the electrolysis unit. All equipment for this section must be constructed of corrosion-resistant material. Highly corrosive sulfuric and hydroiodic acids are present, which have the potential to damage equipment.

Table 8.2. Bunsen reaction lab data and scale-up of H_2S-H_2O splitting cycle

	reactor type		unit
	LF	G4	
reactor volume	0.5	250	mL
liquid flow rate	4.5	2,250	mL/min
H_2O volume fraction	0.15	0.15	
iodine concentration	0.4	0.4	mol/L toluene
gas flow rate	37	18,335	mL/min
SO_2 mole fraction (in N_2)	0.90	0.90	
SO_2 flow rate	33.6	16,669	mL/min
residence time	6.66	6.66	s

Table 8.3. Bunsen reaction process requirements of H_2S-H_2O splitting cycle

	process requirement	unit
iodine molar flow	3,216	kmol/hr
toluene flow rate	8,040	m^3/hr
water flow rate	1,420	m^3/hr
residence time	6.66	S
reactor volume	17.5	m^3
volume (G4-AFR)	250	mL
# G4-AFRs	70,000	fluidic modules

The material to be used for the decanters, mixers, and evaporators is Alloy C-276. For the electrolysis unit, titanium electrode plates were chosen because they are also corrosion-resistant. The sizing and costing of the electrolysis unit was completed with consultation from *ERCO Worldwide*. The design uses the same platinum electrode plates used in their chloralkali process, with the number of plates in parallel accommodating the required process flow. Information provided by *ERCO* included the plate throughput, cross-sectional area, and residence time. These values are seen in Table 8.4.

From these characteristics, the electrolysis unit was designed to accommodate the 1,760 m^3/h flow rate of sulfuric acid and hydroiodic acid. Due to the large flow rate of this process, 2,930 plates are to be configured in 10 units with each containing 293 plates in parallel. Each plate acts as an individual cell containing an anode and cathode, with hydrogen being produced on the surface of each plate.

Short-cut equipment design formulas found in *Ulrich* were used in the design of the auxiliary components for the Section 3. Decanters are used before and after the electrolysis unit to separate the aqueous and organic phases. In order to handle the high flow rate, 31 decanters are required on either side with each unit having a diameter of 4 m and a length of 12 m. They are designed as horizontal gravity decanters, where the different densities of toluene and sulfuric acid drive the separation process.

The iodine produced in the electrolysis unit must be properly mixed with toluene to achieve a high iodine recovery and recycle rate. To do this, five motionless mixers were chosen with a diameter of 0.58 m. These mixers are able to achieve good mixing characteristics between two-phase solutions. With the iodine from the electrolysis reaction being dissolved into the toluene, it can be recycled to the Bunsen reaction and lower the amount of make-up iodine required.

Table 8.4. Electrode plate information of H_2S-H_2O splitting cycle

material	titanium	unit
cross-sectional area	2.5	m^2
throughput rate	0.6	m^3/hr
residence time	15	minutes

To concentrate the dilute sulfuric acid following the second decanter stage, a multi-stage forced-circulation evaporator is used. It is capable of concentrating the sulfuric acid from 17% to 70% (wt/wt) where it can then be further concentrated in the Section 1 to 96% (wt/wt) and reused in reaction (8.1). The amount of heat required for the multi-stage evaporator was found by multiplying the mass flow rate of water that needed to be separated by the enthalpy of vaporization of water. The overall heat transfer coefficient was found in *Ulrich* to be 5,000 $W/m^{2\cdot}K$. Using this value and the energy input, the evaporator was determined to have a heat transfer area of 7,970 m^2.

The electricity required to electrolyze hydroiodic acid was calculated using *Faraday's law of electrolysis* [110]. Two moles of electrons are required to produce one mole of hydrogen, allowing for the current to be calculated. As mentioned earlier, conversion could be achieved with a constant voltage of 1.51 V. Based on this previous research, the current efficiency is 86% without toluene present in the reactor. The electricity requirements for the electrolysis unit are shown in Table 8.5. As seen from this table, the necessary current and power demands are very large. Due to the low molecular weight of hydrogen, the mass yield of hydrogen per mole of electrons transferred is very low, which results in large operating costs.

The only unit that requires the heat demand to be determined is the evaporator. Although electrolyzing hydroiodic acid is an endothermic reaction, it was assumed the heat generated from current inefficiencies would prove sufficient. For the evaporator, the energy required to concentrate the sulfuric acid was determined to be 797 MW. This heat duty is supplied from the steam boiler and heat recovered from other process vessels.

Table 8.5. Electrolysis unit requirements of H_2S-H_2O splitting cycle

characteristic	value	unit
current	180,400	kA
current density	24.6	kA/m^2
power demand	272	MW

8.3. Economic analysis

To assist in determining the feasibility of the process, an economic analysis was performed based on the designed plant in the previous sections as shown in Figure 8.5. Included in the analysis were fixed and working capital, operating expenses, and all product revenue. The fixed capital was determined to be approximately $4.9 billion. The total cost of each G4-Corning fluidic module was roughly $40,000, leading to the high capital cost. The operating expenses were approximately $1.5 billion/year. The main operating expenses included the cost of iodine and energy costs of the electrolysis and steam boiler.

This process has nitrogen and sulfuric acid byproducts which could be sold with the hydrogen. The total annual revenue was found to be approximately $2.1 billion. Assuming a 30 year plant life with a 14 day shutdown period per year, the discounted cash flow rate of return was found to be 6.4%. This rate of return is contingent on a minimum iodine recovery rate of 99.9% and the ability to sell all of the nitrogen produced. Detailed calculations are presented in Appendix D.

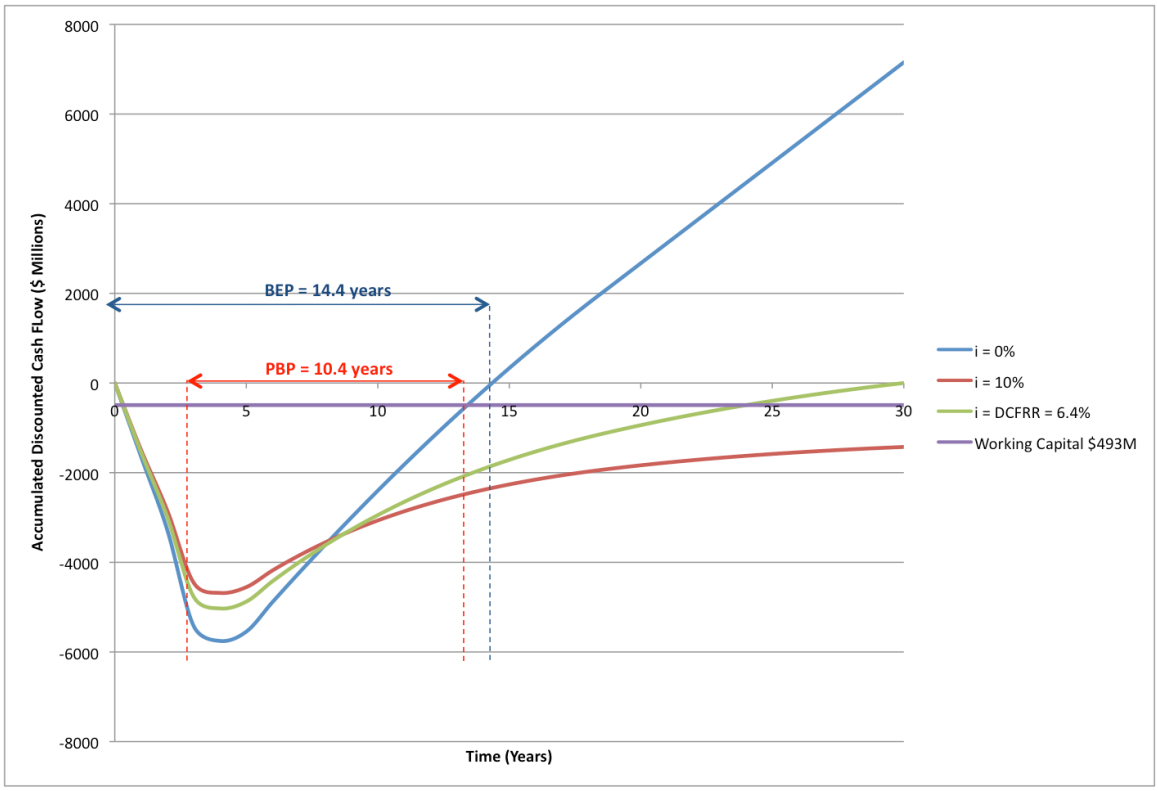

Fig 8.5. Plant Economics of H_2S-H_2O splitting cycle to produce 51,000 tonnes/year of hydrogen

8.4. Summary

H_2S-H_2O splitting cycles convert hydrogen sulfide from oil sands bitumen upgrading into valuable hydrogen. The design of this process was completed in three different sections:

In the Section 1, Corning reactors were selected to handle the first reaction between sulfuric acid and hydrogen sulfide gas because of their corrosion-resistance and mass transfer capabilities. A steam boiler was implemented into the design to manage the heat demand of the process. A heat exchanger is used in the Section 1 to transfer 252 MW of heat into the sulfuric acid before entering the Corning reactors. To separate the three phases produced in the reaction 1, 16 decanters are used. A high concentration forced-circulation evaporator is used to concentrate the sulfuric acid back to 96 wt% to be recycled into the first reaction. Both the evaporator and decanters are made of Alloy C-276 to prevent corrosion.

In the Section 2, a carbon steel air separation unit, capable of producing oxygen at 35,000 m^3/hr, was sized from scaling up a previously designed separation unit. A two-stage compressor is needed to compress the oxygen to 10 bar and reduce the size of the sulfur combustion unit. The sulfur combustion unit was designed as a direct-fired heater and is made out of carbon steel lined with brick for insulation. Three shell and tube heat exchangers are used to collect 223 MW of heat from the furnace's product stream. This heat is used to concentrate sulfuric acid and subsidize the heat demand in the Section 1. The Bunsen reaction is facilitated in 70,000 G4-Corning reactor fluidic modules because of the high flow rate and small internal volume of fluidic modules.

The design of the electrolysis unit and all auxiliary components was completed for the Section 3. Included in the design are the materials selected, sizes of each unit, and the electricity and heat demands. Challenges in this section included the large heat and electrical demands, and the low mass yield of hydrogen gas from electrolysis. Finally, an economic analysis was performed based on the designed plant.

CHAPTER NINE

CONCLUSIONS AND RECOMMENDATIONS

9.1. Summary and conclusions

1. Based on the inspiration of the S-I water-splitting cycle, the H_2S splitting cycle was developed in Dr. Hui Wang's research group. Chapter 3 shows the contributions of this thesis toward the previous works including a reaction scheme that was suggested for the multiphase Bunsen reaction as a key step of both the S-I water-splitting cycle and H_2S splitting cycle. It was found that a Bunsen reaction occurred when I_2 contacted a water-toluene interface. SO_2 showed to be significantly soluble in toluene making the reaction mechanism more complicated. The equilibrium constant was also calculated between I_2 and I^- species. It was found that the formation of higher poly-iodine and poly-iodide compounds was clearly possible at a higher I_2:HI molar ratio. According to the apparent reaction rate study of the Bunsen reaction in the gas-liquid-liquid multiphase system, the SO_2 dissolving-in-liquid phase proved to be the rate-controlling step.
2. The study of this H_2S splitting cycle also opened the gate to propose other attractive cycles that use sulfur-containing compounds as feedstock to feed the Bunsen reaction for hydrogen production. Therefore, five possible routes are proposed in Chapter 5. The performed calculations of molar destructed exergy for every single route show the inherent energy recovery potential of hydrogen production using different sulfur-containing feedstocks. Direct oxidation of H_2S had the most irreversibility while H_2 production using elemental sulfur as a feedstock was the potential alternative, depending on the customer's requirements.
3. In Chapter 6, the absorption rates of sulfur dioxide are measured for different combinations of the SO_2-water-toluene mixture in the LF-AFR and the G1-AFR including SO_2-water and SO_2-

toluene binary systems and the SO_2-water-toluene ternary system to identify the optimum operating conditions to be used when iodine is involved in the multiphase mixture. The overall mass transfer coefficients were also calculated for the binary systems. In the LF-AFR, the overall mass transfer coefficient values tended to be in the same order of magnitude as those for the G1-AFR once one fluidic module was used, indicating that the absorption in both reactors did not vary noticeably and the scaling-up had negligible effects from the LF-AFR to the G1-AFR.

4. In Chapter 7, the multiphase Bunsen reaction is conducted in the Corning-AFRs when SO_2 and I_2 are used as the limiting reactants in turn, and the effects of operating conditions on the rates of SO_2 and I_2 are studied. No significant enhancement for sulfur dioxide absorption was observed by the reaction. Increasing the temperature reduced the SO_2 absorption rate in liquid; however, this variation had no significant effect on the I_2 reaction rate in both reactors. Also, an increase in gas and liquid flow rates did not lead to a noticeable change in the iodine conversion in both reactors and the conversion of the iodine seems to have reached its equilibrium. By scaling-up twenty times, nearly similar data were obtained for both the LF-AFR and the G1-AFR indicating seamless scale-up for this reaction.
5. Chapter 8 illustrates a hydrogen production plant, designed to produce 51,000 tonnes/year of hydrogen, which is the amount needed for a typical heavy oil upgrader. The design process involved the comparison of different alternatives, the determination of flow rates for all required materials, scaling-up the lab data of reaction characteristics, and equipment sizing. An economic analysis was also performed at the end based on the designed plant.

9.2. Recommendations

1. Previously, each reaction in the H_2S splitting cycle has been studied separately. Our rigorous feasibility studies resulted in a low-temperature process for hydrogen production, however the integration of different sections has never been performed. Therefore, to reach the final goal of splitting the H_2S into hydrogen, it is recommended that all reactions be run together in a bench-scale facility so that a practical flow sheet can be developed based on the experimental results, including the reaction and purification steps.
2. The study of the H_2S splitting cycle led to proposals of other attractive cycles that use sulfur-containing compounds as feedstock to feed the Bunsen reaction for hydrogen production. Despite theoretical investigations, these routes have never been studied. Thus, we recommend the new SO_2 production routes be investigated experimentally, to be replaced with the first reaction of the H_2S splitting cycle (H_2S oxidation).
3. The first reaction of the H_2S splitting cycle, between H_2S and sulfuric acid, provides downgraded sulfuric acids, elemental sulfur and SO_2. Since this reaction was determined to be instantaneous, Corning® Advanced-Flow™ Reactors may not be the best choice. The economic analysis showed that choosing the G4-AFR for this process imposes a high capital cost. Therefore, a well-designed packed-bed reactor may be reconsidered for this section.
4. Despite the benefits from using toluene as the iodine solvent, which noticeably tackled the technical challenges in the Bunsen reaction, the circulation cost of the toluene may still cause a significant financial burden in terms of process optimization. We suggest using HI as the I_2 solvent so that a multiphase reaction can be avoided. Since it has larger solubility for I_2, therefore, the liquid flow rate could be reduced significantly while increasing the gas input, resulting in a higher reaction yield. The primary results of the Bunsen reaction, in the presence of hydroiodic acid as the solvent at the Corning Reactor Technology Center, show this proposal

is valid. However, lack of time prevented this experiment from being accomplished and it would make a valuable future study.

5. If HI solution is replaced with toluene, the excess quantities of iodine and water must be used, which results in conditions similar to the GA stoichiometry. Subsequently, the same conventional methods for hydrogen production in the Section 3 of the S-I water-splitting cycle, HI decomposition, must be used, as was explained in Chapter 2. We suggest an economic analysis would compare the costs of the two processes so that an informed decision could be made.
6. The design in Chapter 8 was performed based on the feasibility studies of each reaction separately. A more comprehensive design and economic analysis could be done after the integration of the three sections with the consideration of upgrading all units. Besides, the selection of some equipment and materials should be reconsidered in order to make the capital cost as low as possible.

LIST OF REFERENCES

[1] Holladay JD, Hu J, King DL, Wang Y. An overview of hydrogen production technologies. Catalysis Today. 2009;139:244-60.

[2] Levin DB, Chahine R. Challenges for renewable hydrogen production from biomass. International Journal of Hydrogen Energy. 2010;35:4962-9.

[3] Riis T, Hagen EF, Vie PJ, Ulleberg Ø. Hydrogen production–gaps and priorities. IEA Hydrogen Implementing Agreement (IEA, Paris, 2005). 2005.

[4] Brown LC, Besenbruch G, Lentsch R, Schultz KR, Funk JE, ATOMICS G. Alternative flowsheets for the sulfur-iodine thermochemical hydrogen cycle: United States. Department of Energy. Oakland Operations Office. 2003.

[5] E Funk J. Thermochemical hydrogen production: past and present. International Journal of Hydrogen Energy. 2001;26:185-90.

[6] Giaconia A, Caputo G, Ceroli A, Diamanti M, Barbarossa V, Tarquini P, et al. Experimental study of two phase separation in the Bunsen section of the sulfur–iodine thermochemical cycle. International Journal of Hydrogen Energy. 2007;32:531-6.

[7] Norman JH, Besenbruch GE, O'Keefe DR. Thermochemical Water-Splitting for Hydrogen Production, GRI-80/0105. Gas Research Institute. 1981.

[8] Sakurai M, Nakajima H, Onuki K, Shimizu S. Investigation of 2 liquid phase separation characteristics on the iodine–sulfur thermochemical hydrogen production process. International Journal of Hydrogen Energy. 2000;25:605-11.

[9] Sakurai M, Nakajima H, Amir R, Onuki K, Shimizu S. Experimental study on side-reaction occurrence condition in the iodine–sulfur thermochemical hydrogen production process. International Journal of Hydrogen Energy. 2000;25:613-9.

[10] De Beni G, Pierini G, Spelta B. The reaction of sulphur dioxide with water and a halogen. The case of iodine: reaction in presence of organic solvents. International Journal of Hydrogen Energy. 1980;5:141-9.

[11] Nomura M, Fujiwara S, Ikenoya K, Kasahara S, Nakajima H, Kubo S, et al. Application of an electrochemical membrane reactor to the thermochemical water splitting IS process for hydrogen production. Journal of Membrane Science. 2004;240:221-6.

[12] Nomura M, Nakao S-i, Okuda H, Fujiwara S, Kasahara S, Ikenoya K, et al. Development of an electrochemical cell for efficient hydrogen production through the IS process. AIChE Journal. 2004;50:1991-8.

[13] Sau S, Giaconia A, Caputo G, Prosini PP. Decrease the rate of recycling agents in the sulfur–iodine cycle by solid phase separation. International Journal of Hydrogen Energy. 2008;33:6439-44.

[14] Wang H. Hydrogen production from a chemical cycle of H_2S splitting. International Journal of Hydrogen Energy. 2007;32:3907-14.

[15] Rana MS, Sámano V, Ancheyta J, Diaz JAI. A review of recent advances on process technologies for upgrading of heavy oils and residua. Fuel. 2007;86:1216-31.

[16] ZareNezhad B. An investigation on the most important influencing parameters regarding the selection of the proper catalysts for Claus SRU converters. Journal of Industrial and Engineering Chemistry. 2009;15:143-7.

[17] Wang H, Le Person A, Zhao X, Li J, Nuncio P, Yang L, et al. A low-temperature hydrogen production process based on H_2S splitting cycle for sustainable oil sands bitumen upgrading. Fuel Processing Technology. 2013;108:55-62.

[18] Nieves Remacha MJ, Kulkarni AA, Jensen KF. Gas-Liquid Flow and Mass Transfer in an Advanced Flow Reactor. Industrial & Engineering Chemistry Research. 2013.

[19] Lavric ED, Woehl P. Advanced-Flow™ glass reactors for seamless scaleup. Chemistry Today. 2009;27:45-8.

[20] Chivilikhinl MS, Kuandykovl L, Lavric ED, Federation R, Avon F. Residence Time Distribution in Corning® Advanced-Flow™ Reactors. Experiment and Modelling. Chemical Engineering Transactions. 2011;25:791-6.

[21] Lavric ED. Thermal performance of Corning glass microstructures. Proceedings of the Heat Transfer and Fluid Flow in Microscale III Conference, Hilton Whistler, BC, Canada, ECI international. 2008.

[22] Verfondern K. Hydrogen Production Using Nuclear Energy. 2013.

[23] De Beni G, Marchetti C. Hydrogen, key to the energy market. Eurospectra. 1970;9:46.

[24] Knoche KF, Cremer H, Steinborn G, Schneider W. Feasibility studies of chemical reactions for thermochemical water splitting cycles of the iron-chlorine, iron-sulfur and manganese-sulfur families. International Journal of Hydrogen Energy. 1977;2:269-89.

[25] Kubo S, Nakajima H, Kasahara S, Higashi S, Masaki T, Abe H, et al. A demonstration study on a closed-cycle hydrogen production by the thermochemical water-splitting iodine–sulfur process. Nuclear Engineering and Design. 2004;233:347-54.

[26] Buckingham R RB, Moore R, Pickard P, Helie M, Carles P. Status of the INERI sulfure iodine integrated loop experiment. Proc 17th world hydrogen energy conference. Brisbane, Australia. 2008.

[27] Chang J LW. Status of the Korean nuclear hydrogen production project. The fourth information exchange meeting of nuclear production of hydrogen. Oakbrook, Illinois, USA. 2009; 59-66.

[28] Zhang P, Chen SZ, Wang LJ, Yao TY, Xu JM. Study on a lab-scale hydrogen production by closed cycle thermo-chemical iodine–sulfur process. International Journal of Hydrogen Energy. 2010;35:10166-72.

[29] Liberatore R, Caputo G, Ceroli A, Felici C, Giaconia A, Favuzza P. Demonstration of hydrogen production by sulphur–iodine cycle: realization of a 10 NL/h plant. 18th world hydrogen energy conference. 2010;16-21.

[30] Giaconia A, Caputo G, Sau S, Prosini PP, Pozio A, De Francesco M, et al. Survey of Bunsen reaction routes to improve the sulfur–iodine thermochemical water-splitting cycle. International Journal of Hydrogen Energy. 2009;34:4041-8.

[31] Parisi M, Giaconia A, Sau S, Spadoni A, Caputo G, Tarquini P. Bunsen reaction and hydriodic phase purification in the sulfur–iodine process: An experimental investigation. International Journal of Hydrogen Energy. 2011;36:2007-13.

[32] Taylor ML, Elder RH, Styring P, Allen RWK. Improved solvation routes for the Bunsen reaction in the sulphur iodine thermochemical cycle: Part I – Ionic liquids. International Journal of Hydrogen Energy. 2013;38:1765-74.

[33] Norman J, Besenbruch G, Brown L, O'keefe D, Allen C. Thermochemical water-splitting cycle, bench-scale investigations, and process engineering. GA-A16713. 1982.

[34] Liberatore R, Lanchi M, Giaconia A, Tarquini P. Energy and economic assessment of an industrial plant for the hydrogen production by water-splitting through the sulfur-iodine thermochemical cycle powered by concentrated solar energy. International Journal of Hydrogen Energy. 2012;37:9550-65.

[35] Leybros J, Gilardi T, Saturnin A, Mansilla C, Carles P. Plant sizing and evaluation of hydrogen production costs from advanced processes coupled to a nuclear heat source. Part I: Sulphur–iodine cycle. International Journal of Hydrogen Energy. 2010;35:1008-18.

[36] Lee BJ, Cheon No H, Joon Yoon H, Jun Kim S, Soo Kim E. An optimal operating window for the Bunsen process in the I–S thermochemical cycle. International Journal of Hydrogen Energy. 2008;33:2200-10.

[37] Calabrese VT, Khan A. Polyiodine and Polyiodide Species in an Aqueous Solution of Iodine + KI: Theoretical and Experimental Studies. The Journal of Physical Chemistry A. 2000;104:1287-92.

[38] Spadoni A, Falconieri M, Lanchi M, Liberatore R, Marrocco M, Sau GS, et al. Iodine compounds speciation in HI–I2 aqueous solutions by Raman spectroscopy. International Journal of Hydrogen Energy. 2012;37:1326-34.

[39] Colette Maatouk S, Brijou Mokrani N, Tabarant M, Fleche J-L, Carles P. Study of the miscibility gap in H_2SO_4/HI/I_2/H_2O mixtures produced by the Bunsen reaction – Part I: Preliminary results at 308 K. International Journal of Hydrogen Energy. 2009;34:7155-61.

[40] Guo HF, Zhang P, Bai Y, Wang LJ, Chen SZ, Xu JM. Continuous purification of H_2SO_4 and HI phases by packed column in IS process. International Journal of Hydrogen Energy. 2010;35:2836-9.

[41] Zhu Q, Zhang Y, Zhou C, Wang Z, Zhou J, Cen K. Optimization of liquid–liquid phase separation characteristics in the Bunsen section of the sulfur–iodine hydrogen production process. International Journal of Hydrogen Energy. 2012;37:6407-14.

[42] Elder RH, Priestman GH, Allen RWK, Orme CJ, Stewart FF. The feasibility of membrane separations in the HIx processing section of the sulphur iodine thermochemical cycle. International Journal of Hydrogen Energy. 2009;34:6614-24.

[43] Taylor ML, Elder RH, Allen RWK. Improved solvation routes for the Bunsen reaction in the sulphur iodine thermochemical cycle: Part II – Molecular solvent properties. International Journal of Hydrogen Energy. 2013;38:1775-83.

[44] Taylor ML, Elder RH, Allen RWK. Improved solvation routes for the Bunsen reaction in the sulphur iodine thermochemical cycle: Part III–Bunsen reaction in molecular solvents. International Journal of Hydrogen Energy. 2013;38:1784-94.

[45] Barbarossa V, Vanga G, Diamanti M, Calí M, Doddi G. Chemically Enhanced Separation of H_2S0_4/HI Mixtures from the Bunsen Reaction in the Sulfur−Iodine Thermochemical Cycle. Industrial & Engineering Chemistry Research. 2009;48:9040-4.

[46] AuYeung NJ. Hydrogen production via a sulfur-sulfur thermochemical water-splitting cycle, PhD Thesis. 2011.

[47] Immanuel V, Gokul KU, Shukla A. Membrane electrolysis of Bunsen reaction in the iodine–sulphur process for hydrogen production. International Journal of Hydrogen Energy. 2012;37:3595-601.

[48] Immanuel V, Shukla A. Effect of operating variables on performance of membrane electrolysis cell for carrying out Bunsen reaction of I–S cycle. International Journal of Hydrogen Energy. 2012;37:4829-42.

[49] Gokul KU, Immanuel V, Sant S, Shukla A. Membrane electrolysis for Bunsen reaction of the SI cycle. Journal of Membrane Science. 2011;380:13-20.

[50] Vitart X, Carles P, Anzieu P. A general survey of the potential and the main issues associated with the sulfur–iodine thermochemical cycle for hydrogen production using nuclear heat. Progress in Nuclear Energy. 2008;50:402-10.

[51] Roth M, Knoche K. Thermochemical water splitting through direct Hi-decomposition from $H_2O/HI/I_2$ solutions. International journal of hydrogen energy. 1989;14:545-9.

[52] Zhang Y, Wang Z, Zhou J, Liu J, Cen K. Experimental study of Ni/CeO_2 catalytic properties and performance for hydrogen production in sulfur–iodine cycle. International Journal of Hydrogen Energy. 2009;34:5637-44.

[53] Hinshelwood CN, Burk RE. CCCCII.-The relation of homogeneous to catalysed reactions. The catalytic decomposition of hydrogen iodide on the surface of platinum. Journal of the Chemical Society, Transactions. 1925;127:2896-900.

[54] Chen Y, Wang Z, Zhang Y, Zhou J, Cen K. Platinum–ceria–zirconia catalysts for hydrogen production in sulfur-iodine cycle. International Journal of Hydrogen Energy. 2010;35:445-51.

[55] Favuzza P, Felici C, Lanchi M, Liberatore R, Mazzocchia CV, Spadoni A, et al. Decomposition of hydrogen iodide in the S–I thermochemical cycle over Ni catalyst systems. International Journal of Hydrogen Energy. 2009;34:4049-56.

[56] Li D, Wang L, Zhang P, Chen S, Xu J. HI decomposition over active carbon supported binary Ni–Pd catalysts prepared by electroless plating. Catalysis Communications. 2013;37:32-5.

[57] Li D, Wang L, Zhang P, Chen S, Xu J. Effects of the composition on the active carbon supported Pd–Pt bimetallic catalysts for HI decomposition in the iodine–sulfur cycle. International Journal of Hydrogen Energy. 2013;38:6586-92.

[58] Lin X, Zhang Y, Wang Z, Wang R, Zhou J, Cen K. Hydrogen production by HI decomposition over nickel–ceria–zirconia catalysts via the sulfur–iodine thermochemical water-splitting cycle. Energy Conversion and Management. 2014;84:664-70.

[59] Petkovic LM, Ginosar DM, Rollins HW, Burch KC, Deiana C, Silva HS, et al. Activated carbon catalysts for the production of hydrogen via the sulfur–iodine thermochemical water splitting cycle. International Journal of Hydrogen Energy. 2009;34:4057-64.

[60] Wang L, Bai S, Wang Z, Zhao Y, Yuan X, Zhang P, et al. Activity and stability of Pt catalysts supported on carbon nanotubes, active carbon and γ-Al_2O_3 for HI decomposition in iodine–sulfur thermochemical cycle. International Journal of Hydrogen Energy. 2012;37:10020-7.

[61] Wang L, Han Q, Hu S, Li D, Zhang P, Chen S, et al. Influence of Ir content on the activity of Pt-Ir/C catalysts for hydrogen iodide decomposition in iodine–sulfur cycle. Applied Catalysis B: Environmental. 2015;164:128-34.

[62] Wang L, Han Q, Li D, Wang Z, Chen J, Chen S, et al. Comparisons of Pt catalysts supported on active carbon, carbon molecular sieve, carbon nanotubes and graphite for HI decomposition at different temperature. International Journal of Hydrogen Energy. 2013;38:109-16.

[63] Wang L, Hu S, Li D, Han Q, Zhang P, Chen S, et al. Effects of the second metals on the active carbon supported Pt catalysts for HI decomposition in the iodine–sulfur cycle. International Journal of Hydrogen Energy. 2014;39:14161-5.

[64] Wang L, Zhang P, Chen S, Xu J. Overview of the development of catalysts for HI decomposition in the iodine–sulfur thermochemical cycle at INET. Nuclear Engineering and Design. 2014;271:60-3.

[65] Wang ZC, Wang LJ, Zhang P, Chen SZ, Xu JM, Chen J. Effect of preparation methods on Pt/alumina catalysts for the hydrogen iodide catalytic decomposition. Chinese Chemical Letters. 2009;20:102-5.

[66] Zhang Y, Wang R, Lin X, Wang Z, Liu J, Zhou J, et al. Catalytic performance of different carbon materials for hydrogen production in sulfur–iodine thermochemical cycle. Applied Catalysis B: Environmental. 2015;166–167:413-22.

[67] Tyagi D, Scholz K, Varma S, Bhattacharya K, Mali S, Patil PS, et al. Development of Pt-Carbon catalysts using MCM-41 template for HI decomposition reaction in S–I thermochemical cycle. International Journal of Hydrogen Energy. 2012;37:3602-11.

[68] Onuki K, Hwang G-J, Arifal, Shimizu S. Electro-electrodialysis of hydriodic acid in the presence of iodine at elevated temperature. Journal of Membrane Science. 2001;192:193-9.

[69] Onuki K, Hwang G-J, Shimizu S. Electrodialysis of hydriodic acid in the presence of iodine. Journal of Membrane Science. 2000;175:171-9.

[70] Hwang G-J, Onuki K, Nomura M, Kasahara S, Kim J-W. Improvement of the thermochemical water-splitting IS (iodine–sulfur) process by electro-electrodialysis. Journal of Membrane Science. 2003;220:129-36.

[71] Banerjee AM, Shirole AR, Pai MR, Tripathi AK, Bharadwaj SR, Das D, et al. Catalytic activities of Fe_2O_3 and chromium doped Fe_2O_3 for sulfuric acid decomposition reaction in an integrated boiler, preheater, and catalytic decomposer. Applied Catalysis B: Environmental. 2012;127:36-46.

[72] Lee SY, Jung H, Kim WJ, Shul YG, Jung K-D. Sulfuric acid decomposition on Pt/SiC-coated-alumina catalysts for SI cycle hydrogen production. International Journal of Hydrogen Energy. 2013;38:6205-9.

[73] Tagawa H, Endo T. Catalytic decomposition of sulfuric acid using metal oxides as the oxygen generating reaction in thermochemical water splitting process. International Journal of Hydrogen Energy. 1989;14:11-7.

[74] Yu G, Wang H, Chuang KT. Upper Bound for the Efficiency of a Novel Chemical Cycle of H2S Splitting for H_2 Production. Energy & Fuels. 2009;23:2184-91.

[75] Goldstein S, Borgard J-M, Vitart X. Upper bound and best estimate of the efficiency of the iodine sulphur cycle. International Journal of Hydrogen Energy. 2005;30:619-26.

[76] Wang H, Dalla IG, Chuang L, Chuang KT. Thermodynamics and Stoichiometry of Reactions between Hydrogen Sulfide and Concentrated Sulfuric Acid. The Canadian Journal of Chemical Engineering. 2003;81:80-5.

[77] Wang H, Dalla Lana IG, Chuang KT. Kinetics and Mechanism of Oxidation of Hydrogen Sulfide by Concentrated Sulfuric Acid. Industrial & Engineering Chemistry Research. 2002;41:6656-62.

[78] Wang H, Dalla Lana IG, Chuang KT. Kinetics of Reaction between Hydrogen Sulfide and Sulfur Dioxide in Sulfuric Acid Solutions. Industrial & Engineering Chemistry Research. 2002;41:4707-13.

[79] Wang H, Dalla Lana IG, Chuang KT. Mass-Transfer Characteristics for Gas−Liquid Reaction of H_2S and Sulfuric Acid in a Packed Column. Industrial & Engineering Chemistry Research. 2004;43:5846-53.

[80] Zhang Q, Dalla Lana IG, Chuang KT, Wang H. Reactions between Hydrogen Sulfide and Sulfuric Acid: A Novel Process for Sulfur Removal and Recovery. Industrial & Engineering Chemistry Research. 2000;39:2505-9.

[81] Onda K, Takeuchi H, Okumoto Y. Mass transfer coefficients between gas and liquid phases in packed columns. Journal of Chemical Engineering of Japan. 1968;1:56-62.

[82] Yang L. The Bunsen reaction in the presence of organic solvent in H_2S splitting cycle: MSc. thesis, University of Saskatchewan. 2010.

[83] Makitra R, Kal'muk S, Bryk D, Polyuzhin I. Factors controlling sulfur dioxide solubilities in organic solvents. Russian journal of inorganic chemistry. 2010;55:1322-9.

[84] Li J, Moniri A, Wang H. Apparent kinetics of a gas–liquid–liquid system of Bunsen reaction with iodine-toluene solution for hydrogen production through H_2S splitting cycle. International Journal of Hydrogen Energy. 2015;40:2912-20.

[85] Nieves-Remacha MJ, Kulkarni AA, Jensen KF. Gas–Liquid Flow and Mass Transfer in an Advanced-Flow Reactor. Industrial & Engineering Chemistry Research. 2013;52:8996-9010.

[86] Braune S, Pöchlauer P, Reintjens R, Steinhofer S, Winter M, Lobet O, et al. Selective nitration in a microreactor for pharmaceutical production under cGMP conditions. Chemistry Today. 2009;27:26-9.

[87] National Institute of Standards and Technology (NIST).

[88] Grob RL, Barry EF. Modern practice of gas chromatography: John Wiley & Sons. 2004.

[89] P.D. C. Sulfur and hydrogen sulphide recovery. Kirk-Othmer encyclopaedia of chemical technology: John Wiley & Sons Inc.. 2001.

[90] T.L. M. Sulfuric acid and sulfur trioxide. Kirk-Othmer encyclopaedia of chemical technology: John Wiley & Sons Inc.; 2007.

[91] Prietzel J, Mayer B, Legge AH. Cumulative impact of 40 years of industrial sulfur emissions on a forest soil in west-central Alberta (Canada). Environmental Pollution. 2004;132:129-44.

[92] Querido R, Short WL. Removal of sulfur dioxide from stack gases by catalytic reduction to elemental sulfur with carbon monoxide. Industrial & Engineering Chemistry Process Design and Development. 1973;12:10-8.

[93] Tang Z-g, Zhou C-c, Chen C. Studies on flue gas desulfurization by chemical absorption using an ethylenediamine-phosphoric acid solution. Industrial & engineering chemistry research. 2004;43:6714-22.

[94] Karatepe N. A comparison of flue gas desulfurization processes. Energy Sources. 2000;22:197-206.

[95] Brady JD. Flue gas scrubbing process for sulfur dioxide and particulate emissions preceding CO_2 absorption. Environmental progress. 1987;6:9-12.

[96] Spector ML, Brian TP. Removal of sulfur oxides from stack gas. US Patent 3,843,789. 1974.

[97] Moran M.J. SHN. Fundamentals of Engineering Thermodynamics. 6th edition: Wiley. 2008.

[98] Sankaranarayanan K, de Swaan Arons J, van der Kooi HJ. Efficiency and Sustainability in the energy and chemical industries: scientific principles and case studies: CRC Press. 2004.

[99] Vundela Siva R, Subash Chndra K, Sudhir Kumar T, Narayanlal P. An approach to analyse energy and exergy analysis of thermal power plants: a review. Smart Grid and Renewable Energy. 2010.

[100] Sayin C, Hosoz M, Canakci M, Kilicaslan I. Energy and exergy analyses of a gasoline engine. International journal of energy research. 2007;31:259-73.

[101] National Institute of Standards and Technology (NIST). http://webbook.nist.gov/chemistry/. 2005.

[102] Bilgen S. Calculation and interpretation of the standard chemical exergies of elements using the chemical reference species. Acta Physico-Chimica Sinica. 2009;25:1645-9.

[103] Orhan MF, Dincer I, Rosen MA. Design of systems for hydrogen production based on the Cu–Cl thermochemical water decomposition cycle: configurations and performance. International Journal of Hydrogen Energy. 2011;36:11309-20.

[104] Cengel Y. A. BMA. Thermodynamics An Engineering Approach. 5th Edition ed: McGraw-Hill Science. 2005.

[105] Levenspiel O. Chemical reaction engineering. Industrial & Engineering Chemistry Research. 1999;38:4140-3.

[106] Brilman DWF. Mass transfer and chemical reaction in gas-liquid-liquid systems: Universiteit Twente. 1998.

[107] Zhu Q, Zhang Y, Ying Z, Wang S, Wang Z, Zhou J, et al. Kinetic and thermodynamic studies of the Bunsen reaction in the sulfur–iodine thermochemical process. International Journal of Hydrogen Energy. 2013;38:8617-24.

[108] Ulrich GD. A guide to chemical engineering process design and economics. 1984.

[109] www.ihs.com/products/global-insight/. 2013.

[110] Ehl, Rosemary Gene. Faraday's Laws in One Equation. Journal of Chemical Education. 1954;31:226-32.

APPENDICES

In this section all calibration data are presented. Appendix A shows the mass flow controllers and pump calibration data. In Appendix B calibration curves for liquid phase analyses are given while in Appendix C, the procedure for gas phase calibration is described. Finally, detailed calculation for plant designs and economic are clarified in Appendix D. All the raw data and processing results have been copied to a CD, which is attached to this thesis when it is finalized.

APPENDIX A

MASS FLOW CONTROLLERS AND PUMPS CALIBRATION DATA

Figures A1 to A4 show the MFC calibration curves of N_2 and SO_2, in the Low Flow and G1 Corning® Advanced-Flow™ Reactors, respectively while Figures A5 to A8 show the calibration curves for the pumps used for these reactors as well.

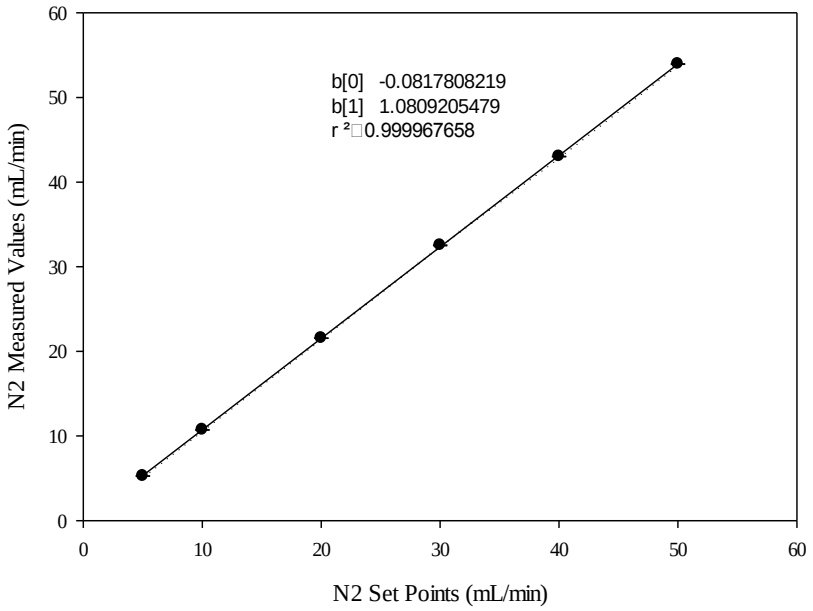

Fig A1. Nitrogen calibration curve for MKS mass flow controller (LF-AFR); error bars are standard deviations

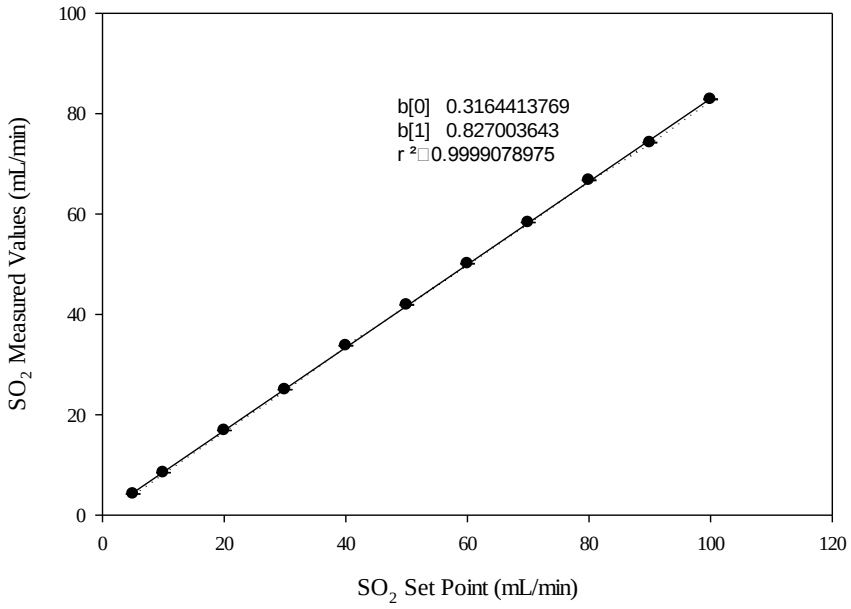

Fig A2. Sulfur dioxide calibration curve for MKS mass flow controller (LF-AFR); error bars are standard deviations

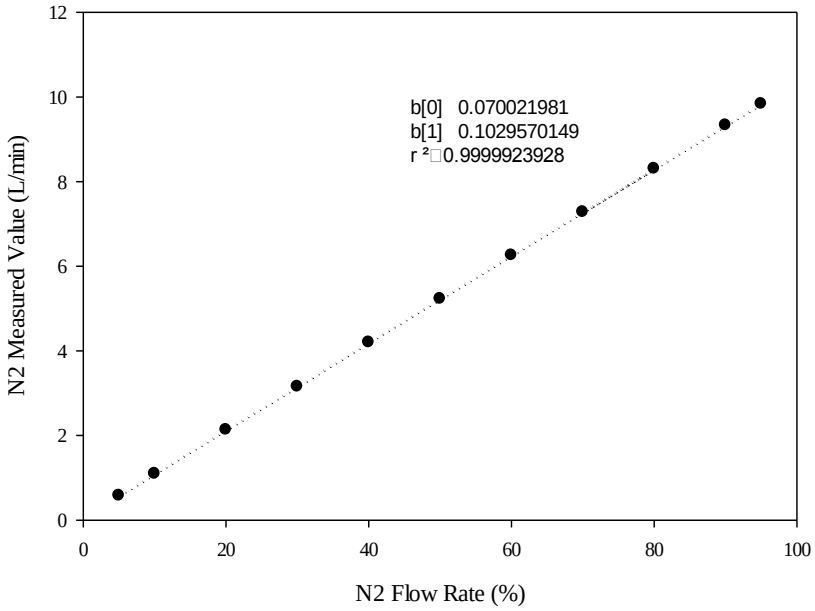

Fig A3. Nitrogen calibration curve for Brooks mass flow controller (G1-AFR); error bars are standard deviations

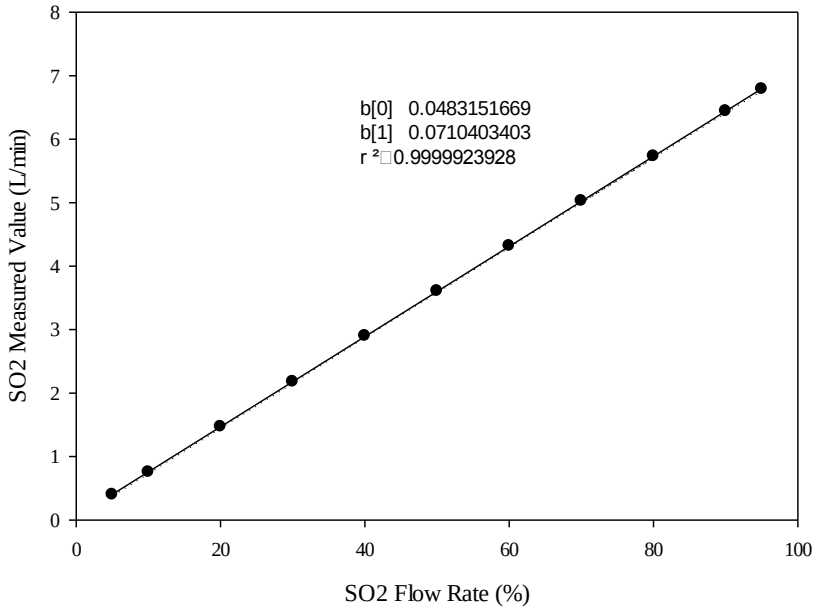

Fig A4. Sulfur dioxide calibration curve for Brooks mass flow controller (G1-AFR); error bars are standard deviations

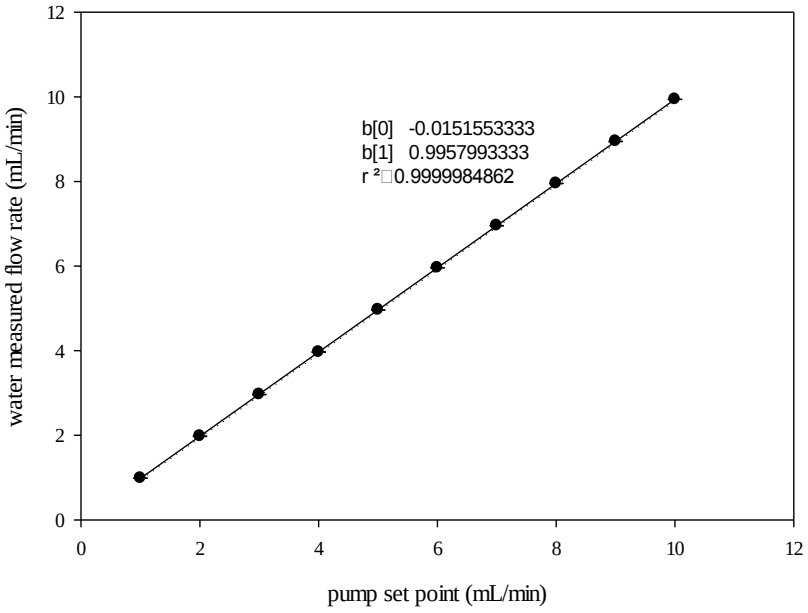

Fig A5. Water pump calibration curve for KD Scientific syringe pump (LF-AFR); error bars are standard deviations

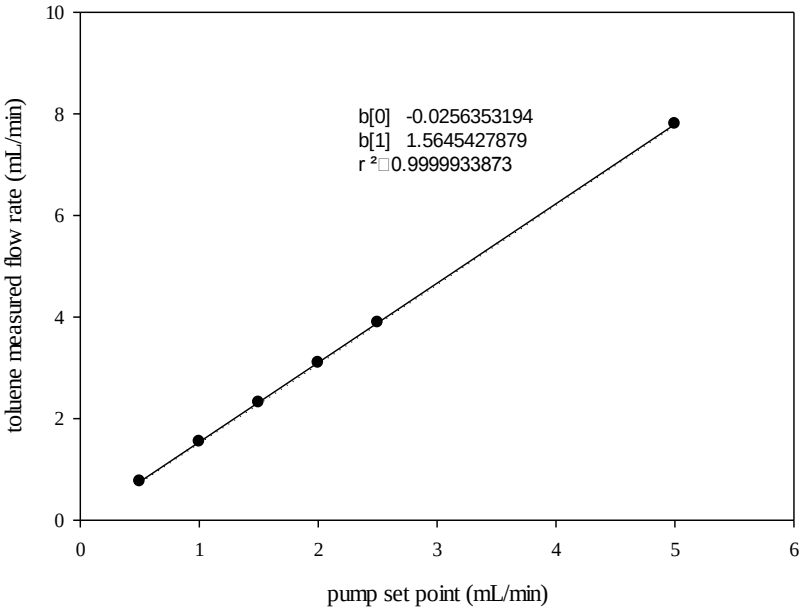

Fig A6. Toluene pump calibration curve for KD Scientific syringe pump (LF-AFR); error bars are standard deviations

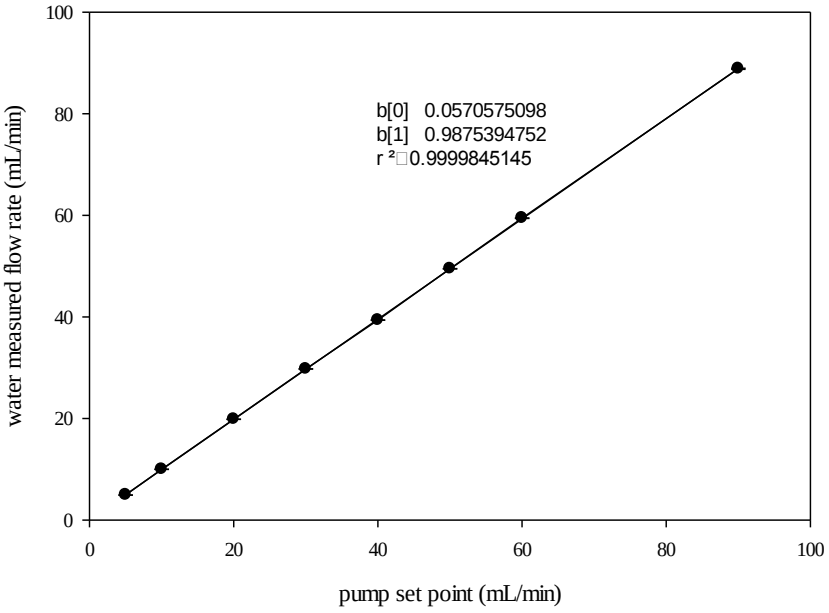

Fig A7. Water pump calibration curve for Jiangsu Hanbon Science & Technology pump (G1-AFR); error bars are standard deviations

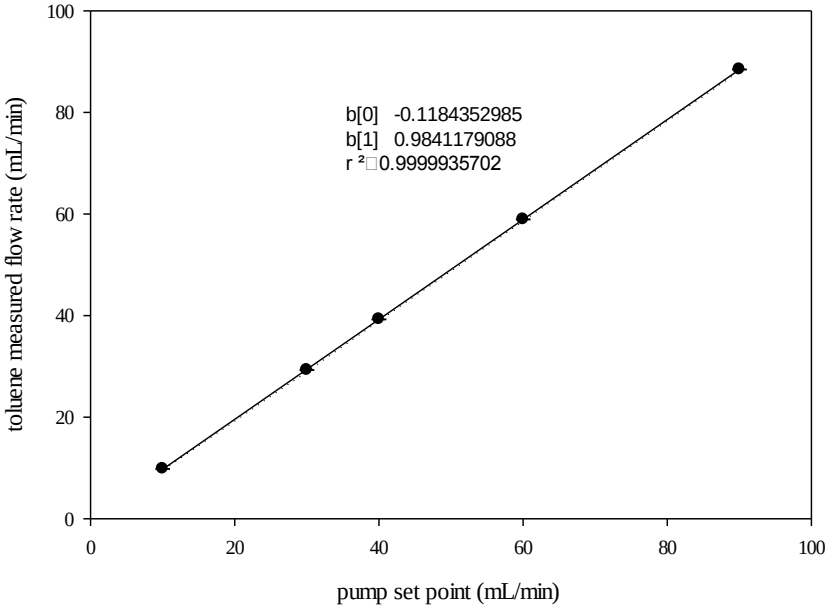

Fig A8. Toluene pump calibration curve for Fuji Technic Tokyo pump (G1-AFR); error bars are standard deviations

APPENDIX B

CALIBRATION CURVE DATA FOR LIQUID PHASE ANALYSES

Figures B1 to B4 show the calibration curves of iodide and iodine, for the Low Flow and G1 Corning® Advanced-Flow™ Reactors.

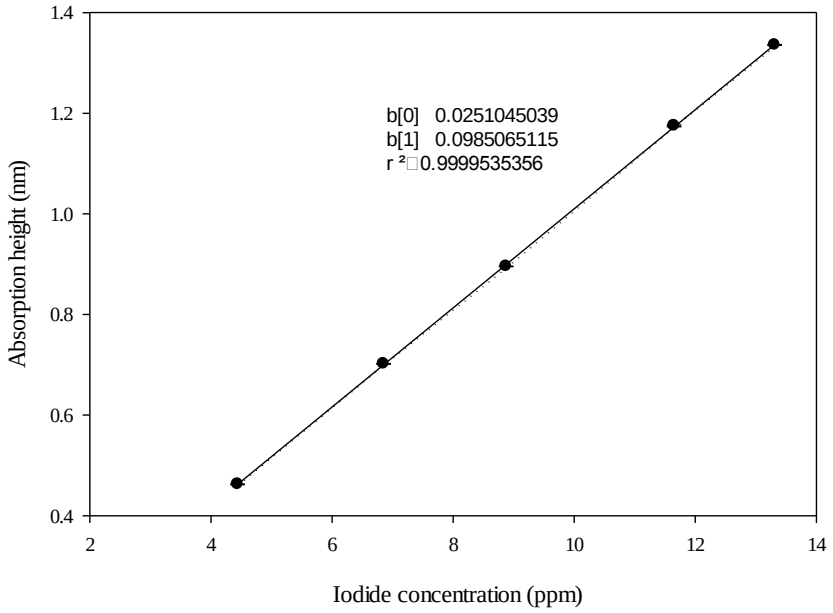

Fig B1. Iodide calibration curve for the LF-AFR; error bars are standard deviations

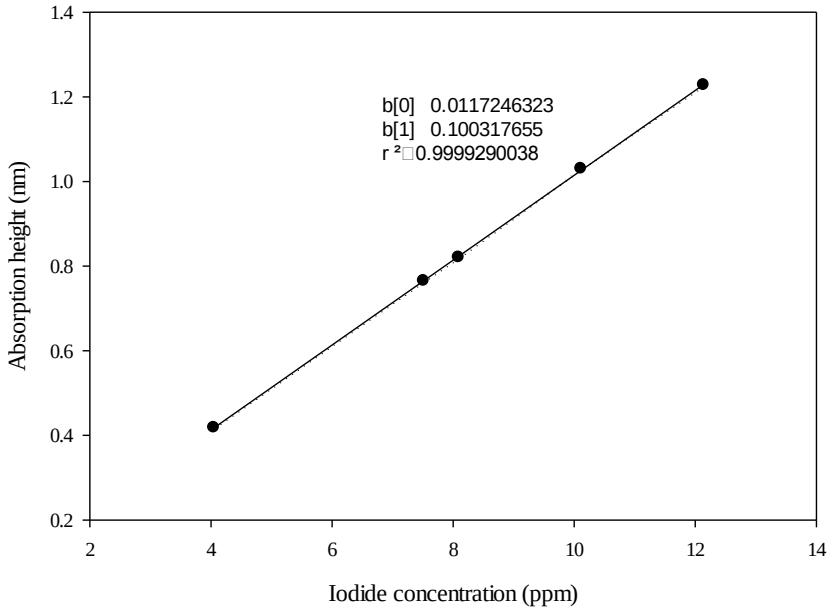

Fig B2. Iodide calibration curve for the G1-AFR; error bars are standard deviations

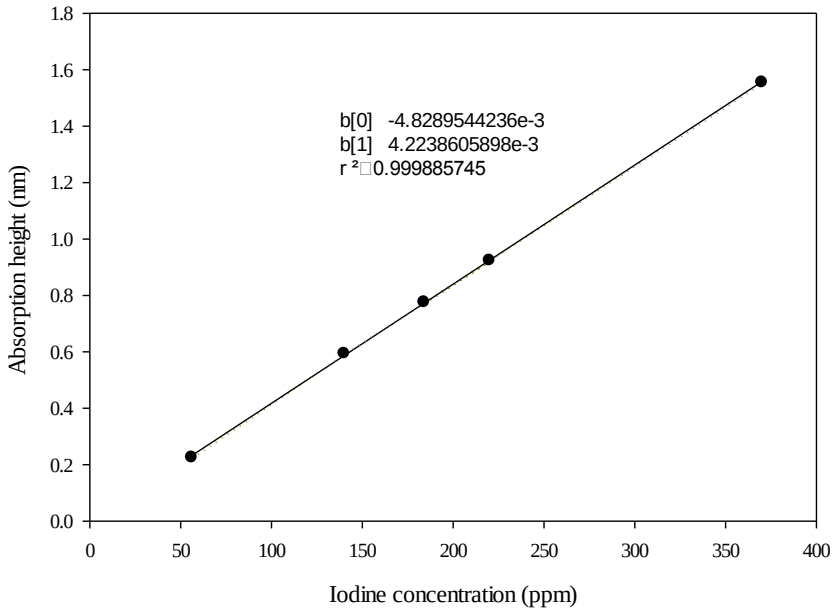

Fig B3. Iodine calibration curve for the LF-AFR; error bars are standard deviations

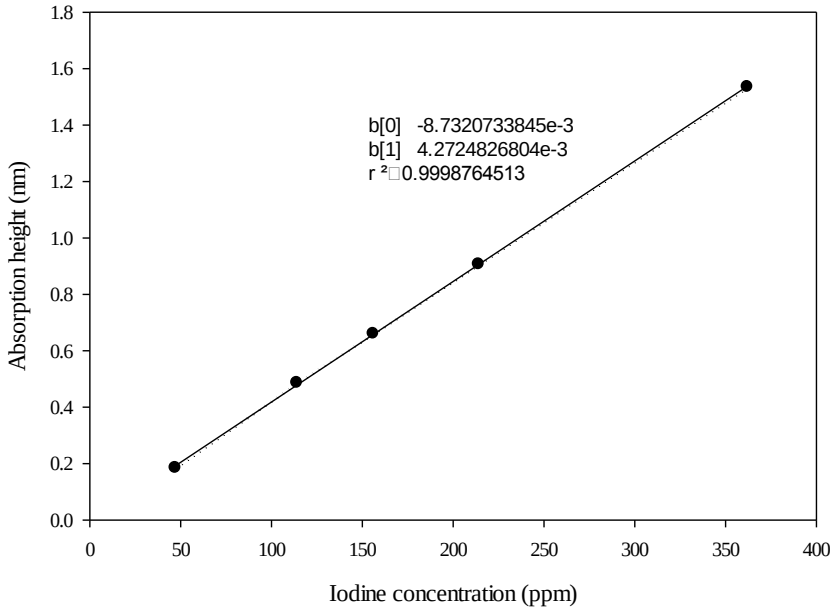

Fig B4. Iodine calibration curve for the LF-AFR; error bars are standard deviations

.

APPENDIX C

GC CALIBRATION DATA AND MEASUREMENT PROCEDURE

Since the volume of gas in a multiphase system is drastically decreased after either the reaction or the absorption, therefore the amount of sample injected to the GC sample loop becomes different at the outlet each time, compared to the initial value. The internal normalization method was used for the gas calibration in the LF-AFR because this technique corrects for the sample-size error when it is highly variable.

C.1. Internal normalization

This approach multiplies GC area by the response factor, thus correcting each area of the individual component response factor in the detector. By using this method, it is assumed that all components would respond in the detector with the same sensitivity. For this reason, first the average response factor was calculated for the mixture of sulfur dioxide-nitrogen and then it was used to calculate the mole fractions of the two known mixtures of SO_2-N_2 to check the accuracy of the method. GC operating conditions, column and detector specifications are shown in Table C1.

Table C1. GC operating conditions, column and detector specifications

detector	TCD
oven temp. (^oC)	120
split ratio	20
injector temp. (^oC)	175
detector temp. (^oC)	200
column	CP-Sil 5 CB
carrier gas	Helium
sample loop	1 ml
analysis time (min)	< 4

After obtaining the chromatograph (the average area of the peaks) for all the standard sample components (three nitrogen and sulfur dioxide mixtures, 25, 50 and 75 vol% for SO_2), the molar percent was calculated as shown in Table C2. The molar percent was then divided by the relevant area to give the concentration per unit area. Then, the reference component was chosen and assigned a response factor of 1.000. The other response factor was determined by dividing its concentration per unit area value by the concentration per unit area value of the chosen reference. For instance, for case No. 1, N_2 was chosen as the reference and the response factor of SO_2 was calculated by dividing 0.415 by 0.562 to be 0.738.

Generally, regardless of the initial concentration, these response factors should be constant as long as the operating conditions of the detector remain constant. However, some variations are observed, probably due to the experimental errors. Therefore, to minimize this systematic error, an average response factor of 0.723 was considered for SO_2.

Table C2. Internal normalization procedure to calculate response factor for the mixtures of 25, 50 and 75 vol % of SO_2

no.	comp.	molar flow (mL/min)	area (uv.min)	% area	% molar flow/area	response factor
1	N_2	0.0013392857	133.370	68.889	0.562	1.000
	SO_2	0.0004464286	60.230	31.111	0.415	0.738
	total	0.0017857143	193.600			
2	N_2	0.0008928571	92.000	41.862	0.543	1.000
	SO_2	0.0008928571	127.770	58.138	0.391	0.720
	total	0.0017857143	219.770			
3	N_2	0.0004464286	49.130	19.139	0.509	1.000
	SO_2	0.0013392857	207.570	80.861	0.361	0.710
	total	0.0017857143	256.700			

To check the accuracy of this method, two known concentrations of SO_2 (50 and 36.3 vol%) were introduced to the GC. The calculations are presented in Table C3 based on the response factor of 0.723 for SO_2. The results confirm the accuracy of the method as the difference between calculated and measured values remained below 10%.

Table C3. Using calculated response factor for the known concentrations of SO_2

no.	comp.	$(conc.)_{i,\ measured}$ (vol%)	area (uv.min)	% area	area*F	$(conc.)_{i,\ calculated}$ (vol%)
1	N_2	50	112	41.63	112	49.66
	SO_2	50	157.03	58.37	113.533	50.34
	total		269.03		225.533	
2	N_2	63.64	153	56.04	153	63.8
	SO_2	36.34	120	43.96	86.76	36.2
	total		273		239.76	

C.2. External calibration

The external calibration was used for gas phase analysis at the Corning Reactor Technology Center. The results are presented in Figure C1.

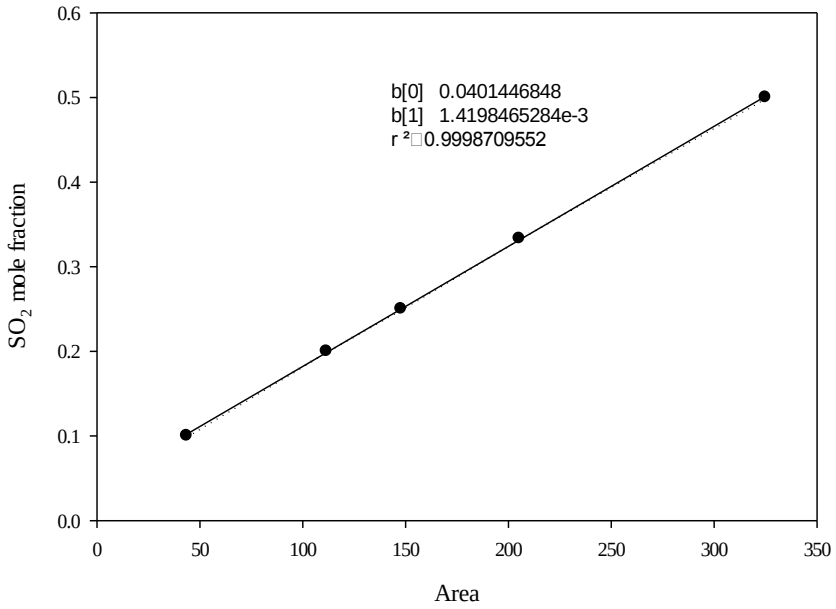

Fig C1. SO_2 external calibration curve for the G1-AFR; error bars are standard deviations

APPENDIX D

DETAILED CALCULATIONS FOR PLANT DESIGN AND ECONOMICS

Ulrich's Chemical Engineering (Process Design and Economics)[1] was used to design equipment in this Appendix.

D.1. Mass balance for the Section 1

This reaction is assumed to achieve a 100% conversion. The sulfuric acid reactant requires a concentration of 96% wt/wt and the quantity of it has an excess factor of 15.

Table D1. Mass balance for reaction between sulfuric acid and hydrogen sulfide

first reaction: $H_2SO_4 + H_2S \rightarrow SO_2 + 2H_2O + S$			
compound	molar flow rate (kmol/h)		
	inlet	change	outlet
H_2SO_4	21707.25	-1447.15	20260.1
H_2S	1447.15	-1447.15	0
SO_2	0	1447.15	1447.15
H_2O	4924.14	2894.3	7818.44
S	0	1447.15	1447.15

Table D2. Mass balance for the decanter in the Section 1

decanter stage in the Section 1				
compound	molar flow rate (kmol/h)			
	inlet	liquid phase	solid phase	gas phase
H_2SO_4	20260.1	20260.1		
SO_2	2894.3			2894.3
H_2O	7818.44	7818.44		
S	1447.15		1447.15	
total	32419.99	28078.54	1447.15	2894.3

[1] Ulrich GD. A guide to chemical engineering process design and economics. 1984.

There are two significant assumptions made for this decanting stage. The first is that this decanter can handle and separate an inlet containing three phases. Secondly, it is assumed that it can achieve 100% separation.

Table D3. Mass balance for the evaporator in the Section 1

high evaporator in the Section 1			
compound	molar flow rate (kmol/h)		
	inlet	change	final
H_2SO_4	23154.4	0	23154.4
H_2O	8474.28	-3222.58	5251.70

The evaporator will concentrate a mixture of the 93% wt/wt sulfuric acid leaving the decanter in this section and the 70% wt/wt sulfuric acid that is pre-concentrated in the Section 3. An excess amount of sulfuric acid is produced from this process, so after recycling the required 21,707.25 kmol/h to the reaction (8.1), 1,447.15 kmol/h of 96% wt/wt sulfuric acid can be sold. The water from this evaporator is recycled to the Bunsen reaction.

D.2. Mass balance for the Section 2

Table D4. Mass balance for the reactor in the Section 2

second reaction: $2H_2O + I_2 + SO_2 \rightarrow H_2SO_4 + 2HI$			
compound	molar flow rate (kmol/h)		
	inlet	change	outlet
H_2O	78583.30	-5788.6	72795.25
I_2	3216.22	-2894.3	321.92
C_7H_8	75651.05	0	75651.05
SO_2	2894.3	-2894.3	0
H_2SO_4	0	2894.3	2894.3
HI	0	5788.6	5788.6

The reaction is assumed to achieve a 100% conversion rate of the products. The excess factors compared to the limiting sulfur dioxide were determined from lab data; their values are 1.11 for iodine, 27.15 for water, and 26.13 for toluene.

Table D5. Mass balance for cryogenic air separator in the Section 2

cryogenic air separator: Air → N_2 + O_2			
compound	molar flow rate (kmol/h)		
	inlet	oxygen outlet	nitrogen outlet
O_2	1447.15	1447.15	
N_2	5444.04		5444.04

The cryogenic air separator is assumed to achieve 100% separation of the nitrogen and oxygen products. The concentration of air is assumed to be 79% nitrogen and 21% oxygen.

Table D6. Mass balance for sulfur combustion unit in the Section 2

sulfur combustion: S + O_2 → SO_2			
compound	molar flow rate (kmol/h)		
	inlet	change	outlet
S	1447.15	-1447.15	0
O_2	1447.15	-1447.15	0
SO_2	0	1447.15	1447.15

The sulfur in this unit needs to be combusted with pure oxygen so that the product is pure SO_2. An assumption is made that sulfur and oxygen can have a 1:1 molar ratio and have a 100% conversion.

D.3. Mass balance for the Section 3

Table D7. Mass balance for the first stage decanters in the Section 3

first decanting stage in the Section 3			
compound	molar flow rate (kmol/h)		
	inlet	organic outlet	aqueous outlet
I_2	321.91	321.92	
C_7H_8	75651.05	75651.05	
H_2SO_4	2894.3		2894.3
H_2O	72795.25		72768.25
HI	5788.6		5788.6

This decanter stage is for the bypass of toluene around the electrolysis unit. It is assumed to achieve 100% conversion between the two phases.

Table D8. Mass balance for the second stage decanters in the Section 3

second decanting stage in the Section 3			
compound	molar flow rate (kmol/h)		
	inlet	organic outlet	aqueous outlet
I_2	3216.22	3216.22	
C_7H_8	75651.05	75651.05	
H_2SO_4	2894.3		2894.3
H_2O	72795.25		72768.25

This decanting stage is to separate the organic and aqueous phases so they can be recycled back into the process. Again, it is assumed to achieve 100% conversion between phases.

Table D9. Mass balance for electrolysis unit in the Section 3

third reaction: $2HI \rightarrow H_2 + I_2$			
compound	molar flow rate (kmol/h)		
	inlet	change	outlet
HI	5788.6	-5788.3	0
H_2SO_4	2894.3	0	2894.3
H_2O	72795.25	0	72795.25
H_2	0	2894.3	2894.3
I_2	0	2894.3	2894.3

The electrolysis reaction is assumed to achieve a 100% conversion of hydroiodic acid. The hydrogen product is assumed to be completely separated from the other reactants.

Table D10. Mass balance for the mixer in the Section 3

mixing stage in the Section 3			
compound	molar flow rate (kmol/h)		
	organic inlet	aqueous inlet	outlet
I_2	321.92	2894.3	3216.22
C_7H_8	75651.05	0	75651.05
H_2SO_4		2894.3	2894.3
H_2O		72795.25	72768.25

This unit is for mixing the products of the electrolysis reaction with the toluene bypass.

Table D11. Mass balance for the evaporator in the Section 3

multi-stage forced-circulation evaporator in the Section 3			
compound	molar flow rate (kmol/h)		
	inlet	acid outlet	water outlet
H_2SO_4	2894.3	2894.3	0
H_2O	72795.25	655.84	72139

The acid will be concentrated from 17% to 70% wt/wt and sent to the evaporator in the Section 1 for further concentrating. The water product will be used in the Bunsen reaction.

D.4. Section 1 (Equipment sizing)

Corning® Advanced-Flow™ Reactors

1. Number of Corning reactor fluidic modules in reaction (8-1)

$$N = \frac{\dot{q} * t_{res}}{V_{G4}}$$

$$N = \frac{(343.39\ L/s) * (2.5\ s)}{250\ mL} * \left(\frac{1{,}000\ mL}{1\ L}\right)$$

$$N = 3{,}400 \text{ fluidic modules}$$

2. Capital cost of unit

$$Capital\ cost = N * C_{plate}$$

$$Capital\ cost = 3{,}434\ plates * 40{,}000\ \frac{\$}{\text{fluidic module}}$$

$$Capital\ cost = \$136{,}000{,}000$$

Decanters

3. Terminal velocity

$$u_t = \frac{\mu_f}{\rho_f D_p}\left[\left(14.4 + 1.8\sqrt{D_p^3(\rho_f - \rho_p)\rho_f g/\mu_f^2}\right)^{0.5} - 3.8\right]^2$$

$$u_t = \frac{0.005\ Pa\ s}{\left(1819\frac{kg}{m^3}\right) * (0.00025\ m)}\left[\left(14.4 + 1.8\sqrt{0.00025\ m\left(1819\ \frac{kg}{m^3} - 1758\ \frac{kg}{m^3}\right)\left(1819\ \frac{kg}{m^3}\right) * \left(9.81\frac{m}{s^2}\right)/(0.005\ Pa\ s)^2}\right)^{0.5} - 3.8\right]^2$$

$$u_t = 0.000378\ m/s$$

4. Average velocity

$$u_{ave} = \frac{L}{D}\frac{u_t}{0.5}$$

$$u_{ave} = 3 * \left(\frac{0.000378\frac{m}{s}}{0.5}\right)$$

$$u_{ave} = 0.00227\ m/s$$

The number of decanters was solved for by dividing the flow rate by whole numbers until a diameter less than the maximum diameter for decanters of 4 m was found.

5. Diameter

$$D_{horizontal\ drum} = \left(\frac{5 * \dot{q}/16}{\pi u_{ave}}\right)^{1/2}$$

$$D_{horizontal\ drum} = \left(\frac{5 * \left(\frac{0.3615}{16}\ \frac{m^3}{s}\right)}{\pi * (0.00227\ m/s)}\right)^{1/2}$$

$$D_{horizontal\ drum} = 3.98\ m$$

6. Length

$$L = \frac{L}{D}D$$

$$L = 3 * (3.98\ m)$$

$$L = 11.9\ m$$

High concentration evaporator

7. Heat transfer area

$$A = \frac{\dot{Q}}{U\Delta T}$$

$$A = \frac{103{,}400\ kW}{(5{,}000\ W \cdot m^2 \cdot K) * (20\ ℃)} * \left(\frac{1000\ W}{1\ kW}\right)$$

$$A = 1034\ m^2$$

Heat exchanger

8. Heat transfer area

$$A = \frac{\dot{Q}}{U * \Delta T_{m,corrected}}$$

$$A = \frac{-252{,}000\ kW}{(1{,}300\ W \cdot m^2 \cdot K) * (-281.4\ ℃)} * \left(\frac{1000\ W}{1\ kW}\right)$$

$$A = 690\ m^2$$

Steam Compressors

9. Number of compressors

$$q = \frac{\ln(r_{p,T})}{ln(r_{p,i})}$$

$$q = \frac{\ln(20/1.01)}{ln(2.71)}$$

$$q = 3$$

10. Fluid power

$$\dot{w}_f = \dot{m} * \frac{\Delta H}{\varepsilon_i}$$

$$\dot{w}_f = \left(20.76\frac{kg}{s}\right) * \frac{\left(3{,}409\frac{kJ}{kg} - 2{,}676\ \frac{kJ}{kg}\right)}{0.75}$$

$$\dot{w}_f = 20{,}300\ kW$$

D.4.1. Section 1 (Heat Demand)

Steam Boiler

11. Mass flow rate of steam required by heating the process

$$\dot{m}_{steam} = \frac{\dot{Q}}{\lambda}$$

$$\dot{m}_{steam} = \frac{46{,}900\ kW}{2260\ \frac{kJ}{kg}}$$

$$\dot{m}_{steam} = 20.8\ \frac{kg}{s}$$

High Concentration Evaporator

12. Heat required to concentrate sulfuric acid to 96 %wt

$$\dot{Q} = \lambda \dot{m}_{w,evap}$$

$$\dot{Q} = \left(2{,}112\ \frac{kJ}{kg}\right) * (48.98\ kg/s)$$

$$\dot{Q} = 103{,}400\ kW$$

Heat Exchanger

13. Corrected log mean temperature difference

$$\Delta T_{m,corrected} = F_T \left\{ \frac{(T_2 - t_1) - (T_1 - t_2)}{ln\left[\frac{(T_2 - t_1)}{(T_1 - t_2)}\right]} \right\}$$

$$\Delta T_{m,corrected} = 0.85 * \left\{ \frac{(153.1°C - 500°C) - (130°C - 445.7°C)}{ln\left[\frac{(153.1°C - 500°C)}{(130°C - 445.7°C)}\right]} \right\}$$

$$\Delta T_{m,corrected} = -281.4°C$$

D.5. Section 2 (Equipment sizing)

Sulfur Combustion Unit

14. Diameter

$$D = \sqrt[3]{\frac{4}{3\pi}\dot{q}\theta}$$

$$D = \sqrt[3]{\frac{4}{3\pi} * \left(1.004\ \frac{m^3}{s}\right) * (30\ s)}$$

$$D = 2.34\ m$$

15. Height

$$L = \frac{L}{D}D$$

$$L = 3 * (2.34\ m)$$

$$L = 7.02\ m$$

Compressors

16. Number of compressors

$$q = \frac{\ln(r_{p,T})}{ln(r_{p,i})}$$

$$q = \frac{\ln(10/1.01)}{ln(3.15)}$$

$$q = 2$$

17. Fluid power

$$\dot{w}_f = \dot{m}RTln\frac{P_2}{P_1}$$

$$\dot{w}_f = \left(6.431\frac{kg}{s}\right) * \left(8.314\ \frac{Pa \cdot m^3}{mol \cdot K}\right) * (298.15\ K) * \left(ln\frac{3.178\ bar}{1.01\ bar}\right)$$

$$\dot{w}_f = 18.27\ kW$$

Heat Exchanger

18. Heat transfer area

$$A = \frac{\dot{Q}}{U * \Delta T_{m,corrected}}$$

$$A = \frac{223{,}000\ kW}{(90\ W \cdot m^2 \cdot K) * (1114\ ℃)} * \left(\frac{1000\ W}{1\ kW}\right)$$

$$A = 2{,}230\ m^2$$

According to *Ulrich*, this exceeds the maximum heat transfer area per heat exchanger of 900 m^2. The number of heat exchangers required becomes 3 and the total area is divided by this.

$$A = \frac{2{,}230\ m^2}{3}$$

$$A = 743\ m^2$$

Corning® Advanced-Flow™ Reactors

19. Number of Corning reactor fluidic modules in reaction (8.2)

$$N = \frac{\dot{q} * t_{res}}{V_{G4}}$$

$$N = \frac{(9{,}460\ m^3/hr) * (6.66\ s)}{250\ mL} * \left(\frac{1\ hr}{3600\ s}\right) * \left(\frac{1{,}000{,}000\ mL}{1\ m^3}\right)$$

$$N = 70{,}000$$

20. Capital cost of unit

$$Capital\ cost = N * C_{plate}$$

$$Capital\ cost = 70{,}000\ plates * 40{,}000\ \frac{\$}{\text{fluidic modules}}$$

$$Capital\ cost = \$2{,}800{,}000{,}000$$

Heat Exchanger

21. Corrected log mean temperature difference

$$\Delta T_{m,corrected} = F_T \left\{ \frac{(T_2 - t_1) - (T_1 - t_2)}{ln\left[\frac{(T_2 - t_1)}{(T_1 - t_2)}\right]} \right\}$$

$$\Delta T_{m,corrected} = 0.84 * \left\{ \frac{(500.1°C - 211.9°C) - (4{,}124°C - 467.6°C)}{ln\left[\frac{(500.1°C - 211.9°C)}{(4{,}124°C - 467.6°C)}\right]} \right\}$$

$$\Delta T_{m,corrected} = 1114°C$$

D.6. Section 3 (Equipment sizing)

Electrolysis Unit

22. Number of plates

$$N = \frac{\dot{q}_{total}}{\dot{q}_{plate}} = \frac{1{,}760\ \frac{m^3}{hr}}{0.6\ \frac{m^3}{hr}} = 2{,}934 \text{ plates}$$

23. Capital cost of unit

$$Capital\ cost = N * C_{plate}$$

$$Capital\ cost = (2{,}934\ plates) * \left(15{,}000\,\frac{\$}{\text{plate}}\right)$$

$$Capital\ cost = \$44{,}010{,}000$$

24. Current requirement (for 100% current efficiency)

$$I = (\dot{q}_{H2})(F)(z)$$

$$I = \left(803.97\,\frac{mol\ H_2}{s}\right) * \left(96{,}485.34\,\frac{C}{mol\ e^-}\right) * \left(2\,\frac{mol\ e^-}{mol\ H_2}\right)$$

$$I = 155{,}143\ kA$$

25. Current requirement (for 86% current efficiency)

$$I = \frac{155{,}143\ kA}{0.86} = 180{,}399\ kA$$

26. Power Demand

$$P = IV$$

$$I = (1.51V) * (180{,}399kA) = 272\ MW$$

Decanters

27. Terminal velocity

$$u_t = \frac{\mu_f}{\rho_f D_p}\left[\left(14.4 + 1.8\sqrt{D_p^3(\rho_f - \rho_p)\rho_f g/\mu_f^2}\right)^{0.5} - 3.8\right]^2$$

$$u_t = \frac{0.001005\ Pa\ s}{\left(998\frac{kg}{m^3}\right) * (0.00015\ m)}\left[\left(14.4 + 1.8\sqrt{0.00015\ m\left(998\ \frac{kg}{m^3} - 886\ \frac{kg}{m^3}\right)\left(998\ \frac{kg}{m^3}\right) * \left(9.81\frac{m}{s^2}\right)/(0.001005\ Pa\ s)^2}\right)^{0.5} - 3.8\right]^2$$

$$u_t = 0.001415\ m/s$$

28. Average velocity

$$u_{ave} = \frac{L}{D}\frac{u_t}{0.5}$$

$$u_{ave} = 3 * \left(\frac{0.001415\frac{m}{s}}{0.5}\right)$$

$$u_{ave} = 0.008493\ m/s$$

The number of decanters was solved for by dividing the flow rate by whole numbers until a diameter less than the maximum diameter for decanters of 4 m was found.

29. Diameter

$$D_{horizontal\ drum} = \left(\frac{5 * \dot{q}/5}{\pi u_{ave}}\right)^{1/2}$$

$$D_{horizontal\ drum} = \left(\frac{5 * \left(\frac{2.633}{31}\ \frac{m^3}{s}\right)}{\pi * (0.00849\ m/s)}\right)^{1/2}$$

$$D_{horizontal\ drum} = 4\ m$$

30. Length

$$L = \frac{L}{D}D$$

$$L = 3 * (4\ m)$$

$$L = 12\ m$$

High concentration evaporator

31. Heat transfer area

$$A = \frac{\dot{Q}}{U\Delta T}$$

$$A = \frac{797{,}200\ kW}{(5{,}000\ W \cdot m^2 \cdot K) * (20\ ℃)} * \left(\frac{1000\ W}{1\ kW}\right)$$

$$A = 797\ m^2$$

D.7. Capital expenses

The fixed capital of the design was determined from the summation of all equipment and start-up material costs. A summary of these costs can be seen below in Table D12. It is important to note that included in the total fixed capital were estimated costs of contingency fees and auxiliary facilities. Auxiliary facilities include the additional costs not included in the equipment design costs, such as buildings to house equipment, piping, and additional pumps. The auxiliary facilities were cost based on 30% of the total module capital, equaling approximately $1.13 billion. Since this cost is purely based off of a percentage, it may not accurately represent the actual cost of auxiliary facilities. With additional research, the auxiliary costs could likely be reduced. The start-up materials are also included in the capital cost summary. Although once the process is in operation most feedstock materials will be supplied through recycle, some feedstocks are required at plant start-up. The start-up materials to be purchased are iodine, toluene, and sulfuric acid. The cost of start-up materials is $18.3 million.

Table D12. Capital expense summary

type	notes	cost
material expenses		
iodine	45 min residence time @ $6091/kmol	$14,692,961
toluene	30 min residence time @ $95/kmol	$3,610,946
sulfuric acid	25 min residence time @ $7.2/kmol	$60,439
	materials total	$18,364,347
equipment		
multi stage evaporator	forced circulation rising/falling film up to 70% (wt/wt)	$16,701,353
high concentrator	forced circulation rising/falling film up to 96% (wt/wt)	$2,877,428
decanter 1	sulfur: 3-phase	$14,745,600
decanter 2	toluene: 2-phase	$57,139,200
mixer	motionless mixer, nickel alloy	$900,695
cryogenic separator	cast steel; process 1,100 tonnes air/day	$78,114,080
steam boiler	heating steam to 500°C 20 bar, 250100 kW	$106,654,404
heat exchanger 1	SO_2 combustion cooling; C-276 alloy; 2,230 m^2	$669,471
heat exchanger 2	H_2SO_4 heating; C-276 alloy; 689 m^2	$367,609
compressor 1	steam compression 1-20 bar	$18,868,133
compressor 2	oxygen compression 1-10 bar	$156,522
reactor 1	Corning G4; 3400 fluidic modules	$136,000,000
reactor 2	Corning G4; 70,000 fluidic modules	$2,800,000,000
electrolysis	titanium electrodes; 10342 plates; A=2.5 m^2	$43,950,000
sulfur combustion	brick-lined cast steel; D: 2.3 m, H: 7.0 m	$99,000
	equipment total	$3,201,021,198
	total module capital	$3,777,205,013
	auxiliary facilities	$1,133,161,504
	total grassroots capital	**$4,928,730,864**

D.8. Operating expenses

The operating expenses of the plant were broken down into three categories, which were direct, indirect, and general expenses. The direct expenses included feedstock costs and utility expenses for the electricity and heat requirements. Indirect expenses included overhead costs, as well as local taxes and insurance. General expenses included the administrative expenses and research and development. The total annual operating expenses were found to be $1.5 billion. The summary of all operating expenses is shown below in Table D13.

Table D13. Operating expense summary

manufacturing expenses	annual cost ($/yr)
direct	
raw materials - water (@ 10ºC, 101.3kPa)	$396,434.45
raw materials – iodine	$171,613,786
raw materials – toluene	$63,263,776
operating labour	$1,612,356
supervising and clerical labour (15% of operating labour)	$241,853
utilities	
electricity (for electrolysis, 2,386,244,508 kWh @ 0.06393 $/kWh)	$152,552,611
electricity (steam/O_2 compression 177,713,746 kWh @ 0.06393 $/kWh)	$11,361,240
power (for CH_4 combustion, 2,293,835,812 kWh @ $3.82/GJ)	$36,575,044
power (for cryogenic separator, scale up)	8,470,309.84
maintenance and repairs (6% of fixed capital)	$295,723,852
operating and supplies (15% of maintenance and repairs)	$44,358,578
laboratory charges (15% of operating labour)	$241,853
patents and royalties (3% of total expense)	$42,345,994
A_{DME}	**$828,757,686**
indirect	
overhead, packing and storage (60% of op. labour, supervision, maintenance)	$178,546,836
local taxes (2% of fixed capital)	$98,574,617
insurance (1% of fixed capital)	$49,287,309
A_{IME}	**$326,408,762**
general expenses	
administrative costs (25% of overhead)	$44,636,709
distribution and selling (10% of total expense)	$141,153,313
research and development (5% of total expense)	$70,576,656
total general expenses A_{GE}	**$256,366,678**
total expenses A_{TE}	**$1,411,533,127**

D.9. Revenue

This process would generate revenue through the sale of produced hydrogen, nitrogen, and sulfuric acid. As seen in Table D14, the total revenue of the plant exceeds two billion dollars, and the largest portion of revenue is from the sale of nitrogen. For determining the revenue of this process, it was assumed that all products would be sold at their current market price.

Table D14. Revenue summary

product	production rate (tonnes/year)	sale price ($/tonnes)	source	revenue ($ million/year)
H_2	51,000	$ 7,000	(U of Birmingham 2013)	$ 357.8
H_2SO_4	1,243,343	$ 73	(ICIS Chemical Business 2014)	$ 90.8
N_2	1,335,953	$ 1,280	(OMAFRA 2014)	$ 1,710.0
			total revenue	$ 2,158.6

D.10. Economic analysis of plant life cycle

An economic analysis was done over the 30-year life of the plant. The plant construction will occur in the first three years. A third of the fixed capital will be invested in each of these years, with the working capital being invested in the third year. Table D15 shows the annual sales in the first three years of operation.

Table D15. Annual sales in first three years of operation

year	percentage of revenue	revenue ($ million/year)
4	50%	$1,079
5	75%	$1,619
6	100%	$2,159

The revenue was assumed to remain at $2,159 million per year continuing after year six. The payback period was found to be 10.4 years, from the beginning of plant operation to crossing the working capital line. The break-even point was found to be 14.4 years, from the start of plant construction to crossing the $0 line.

PERMISSION TO REPRODUCE

Permission to use Figure 3.1 and Figure 3.2:

License Number	3607940412011
License date	Apr 14, 2015
Licensed content publisher	Elsevier
Licensed content publication	Fuel Processing Technology
Licensed content title	A low-temperature hydrogen production process based on H2S splitting cycle for sustainable oil sands bitumen upgrading
Licensed content author	Hui Wang,Annaïg Le Person,Xu Zhao,Ji Li,Patricia Nuncio,Liuqing Yang,Armin Moniri,Karl T. Chuang
Licensed content date	April 2013
Licensed content volume number	108
Licensed content issue number	n/a
Number of pages	8
Type of Use	reuse in a thesis/dissertation
Portion	figures/tables/illustrations
Number of figures/tables/illustrations	2
Format	both print and electronic
Are you the author of this Elsevier article?	Yes
Will you be translating?	No
Original figure numbers	figures 3, 4
Title of your thesis/dissertation	THE EXPERIMENTAL AND THEORETICAL INVESTIGATION OF THE HYDROGEN SULFIDE SPLITTING CYCLE FOR HYDROGEN PRODUCTION
Expected completion date	Apr 2015
Estimated size (number of pages)	200
Elsevier VAT number	GB 494 6272 12
Permissions price	0.00 CAD
VAT/Local Sales Tax	0.00 CAD / 0.00 GBP
Total	0.00 CAD